Technische Universität Ilmenau
Fakultät für Mathematik und Naturwissenschaften
Institut für Physik
Fachgebiet Experimentalphysik I

COMPOSITE CONJUGATED POLYMER/FULLERENE FILMS: STRUCTURE–PROPERTY RELATION

Dissertation zur Erlangung des akademischen Grades
Doctor rerum naturalium

Eingereicht von:
Dipl.-Phys. Uladzimir Zhokhavets

Betreuer:
Prof. Dr. habil. Gerhard Gobsch

Gutachter:
Prof. Dr. habil. Gerhard Gobsch
Prof. Dr. habil. Bernd Stühn
Dr. habil. Christoph Brabec

Eingereicht am: 13.07.2005
Verteidigt am: 18.11.2005

urn:nbn:de:gbv:ilm1-2005000215

Abstract

Conjugated polymer/fullerene based plastic solar cells represent an exciting alternative to inorganic ones because of their low production costs, flexibility and low weight. At present, commercialisation of plastic solar cells is limited due to their relatively low efficiency in comparison to silicon ones. In order to understand the operation of plastic solar cells and to increase their efficiency, more information about structure of absorber layer is needed. Especially the connection between structure and properties of the absorber layer is of great importance.

The aim of this work was to study the correlation between structural, optical and transport properties of conjugated polymer/fullerene films, which are used as absorber layer in plastic solar cells. We start by investigation of pristine polythiophene films. From X-ray diffraction and spectroscopic ellipsometry studies it follows, that the polythiophene films consist of a highly ordered interface layer. After this interface layer the order of the polymer drops off with increasing distance from the substrate. The decisive for growth of the film parameters were established. A correlation between the anisotropic charge carrier mobilities and the film structure was shown. After this, the polythiophene/fullerene films were investigated. We found, that annealing of such films supports the formation of polythiophene crystallites due to enhanced diffusion of fullerene at elevated temperatures. The crystallisation of polythiophene leads to an increased optical absorption in visible region due to stronger interchain interaction between polythiophene molecules. The observed increase of the efficiency of the polythiophene/fullerene solar cells after annealing was explained by improved optical absorption together with improved hole mobility.

Zusammenfassung

Plastiksolarzellen stellen aufgrund ihrer niedrigen Produktionskosten, Flexibilität und niedrigem Gewicht eine vielversprechende Alternative zu herkömmlichen, auf anorganischen Materialien basierenden Solarzellen, z. B. Silizium, dar. Momentan wird die Vermarktung durch die relativ geringe Effizienz im Vergleich zu den sehr häufig eingesetzten Siliziumsolarzellen behindert. Um das Funktionsprinzip der Plastiksolarzellen zu verstehen und die Effizienz zu steigern, müssen Informationen über die Struktur der Absorberschicht gewonnen werden. Speziell der Zusammenhang zwischen dem strukturellen Aufbau der Absorberschicht und deren optischen und elektrischen Eigenschaften ist von herausragender Bedeutung.

Das Ziel dieser Arbeit ist es, den Zusammenhang zwischen den strukturellen und optischen Eigenschaften sowie dem Ladungsträgertransport von konjugierten Polymer/Fulleren-Kompositschichten zu untersuchen, die als Absorberschichten in Plastiksolarzellen verwendet werden. Wir haben damit begonnen, mittels Röntgen-Diffraktometrie und Spektralellipsometrie reine Polythiophen-Schichten zu untersuchen. Die Ergebnisse beider Methoden zeigen, dass sich auf der Oberfläche des Substrates zunächst eine hoch geordnete Polythiophen-Grenzschicht ausbildet. Danach findet man für das Polythiophen über der geordneten Grenzschicht eine stetige Zunahme der Unordnung mit steigendem Abstand zum Substrat. Des Weiteren wurden die für das Schichtwachstum wichtigen Parameter ermittelt und der Zusammenhang zwischen der anisotropen Ladungsträgerbeweglichkeit und der Schichtstruktur demonstriert. In einem nächsten Schritt wurden Polythiophen/Fulleren-Kompositschichten untersucht. Die Ergebnisse zeigen, dass das Tempern der Kompositschichten zur Ausbildung der Polythiophenkristalliten führt. Ursache hierfür ist die verstärkte thermische Diffusion von Fullerenmolekülen während des Temperprozesses. Die Ausbildung von Polythiophenkristalliten hat zur Folge, dass die Absorption im sichtbaren Spektralbereich verstärkt wird. Die festgestellte Erhöhung des Wirkungsgrades

von getemperten Polythiophen/Fulleren-Solarzellen nach dem Tempern wird durch die verbesserte Absorption und die gestiegene Ladungsträgerbeweglichkeit erklärt.

Contents

Chapter 1

Introduction

The limitation of the fossil fuels leads to the growing interest in the renewable energy sources like wind, water or solar energy. According to the forecasts of many leading companies and institutes, the renewable energy sources will play a major role already in the near future. That is why significant efforts are concentrated at present on the development of devices which utilise these energy sources. In particular, photovoltaic solar cells which convert solar energy directly into electrical power are of interest. The great advantage of the photovoltaic solar cells is their excellent scalability, which allows the decentralisation of the energy generation and consumption.

The photovoltaic market has a growth rate of 25%/year over the last 15 years [1]. At present, the photovoltaic market is dominated by silicon solar cells. Other inorganic solar cells (see Table 1.1) can not compete with Si solar cells at the moment because of its high costs (GaAs cells, tandem cells) or due to environmental damage (CdTe, CIGS cells).

The silicon solar cells have an excellent power conversion efficiency and a lifetime up to 25 years. However, the production costs for silicon solar cells of approximately 3 Euro/Wp are still too high due to the need for costly semiconductor processing technologies. This significantly limits the overall application of silicon solar cells.

Conjugated polymer/fullerene based plastic solar cells (further "plastic solar cells") (Fig. 1.1) represent an exciting alternative to the inorganic ones. The active layer of such cells is a so-called "bulk heterojunction", i. e. a conjugated polymer/fullerene mixture. The required thickness of the active layer is with 100-300 nm very low (compared for example with $\sim$2 μm for amorphous and $\sim$300 μm for crystalline Si-cells), resulting in low material consumption. These cells could

Table 1.1: Power conversion efficiencies of inorganic and organic laboratory solar cells under AM1.5 Global 1000 W/m^2 illumination. Status: 07.09.2004.

Material system	Power conversion efficiency (%)
Inorganic solar cells [2]	
Si (crystalline)	24.7
Si (nanocrystalline)	10.1
GaAs (crystalline)	25.1
CdTe (polycrystalline)	16.5
CIGS (polycrystalline)	18.4
Plastic solar cells	
MDMO-PPV/PCBM	2.5* [3]
P3HT/PCBM	3.5* [4]

*under 800 W/m^2 illumination

be fabricated using simple and cheap production techniques like blade casting or continuous printing process. This would lead to significant cost reduction as compared to the silicon technology. Production costs as low as 0.3 Euro/Wp seem to be realistic [1]. Another benefits of the plastic solar cells are mechanical flexibility and low weight, which is essential for many special applications.

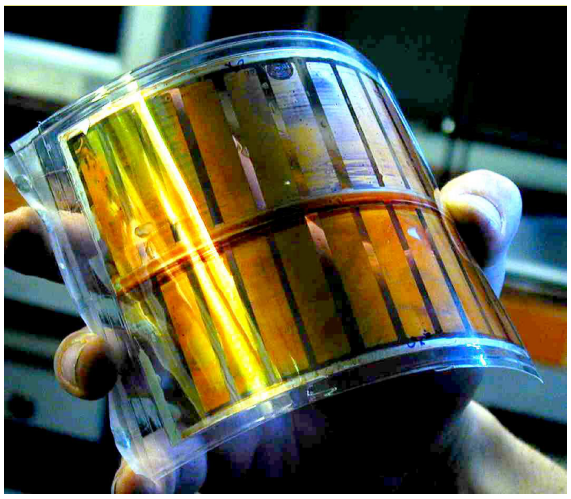

Figure 1.1: Plastic solar cell [5].

Although the efficiency of the plastic solar cells was significantly increased in the last years [3, 6, 4] (see also Table 1.1), it is still a main limiting factor for their commercialisation. Another problem which must be solved is not sufficient stability of the plastic solar cells [7].

There are two processes which mainly determine the efficiency of the plastic

solar cells: a) creation of electron/hole pairs due to absorption of light, and b) transport of the generated charges to the electrodes. The first process is determined by the absorption coefficient of the used conjugated polymer/fullerene blend and the charge transfer process between the two components, whereas the transport of the charge carriers to the electrodes is mainly determined by electron and hole mobilities. Other factors limiting the efficiency of the plastic solar cells like low open circuit voltage, high contact resistance, optical losses (see also Appendix C for more details) were not considered in this work. Let us focus on the charge transport and optical properties of the active layer.

Optical and charge transport properties of composite conjugated polymer/fullerene films depend not only on optical/transport properties of constituents, but also on the morphology of the active layer. TEM, SEM and AFM studies [8, 9, 10, 3] on thin conjugated polymer/fullerene films show a strong phase separation between the conjugated polymer and the fullerene. The degree of the phase separation and therefore the macroscopic optical and transport properties of the films depend strongly on preparation conditions like fullerene concentration, solvent type or thermal treatment (annealing). In the case of poly[2-methoxy-5-(3,7-dimethyloctyloxy)-1,4-phenylenevinylene] / [6,6]-phenyl-C61-butyric acid methyl ester (MDMO-PPV/PCBM) solar cells, an increase of short circuit current from 2.33 mA/cm^2 to 5.25 mA/cm^2 and solar cell efficiency from 0.9% to 2.5% by changing the solvent from toluene to chlorebenzene was observed [3]. This improvement was explained by increased charge carrier mobilities in the chlorobenzene-cast active layer. Further on, the efficiency of poly(3-hexylthiophene) (P3HT)/PCBM solar cells was improved from 0.4% to 2.5% upon annealing of the solar cells [4]. These two examples demonstrate the enormous influence of the film structure on the solar cell performance.

Although the morphology of the active layer was intensively studied since several years, the most efforts were focused on the relation between preparation parameters (solvent type, conjugated polymer/fullerene blend ratio and so on) and the solar cell performance. This approach could help to reach higher solar cell efficiencies; however, the fundamental knowledge about the film structure and the relation between the film structure and film properties can not be gained. To understand the reasons for better (or worse) solar cell performance, the influence of the layer structure on the "key parameters" (charge carrier mobilities/lifetimes, optical absorption) must be clarified. For this reason, the aim of this work was to study the relation between structural, optical and transport properties of

conjugated polymer/fullerene films.

Before investigating composite conjugated polymer/fullerene films, the knowledge about pristine conjugated polymer films is required. Since the conjugated polymer and the fullerene phases in conjugated polymer/fullerene layer are separated, one could expect that the findings for pristine conjugated polymer films can be adopted for the conjugated polymer/fullerene composites after careful revision.

The structure–property relation was studied on standard materials, poly(3-octylthiophene) (P3OT) and poly(3-hexylthiophene) (P3HT), and their composites with PCBM. The polythiophene/fullerene composites are currently widely used in plastic solar cells.

The structure of this work is as follows:

In Chapter 2, the chemical and physical properties of conjugated polymers and their composites with fullerenes are briefly discussed. The configuration of a plastic solar cell and the principles of its operation are described. In Chapter 3, the goal of this work is formulated. Chapter 4 contains the description of the investigated materials. After this, the experimental methods used in this work for optical (spectroscopic ellipsometry (SE), photoluminescence spectroscopy (PL)) and structural (X-ray diffraction (XRD)) characterisation are described (Chapter 5).

The results are presented in Chapters 6 and 7. The XRD and SE measurements on pristine polythiophene films are reported in Chapter 6. On the basis of this data, the model describing structure and growth of the polythiophene films is proposed. The influence of the film structure on the anisotropic charge carrier mobility in polythiophene films is discussed.

In Chapter 7, structural and optical properties of polythiophene/fullerene films were studied and compared with this of pristine polythiophene films. After this, the effect of annealing on structural, optical and transport properties of polythiophene/fullerene composite films was studied.

The most important results of this work are summarised in Chapter 8.

Chapter 2

Physics of plastic solar cells

2.1 Conjugated polymers

Conjugated polymers are semiconducting organic materials with π-conjugated electron system, which exhibit an unique combination of optical, electrical and mechanical properties [11]. The primary tasks of the conjugated polymer in plastic solar cell are to absorb the light and to transport the positive charges to the ITO electrode.

2.1.1 Chemical structure

The chemical structures of some conjugated polymers are shown in Fig. 2.1. Among the conjugated polymers, the *trans*-polyacetylene has the simplest structure and therefore it is considered here as a model system. To hold together the polymer backbone, only two of the four valence electrons of carbon atom are needed. These two electrons of carbon atom form σ-orbitals between the carbon atoms in the backbone. The third electron builds a σ-bond with hydrogen. Thus, one electron per carbon atom is remaining. This remaining fourth electron builds a p_z-orbital, which is perpendicular to the backbone plane. All these p_z orbitals overlap and form a π-band. Because the π-band is half-filled with π-electrons, each polyacetylene chain should theoretically have metallic conductivity. It was however shown, that polyacetylene is a semiconductor with band gap of 1.5 eV. This contradiction can be explained by Peierls instability, which leads to the alternation of the bond length between neighbour carbon atoms and therefore to the splitting of the π-band into the valence and conduction bands [12].

Although the chemical structures of the other conjugated polymers shown

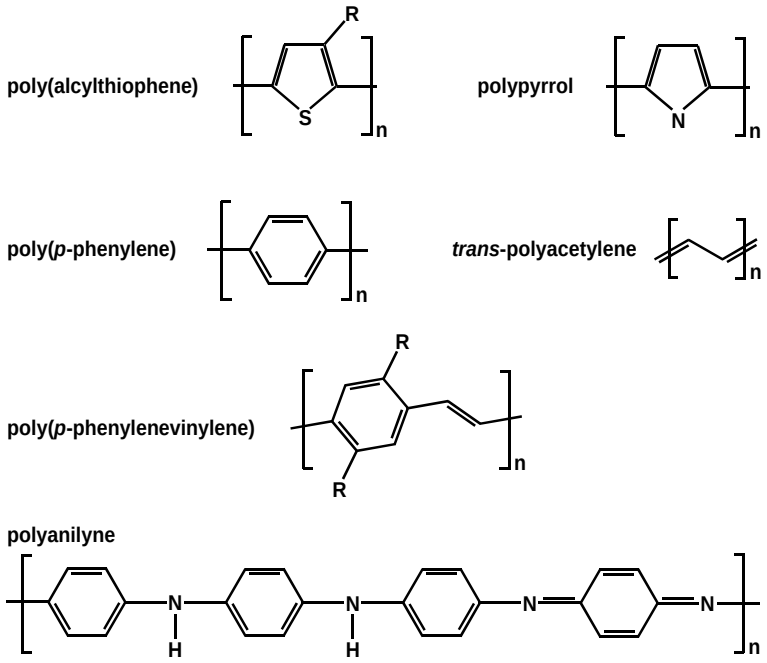

Figure 2.1: Chemical structure of widely used conjugated polymers .

in Fig. 2.1 are much more complicated than that of *trans*-polyacetylene, the mechanism of electrical conductivity is qualitatively the same (i. e. the overlap of the wave functions of the π-electrons).

2.1.2 Electronic states and electrical conductivity

By placing a positive (or negative) charge on the conjugated polymer chain, a quasi-particle called positive (negative) polaron is created. This is because the positive (negative) charge induces a lattice deformation, as shown in Fig. 2.2 for poly(*p*-phenylenevinylene). Due to the lattice deformation, new states within the gap arise (Fig. 2.2). These new states can be detected, for example, by photoinduced absorption spectroscopy.

The polarons can be created in different ways. First, they can be introduced by electrochemical doping, for example, with iodine atoms [14]. Secondly, the excitons (see section 2.1.3) generated by absorption of light can be separated by strong electric fields, resulting in the formation of free positive/negative polaron pairs. Third, positive polarons can be built through the photoinduced electron transfer, which occurs in conjugated polymer/fullerene composites as described in section 2.2.

Since the polarons can move along the polymer backbone, they are responsible for charge transport in conjugated polymers. The transport along the polymer

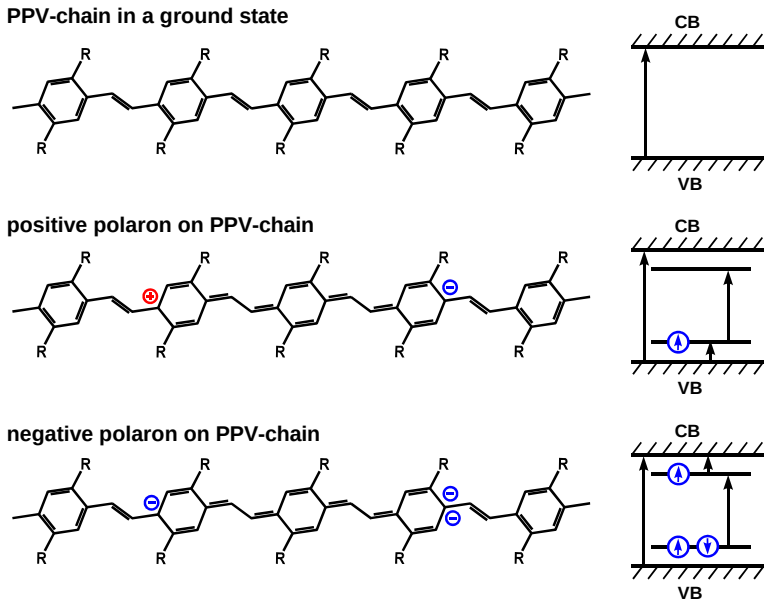

Figure 2.2: Structure of positive and negative polarons on PPV-chain and corresponding allowed optical transitions [13].

chain is supposed to be quite effective. For instance, relatively high mobilities of $\sim$0.1 cm^2/(V s) were obtained for polythiophene transistors [15, 16]. However, defects like chain kinks or finite chain lengths form potential wells ("traps") and potential barriers for the polarons (Fig. 2.3a,b). The trapped polarons and those which have reached the chain boundary can escape by field-assisted tunneling (see Fig. 2.3c).

Thus, the charge transport on the macroscopic distance is always assisted by tunneling ("hopping" transport). The traps drastically limit the mobility of charge carriers in conjugated polymers. That is why the charge carrier mobilities of conjugated polymers are 3-10 orders of magnitude lower than these of inorganic semiconductors (see Table 2.1).

It should be pointed out, that charge carrier mobilities depend strongly not only on the material, but also on the film morphology. For instance, the mobility of highly ordered or aligned materials is several orders of magnitude larger than that of amorphous or not oriented materials (see data for aligned polythiophene films or for pentacene, Table 2.1). The highest mobilities were reported for films of well ordered small molecules and oligomers with large crystalline areas [20, 21, 22]. The intrinsic mobilities as high as 75 cm^2/(V s) were estimated for ideal pentacene crystal [25]. The reason for this is that the number of traps caused by structural defects is much lower in highly ordered materials. Thus,

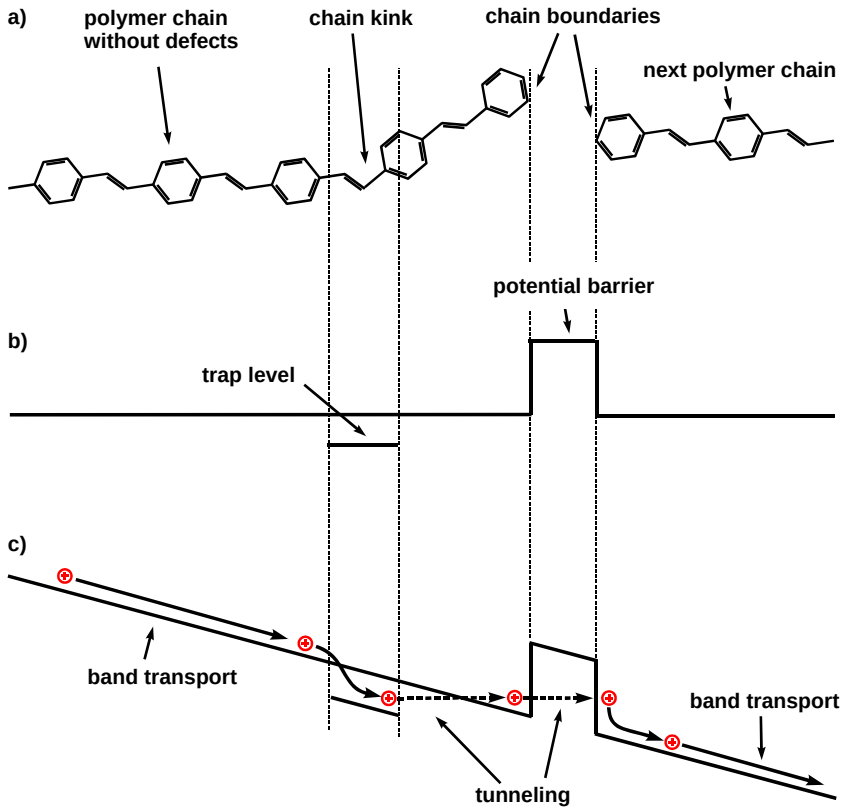

Figure 2.3: Polymer chain with characteristic defects (a); schematic energy diagram for positive polarons without electric field (b) and charge transport under applied electric field (c).

the charge carrier mobility can be significantly enhanced by choosing preparation methods, which give highly ordered films with a low number of structural defects.

2.1.3 Optical excitations in conjugated polymers

The lowest energy optical transition in conjugated polymers E_0 is attributed to the formation of a singlet exciton. The singlet exciton is an electron-hole pair with spin 0, bound by the Coulomb attraction. The transitions at higher photon energies correspond to the formation of singlet exciton with one or several phonons, or to the band-band transition. The difference between electronic gap E_G and the energy of excitonic transition E_0 is the exciton binding energy E_B. The lowest energy transition E_0 determines the onset of an optical absorption ("optical gap", E_G^{OPT}).

The scheme of optical excitations in polythiophenes is shown in Fig. 2.4. The polythiophenes have an optical gap of 1.96 eV, followed by absorption peaks at $E_0 = 2.05$, $E_1 = 2.20$ and $E_2 = 2.35$ eV. These peaks are attributed to the singlet

Table 2.1: Charge carrier mobilities in thin films of some organic and inorganic materials.

Material	Electron (e) or hole (h) mobilities ($cm^2/(V\ s)$)	Reference
Organic		
Polythiophene (spin-coated films)	$10^{-4} - 10^{-2}$ (h)	[17]
Polythiophene (aligned by drawing method)		
parallel to the alignment direction	$7.4 * 10^{-4}$ (h)	[18]
perpendicular to the alignment direction	$0.9 * 10^{-4}$ (h)	[18]
Polythiophene (printed)	0.1 (h)	[16]
MDMO-PPV/PCBM (spin-coated films)	$2 * 10^{-7} - 5 * 10^{-6}$ (h),	[19]
	$2 * 10^{-5} - 4 * 10^{-4}$ (e)	[19]
Oligothiophene	$0.1 - 0.5$ (h)	[20]
Pentacene (polycrystalline)	$0.3 - 1.0$ (h)	[21]
Pentacene (single crystal)	2.0 (h)	[22]
Inorganic		
c-Si	1400 (e), 480 (h)	[23]
c-GaAs	8000 (e), 400 (h)	[24]

excitonic transition at 2.05 eV with vibronic sidebands at 2.20 and 2.35 eV. The shape of the absorption in high photon energy region above 2.5 eV is determined by band-to-band transition at $E_G = 2.67$ eV. This transition is not clearly seen in absorption spectrum because of the lower oscillator strength in comparison to the excitonic transitions. However, it can be detected with another experimental methods like two-photon absorption [26, 27].

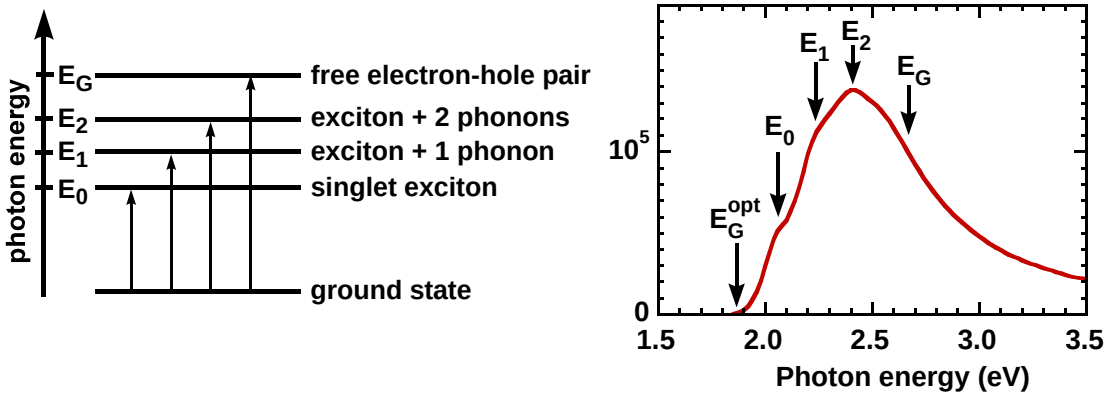

Figure 2.4: Scheme of optical excitations in polythiophenes (left) and absorption coefficient of P3OT (right).

The most theoretical and experimental studies [28, 29, 26, 30, 31] support

large (∼0.5 eV) exciton binding energies. For comparison, the exciton binding energy for most inorganic semiconductors does not exceed several tens of meV [32]. Because the thermal energy kT at room temperature is only 26 meV, there is no noticeable thermal exciton dissociation in organic semiconductors. In principle, the generated excitons can dissociate in strong enough electric field. Assuming the exciton size of $L \sim 10$ nm, which is typical value for the exciton size in different conjugated polymers [33], the ionisation field of $E = 5 \cdot 10^5$ V/cm is obtained. Such strong electric fields can be achieved for example by applying the voltage of 5 Volts between electrodes of a 100 nm thick solar cell. For this reason, the first plastic solar cells consisting of a single conjugated polymer active layer between metallic electrodes showed a very weak photovoltaic effect ($\eta < 0.1\%$). Thus, pure conjugated polymers are not promising for application in solar cells. Significantly higher power conversion efficiencies were achieved with so called "bulk-heterojunction" solar cells.

2.2 Conjugated polymer/fullerene blends

2.2.1 Ultra-fast photoinduced electron transfer

Due to the high exciton binding energy, a very strong electric field is needed in order to create free positive and negative polarons on the conjugated polymer chain. This difficulty was overcome in bulk heterojunction solar cells by mixing conjugated polymer with fullerenes [34]. In this mixture, charge separation occurs in less than 45 fs due to ultra-fast electron transfer from conjugated polymers to fullerenes [35]. This phenomenon is called photoinduced charge transfer [36]. The photoinduced charge transfer can be divided into following 4 steps [36]:

- excitation of the conjugated polymer and formation of an exciton;
- delocalisation of the excitation on conjugated polymer/fullerene complex;
- electron transfer from conjugated polymer to the fullerene and formation of an ion paar;
- charge carrier delocalisation on the conjugated polymer (positive polaron) and fullerene (electron).

To determine the efficiency of the photoinduced charge transfer, the measurement of photoluminescence quenching can be used [36]. In the photoluminescence

quenching experiment, the samples of pure conjugated polymer and conjugated polymer/fullerene blend are excited by a laser, and photoluminescence spectra of both samples $PL_{polymer}(\hbar\omega)$ and $PL_{blend}(\hbar\omega)$ are recorded. The intensity of the pump beam I_{pump} is the same for both samples. Let us define the photoluminescence quenching $Q(\hbar\omega)$ as the ratio of photoluminescence intensities of pristine conjugated polymer film and conjugated polymer/fullerene film, i. e.

$$Q(\hbar\omega) = \frac{PL_{polymer}(\hbar\omega)}{PL_{blend}(\hbar\omega)}. \tag{2.1}$$

It is known, that the excitons on conjugated polymers recombine radiative. On the other hand, the separated positive polaron on the polymer chain and electron on the fullerene recombine without emission of light (photoluminescence intensity = 0). In the conjugated polymer/fullerene composite, some excitons recombine before the dissociation, and others dissociate due to photoinduced electron transfer and recombine then non-radiative (see Fig. 2.5).

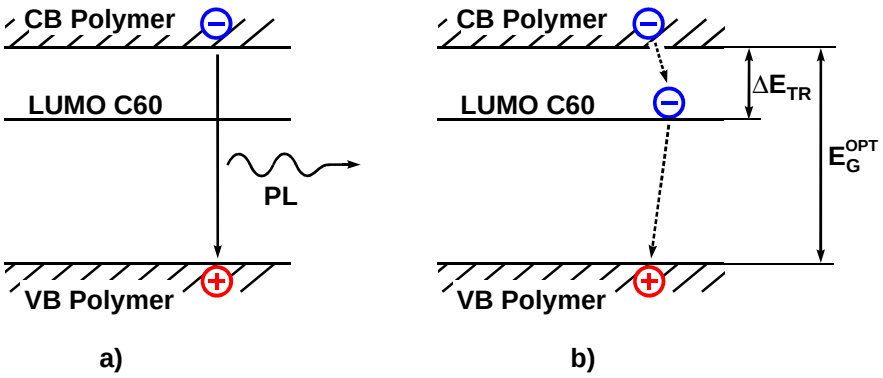

Figure 2.5: Radiative (a) and non-radiative (b) recombination of photogenerated excitons in conjugated polymer/fullerene blend. The probabilities of the non-radiative and radiative recombination are η_{PET} and $1 - \eta_{PET}$, respectively.

Let η_{PET} be the part of excitons which dissociate before recombination; then $1 - \eta_{PET}$ is the part of excitons which recombine radiatively. Thus the η_{PET} characterise the efficiency of photoinduced electron transfer. Let also $G_{polymer}$ and G_{blend} be the exciton generation rates for the conjugated polymer and the conjugated polymer/fullerene films, respectively, and $I_{exc}(\hbar\omega)$ be a spectral density of a single exciton. Then the photoluminescence of this two samples can be written as:

$$PL_{polymer}(\hbar\omega) = G_{polymer} I_{exc}(\hbar\omega), \tag{2.2}$$

$$PL_{blend}(\hbar\omega) = G_{blend}(1 - \eta_{PET}) I_{exc}(\hbar\omega). \tag{2.3}$$

For the photoluminescence quenching $Q(\hbar\omega)$ one obtains:

$$Q(\hbar\omega) = \frac{G_{polymer}}{G_{blend}} \frac{1}{1-\eta_{PET}}. \tag{2.4}$$

From this, the part of excitons which dissociate before recombination η_{PET} can be calculated:

$$\eta_{PET} = 1 - \frac{1}{Q(\hbar\omega)} \frac{G_{polymer}}{G_{blend}}. \tag{2.5}$$

Further, the generation rates $G_{polymer}$ and G_{blend} are proportional to the intensity of pump beam I_{pump}:

$$G_{polymer} = A_{polymer} I_{pump}, \tag{2.6}$$

$$G_{blend} = A_{blend} I_{pump}, \tag{2.7}$$

where $A_{polymer}$ and A_{blend} are the parts of light absorbed by the conjugated polymer and the conjugated polymer/fullerene film, respectively. These quantities can be calculated from a 3-phase model (see appendix A). In further consideration, the correction factor

$$K = \frac{A_{blend}}{A_{polymer}} \tag{2.8}$$

is used. Finally, the Eq. (2.5) can be written as:

$$\eta_{PET} = 1 - \frac{1}{KQ(\hbar\omega)}. \tag{2.9}$$

A very efficient photoinduced electron transfer was found in MEH-PPV/PCBM composites. The photoinduced electron transfer in this material system occurs in less than 45 fs [35]. In [36] it was shown, that addition of only 1 mol% of C_{60} to MEH-PPV leads to the quenching of photoluminescence by factor 5. From (2.9) one obtains for the MEH-PPV/C_{60} composites the efficiency of the photoinduced charge transfer $\eta_{PET} = 80\%$ (correction factor $K = 1$ is assumed). Thus, a minimal amount of fullerene is sufficient for effective charge separation in conjugated polymer/fullerene composites.

A primary drawback of solar cells based on conjugated polymer/fullerene composites is an energy loss ΔE_{TR}, which is the difference between the conduction band edge of the conjugated polymer and the LUMO level of the fullerene:

$$\Delta E_{TR} = E_{CB}^{polymer} - E_{LUMO}^{fullerene}. \tag{2.10}$$

For MDMO-PPV/PCBM and P3HT/PCBM solar cells, the ΔE_{TR} is 0.9 and 0.2 eV, respectively [37, 38]. In [37] it was shown, that even very low energy difference $\Delta E_{TR} = 0.17$ eV is already sufficient for effective electron transfer between the conjugated polymer and the fullerene.

2.2.2 Morphology and charge transport

The absorber layer of plastic solar cells is a conjugated polymer/fullerene blend. For effective transport of positive/negative charges to the electrodes, a bicontinuous conjugated polymer/fullerene network with percolation to the corresponding electrodes is necessary. It is known theoretically, that a fullerene fraction of only 16%, which is called "percolation limit" in 3D case for spherical particles, should be sufficient to transport all the electrons in active layer to the electrode [11]. However, in practice the polymer/fullerene layers with much higher (up to 80 wt.%) concentrations of fullerene are used. The reason for this is the enhanced phase separation between the conjugated polymer and the fullerene phases. It was shown by TEM [9, 8] and SEM [10] measurements, that the MDMO-PPV/PCBM films with low fullerene fraction (<60%) exhibit a very homogeneous morphology. The phase separation in such films can not be observed within the limits of TEM resolution (Fig. 2.6a).

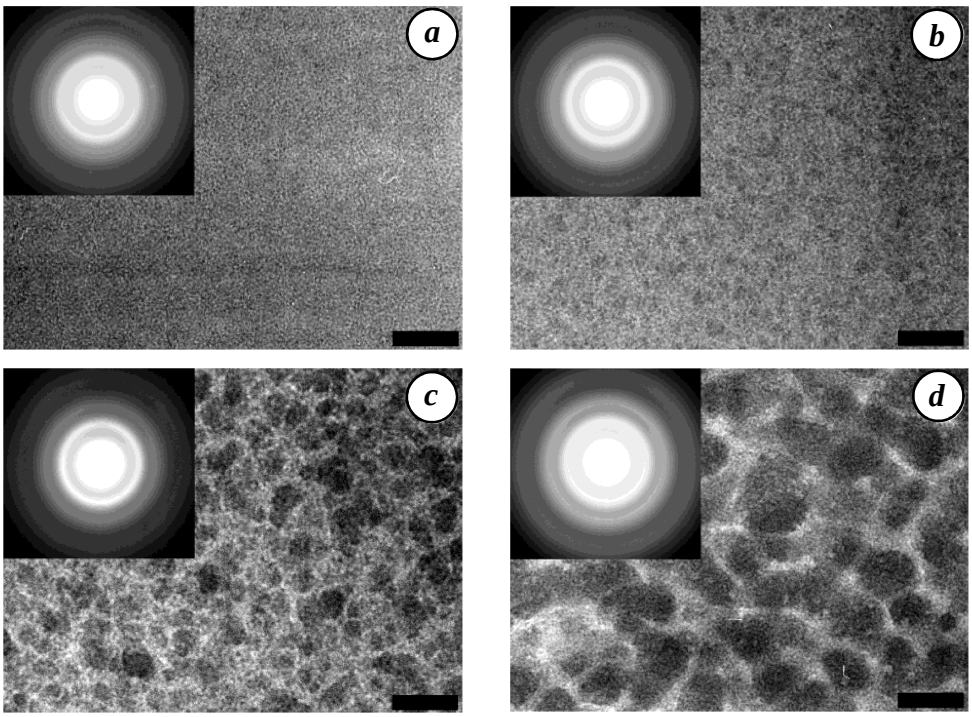

Figure 2.6: TEM images (scale bar: 200nm) of MDMO-PPV/PCBM films with PCBM concentrations of a) 60, b) 75, c) 80 and d) 90 wt.% [8].

With increased PCBM concentrations, the phase separation between two components becomes clearly visible (Fig. 2.6b-d). The average PCBM cluster size is increased up to nearly 160 nm for PCBM concentration of 90% for the

films spin coated from chlorobenzene solution. It is supposed, that for samples with low PCBM concentrations PCBM molecules are very fine dispersed in conjugated polymer matrix . For higher PCBM concentrations, the PCBM molecules aggregate into large PCBM-rich clusters [9, 10], resulting in the observed by AFM, SEM and TEM phase separation. The degree of the phase separation depends strongly on preparation conditions like fullerene concentration, solvent type or thermal treatment (annealing). For example, the average size of fullerene clusters in composite MDMO-PPV/PCBM films was found to be nearly 500 nm using toluene and about 50 nm when prepared from chlorobenzene solution (see Fig. 2.7).

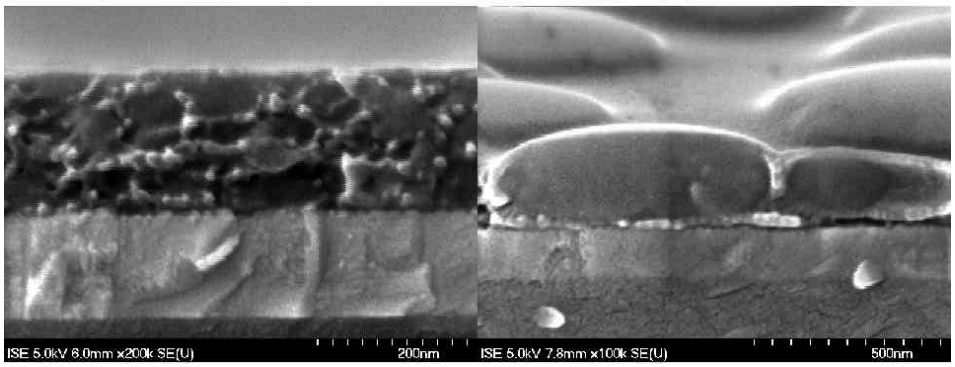

Figure 2.7: SEM images of MDMO-PPV/PCBM composite films (PCBM fraction is 80 wt.%) spin coated from chlorobenzene (left) and toluene (right) solutions. The dark areas are attributed to PCBM clusters [10].

It is commonly assumed, that the phase separation between conjugated polymer and fullerene is needed in order to prevent fast recombination of charge carriers. Moreover, the phase separation has a positive effect on charge carrier mobilities. Choulis et. al. [19] reported, that both electron and hole mobilities in MDMO-PPV/PCBM blend are increasing with increasing PCBM concentration in the blend (at least up to a PCBM concentration of 80 wt.%). The improvement in electron mobility with increasing concentration of PCBM was explained by the growth of PCBM network. The reason for the improvement in hole mobility remains unclear.

2.3 Operation of plastic solar cells

The configuration of plastic solar cell and typical layer thicknesses are shown in Fig. 2.8. The substrate consists of glass plate or polyethylenether-phtalate (PET) foil. Both glass and PET are transparent in the visible region. The substrate is coated with a thin indium tin oxide (ITO) layer, which works as a transparent electrode. The intermediate poly(3,4-ethylendioxythiophene):poly(styrensulfonate (PEDOT:PSS) layer is needed in order to flatten a rough surface of the ITO layer and thus to improve the contact to the active layer. On the other hand, the increased work function of PEDOT:PSS in comparison to this of ITO is desired to increase the open circuit voltage of the device. The active layer consists of the polymer/fullerene blend with fullerene fraction up to 80 wt.%. Thin interface LiF layer is used to increase the fill factor and the open circuite voltage of the plastic solar cell [39]. The solar cell is illuminated from the substrate-side.

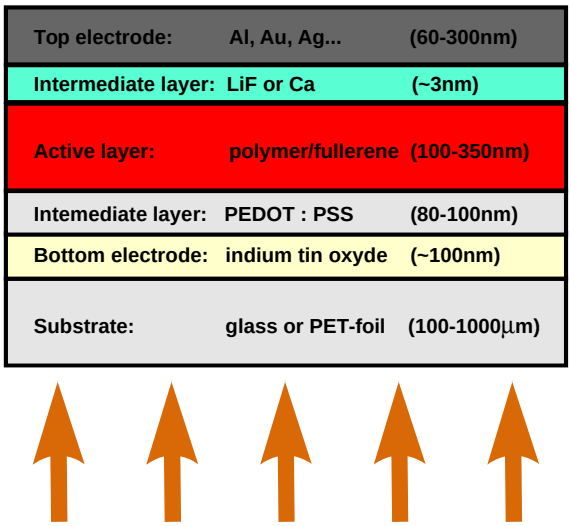

Figure 2.8: Configuration of conjugated polymer/fullerene solar cell.

The operation of the plastic solar cell is as follows. Sun light passes the substrate and the transparent ITO/PEDOT:PSS electrode. Then it is absorbed by the polymer in the active layer (see Fig. 2.9). The absorbed photons create the excitons on conjugated polymer chains. Then the excitons dissociate due to the photoinduced electron transfer from the polymer chain to the fullerene. As a result, positive polarons on the polymer chains and electrons on the fullerene molecules are formed. Due to build-in electric field, the electrons move towards the Al electrode by hopping from one fullerene molecule to another, while the

positive polarons are transported by the polymer chains to the ITO electrode. The charge carriers, which reach the electrodes, produce the electrical current in an outer circuit.

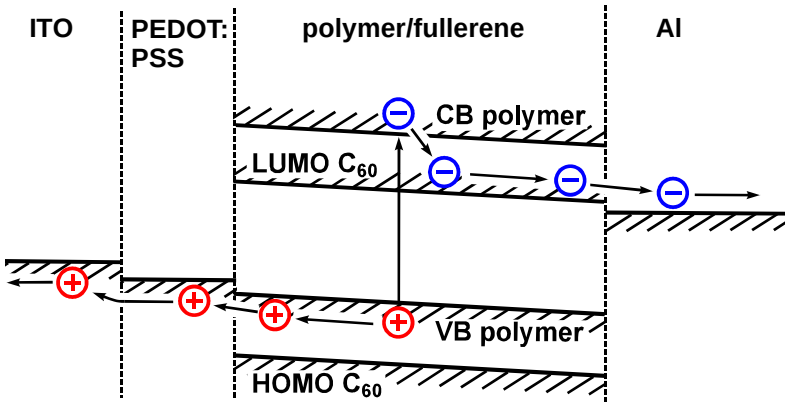

Figure 2.9: Schematic band diagram and charge transport in conjugated polymer/fullerene solar cell.

Chapter 3

Challenges of this work

3.1 Requirements on optical absorption and charge transport

The short circuit current of plastic solar cells is mainly determined by absorption of light and by transport of the separated charges to the electrodes.

In order to achieve effective absorption of the incident light, the thickness D of the active layer should be chosen as:

$$D > 1/\alpha_{blend}^{max}, \tag{3.1}$$

where α_{blend}^{max} is the maximum of the absorption coefficient of the conjugated polymer/fullerene blend (see Appendix D for more detail).

On the other hand, the condition of efficient charge carrier transport can be written as (see Appendix B):

$$\mu_{e(h)}\tau_{e(h)} \gg D^2/V_{OC}, \tag{3.2}$$

where $\mu_{e(h)}$ and $\tau_{e(h)}$ are electron (hole) mobility and lifetime, respectively, and V_{OC} is the open circuit voltage. Combining these two equations, one obtains:

$$\mu_{e(h)}\tau_{e(h)}(\alpha_{blend}^{max})^2 \gg 1/V_{OC}. \tag{3.3}$$

It can be easily proven, that the MDMO-PPV/PCBM solar cells do not fulfill the condition (3.3). Applying the literature data for hole mobility $\mu_h \sim 5 * 10^{-6}$ cm^2/Vs [19], lifetime $\tau_h \sim 10$ μs [40], open circuit voltage $V_{OC} \sim 1$ V and absorption coefficient $\alpha_{blend}^{max} \sim 5 * 10^4$ cm^{-1} , one obtains for the left side of (3.3) 0.125 V^{-1}, which is much lower than $1/V_{OC}$ (1 V^{-1}). For P3HT/PCBM solar cells,

the absence of reliable mobility data for P3HT in blend with PCBM do not allow us to calculate the left side of (3.3). Most likely, the $\mu_{e(h)}\tau_{e(h)}(\alpha_{blend}^{max})^2$ product yields higher value due to the improved hole mobility of P3HT in comparison to MDMO-PPV. Nevertheless, the $\mu_{e(h)}\tau_{e(h)}(\alpha_{blend}^{max})^2$ product is still too low even assuming ten times higher hole mobility than that for MDMO-PPV. Thus, the efficiency of P3HT/PCBM is limited by charge transport and optical absorption.

The condition (3.3) can be satisfied by optimisation of transport ($\mu_{e(h)}$ and $\tau_{e(h)}$) and/or optical α_{blend}^{max} properties of the blend. In this work we focus on the influence of structure of the active layer on its optical and transport properties.

3.2 Structure–property relation

In the case of MDMO-PPV/PCBM solar cells, the solar cell performance depends on the mean size of PCBM clusters. The highest efficiency was achieved for solar cells prepared by spin coating from chlorobenzene solution with PCBM concentration of 80 wt.%, which results in mean PCBM cluster size of 50-100 nm [8, 3]. The PCBM concentration affects the transport properties of the MDMO-PPV/PCBM blend, i. e. with increased PCBM concentration both electron and hole mobilities are increasing [19]. If the PCBM clusters become too large, the losses due to exciton recombination are increasing. It was concluded [41], that moderate phase separation between MDMO-PPV and PCBM is needed to balance exciton dissociation and charge transport requirements. It should be pointed out, that the optical absorption of MDMO-PPV/PCBM blend does not depend on the film morphology [3].

On the contrary to MDMO-PPV/PCBM, the optical properties of P3HT/PCBM composites are strongly affected by the film structure. In [42], the significant increase (factor 1.5 - 3 at λ =500 nm, depending on the annealing time) of optical absorption of P3HT/PCBM thin films upon annealing at elevated temperature (130°C) was reported. At the same time, the solar cell efficiency is improved from 0.4% to 2.5% upon annealing [4]. This unproportional increase of the solar cell efficiency was explained by simultaneous increase of charge carrier mobilities and raise of optical absorption. It was presumed that this is due to enhanced crystallisation of the P3HT during the annealing [4]. In fact, it is known that the polythiophenes tend to form crystalline domains in pure films [43, 44]. However, no experimental evidence of the P3HT crystallisation in P3HT/PCBM blends was provided yet. Thus, the origin of increased optical

absorption of annealed P3HT/PCBM films remains unclear.

Since both optical and transport properties of P3HT/PCBM films depends on film structure, this material system is of great interest for studying of structure–property relation. In comparison to MDMO-PPV/PCBM, the structure of P3HT/PCBM films is not very good investigated. Therefore the relation between structure of P3HT/PCBM films and their optical and transport properties was studied in this work.

3.3 Anisotropy in conjugated polymer films

One of the intentions and speciality of this work was to study the optical anisotropy in conjugated polymer and conjugated polymer/fullerene films. The motivation for this is that the optical anisotropy provides the information about the orientation of polymer molecules within the film. Since the π-electrons are delocalised along the polymer chain and limited in two other directions, conjugated polymer molecules have a highly anisotropic polarisability. The anisotropic polarisability can reveal itself in macroscopic properties of the material if, for example, there is a preferable orientation of the molecules. Indeed, a very high anisotropy of optical properties was demonstrated in case of aligned polymer films, where polymer molecules are oriented parallel to the draw axis. In this case, the optical absorption is the highest parallel to the draw axis. For instance, the absorption anisotropy as high as 50/1 for light polarised parallel/perpendicular to the draw direction was reported by D. Comoretto *et. al.* [45] for highly stretch-oriented MEH-PPV films.

For thin spin-coated and drop-cast films of some conjugated polymers, uniaxial optical anisotropy with the optical axis perpendicular to the surface was reported [46, 47, 48, 49, 50, 51]. This phenomenon was related to the preferable orientation of the polymer chains parallel to the substrate. This assumption was also confirmed by X-ray diffraction measurements on thin spin-coated poly(3-alkylthiophene) films [43, 44]. The degree of the optical anisotropy depends on the angular distribution of the chains, i.e. the higher optical anisotropy corresponds to the better alignment of the chains parallel to the substrate.

It was also shown, that the charge transport in conjugated polymers is affected by orientation of polymer chains. In the case of oriented poly(3-dodecylthiophene) films, the hole mobility parallel to the polymer backbone one order of magnitude larger than that for orthogonal direction [18] was reported.

A correlation between the orientation of the polymer chains and the anisotropic conductivity was demonstrated [52, 53, 54] in other cases, too.

In spite of importance of these findings, there is only limited number of publications related to the optical anisotropy of conjugated polymer films. The influence of growth parameters such as spin frequency, concentration of the polymer in the solvent and solvent type on the optical anisotropy was not reported yet. To our knowledge, the optical anisotropy of conjugated polymer/fullerene blends was not investigated at all.

The information about the orientation of the polymer molecules can be in principle obtained by X-ray diffration measurements, too. However, in comparison to XRD the optical characterisation has some important advantages. First of all, the quantitative results about the orientation of polymer molecules or crystallites could be obtained. For instance, the increase of a diffraction peak corresponding to orientation of the polymer crystallites parallel to the substrate could be caused either by increased number of crystallites or by their reorientation. On the other hand, the increase of optical anisotropy means that the polymer molecules (or crystallites) become on average more oriented parallel to the substrate. Another advantage of the optical characterisation over the XRD analysis is that the XRD analysis do not provide any structural information for non-crystalline films, where optical characterisation still works.

Chapter 4

Materials

The investigated samples consist of the conjugated polymer or conjugated polymer/fullerene films, deposited on Si or glass substrates.

Among the conjugated polymers, poly(3-octylthiophene) (P3OT) and poly(3-octylthiophene) P3HT (see Fig. 4.1) were studied. The polymers were purchased by Aldrich.

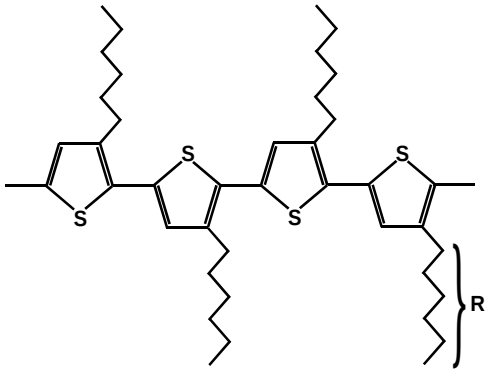

Figure 4.1: Chemical structure of poly(3-alkylthiophene) P3DDT, P3OT and P3HT.

The substituted fullerene [6,6]-phenyl-C61-butyric acid methyl ester (PCBM, see Fig. 4.2) used in this work was synthesized in the group of Prof. J. C. Hummelen at the University of Groningen (Netherlands).

Thin P3OT films were prepared by Harald Hoppe (Linz Institute of Organic Solar Cells (LIOS)). By the preparation of these samples, parameters like spin frequency, polymer concentration, solvent, substrate, etc. were varied. The influence of these parameters on optical properties was systematically investigated.

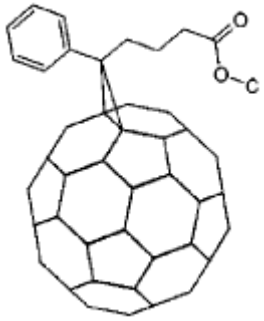

Figure 4.2: Chemical structure of PCBM.

The effect of annealing on optical and structural properties of pristine P3HT and P3HT/PCBM composite films was studied in collaboration with Siemens AG Erlangen (Pavel Schilinsky, Christoph Waldauf and Christoph Brabec, department CT MM 1) and LIOS Linz (Harald Hoppe, Niyazi Serdar Sariciftci).

Influence of annealing temperature on crystallinity and optical absorption of P3HT/PCBM composite films was investigated in collaboration with Centre for Micro- and Nanotechnologies (ZMN), Ilmenau. The samples for this study were prepared by Maher Al-Ibrahim.

Chapter 5

Experimental Methods

5.1 Spectroscopic ellipsometry

Spectroscopic ellipsometry (SE) is a primary technique for determination of dielectric function (see section 5.1.1) and thicknesses of materials in layered samples. SE allows to measure the change in polarisation state of light reflected from the surface of the sample. SE is more accurate than intensity reflectance (or transmittance) measurements because the absolute intensity of light reflected (passed) through the sample does not have to be measured.

Generally, the determination of optical constants with SE could be divided in following 4 steps [55]:

- Measurement of ellipsometric angles Ψ_{meas} and Δ_{meas}. This step is described in sections 5.1.2 and 5.1.3).
- Development of an optical model for the measured sample and calculation of the Ψ_{model} and Δ_{model} from this model (section 5.1.4).
- Fit of the model parameters to measured data by minimisation of the mean-square error between calculated (Ψ_{model}, Δ_{model}) and measured (Ψ_{meas}, Δ_{meas}) data (section 5.1.5).
- Examination of best-fit model parameters (section 5.1.5).

5.1.1 Dielectric function

From Maxwell's equations, the wave equation for electric field vector **E** can be obtained [56]:

$$\Delta\mathbf{E} = \frac{\mu\varepsilon}{c^2}\frac{\partial^2\mathbf{E}}{\partial t^2}, \tag{5.1}$$

where c, ε and μ are the velocity of light in vacuum, the dielectric function (DF) and the magnetic permeability, respectively. The simplest solution of the eq. 5.1 is a harmonic plane wave propagating for example in direction determined by unit vector $\mathbf{q}$:

$$\begin{pmatrix} E_X \\ E_Y \\ E_Z \end{pmatrix} = \begin{pmatrix} E_X^0 \cos\left(\frac{2\pi n}{\lambda}\mathbf{q}\cdot\mathbf{r} - \omega t + \phi_X^0\right) \\ E_Y^0 \cos\left(\frac{2\pi n}{\lambda}\mathbf{q}\cdot\mathbf{r} - \omega t + \phi_Y^0\right) \\ E_Z^0 \cos\left(\frac{2\pi n}{\lambda}\mathbf{q}\cdot\mathbf{r} - \omega t + \phi_Z^0\right) \end{pmatrix} \tag{5.2}$$

where w is the angular frequency of the wave, E_0^X, E_0^Y E_0^Z are constants, ϕ_0 is the phase angle and $n = \sqrt{\mu\varepsilon}$ is the refractive index of the medium. This equation can be written in complex form

$$\mathbf{E}(\mathbf{r},t) = \mathrm{Re}\left[\tilde{\mathbf{E}}_0 \exp\left(i\frac{2\pi n}{\lambda}\mathbf{q}\cdot\mathbf{r}\right)\exp(-i\omega t)\right], \tag{5.3}$$

where $\tilde{\mathbf{E}}^0 = \begin{pmatrix} E_X^0\exp(i\phi_X^0) \\ E_Y^0\exp(i\phi_Y^0) \\ E_Z^0\exp(i\phi_Z^0) \end{pmatrix}$ is a complex vector specifying the amplitude and the polarisation state of the wave. Since for most semiconducting and insulating materials the magnetic permeability μ is nearly unity ($\mu = 1 \pm 10^{-4}$, see for example [57]), the refractive index equals the square root of the DF

$$n = \sqrt{\varepsilon}, \tag{5.4}$$

which is a real number for non-conductive, non-dispersive, isotropic materials considered before. In order to describe absorbing and/or conducting materials, one introduce the complex DF $\tilde{\varepsilon} = \varepsilon_1 + i\varepsilon_2$ and complex refractive index $\tilde{n} = \sqrt{\tilde{\varepsilon}} = n + ik$. If the imaginary part of the DF (or of the complex refractive index) is not zero, the intensity of the wave will decay as it propagates

$$I \sim \mathbf{E}^2 \sim \exp\left(-\frac{4\pi k}{\lambda}z\right). \tag{5.5}$$

Comparing this with Lambert-Beer's law

$$I(z) = I(0)\exp(-\alpha z), \tag{5.6}$$

we find for the absorption coefficient α

$$\alpha = \frac{4\pi k}{\lambda}. \tag{5.7}$$

Applying the equations $\varepsilon_2 = 2nk$ and $\lambda = 2\pi c/\omega$ to (5.7), one obtains

$$\alpha = \frac{\varepsilon_2 \omega}{nc}. \tag{5.8}$$

The complex DF $\tilde{\varepsilon}$ completely describes the propagation, reflection, refraction and absorption of electromagnetic wave in materials and multi-layer structures. Therefore the precise determination of $\tilde{\varepsilon}$ is of great importance for the design of highly efficient optoelectronic devices.

For anisotropic materials the equation $\mathbf{D} = \varepsilon\varepsilon_0\mathbf{E}$ is applicable in the form

$$\mathbf{D} = \varepsilon_0\hat{\varepsilon}\mathbf{E}, \tag{5.9}$$

where $\hat{\varepsilon} = \begin{pmatrix} \tilde{\varepsilon}_{XX} & \tilde{\varepsilon}_{XY} & \tilde{\varepsilon}_{XZ} \\ \tilde{\varepsilon}_{YX} & \tilde{\varepsilon}_{YY} & \tilde{\varepsilon}_{YZ} \\ \tilde{\varepsilon}_{ZX} & \tilde{\varepsilon}_{ZY} & \tilde{\varepsilon}_{ZZ} \end{pmatrix}$ is the tensor of DF. From Eq. (5.9) follows, that the vector of electric displacement is generally not parallel to the electric vector in medium.

For uniaxial materials in a coordinate system with the z-axis parallel to the optical axis, the tensor of the DF has the form:

$$\hat{\varepsilon} = \begin{pmatrix} \tilde{\varepsilon}_o & 0 & 0 \\ 0 & \tilde{\varepsilon}_o & 0 \\ 0 & 0 & \tilde{\varepsilon}_e \end{pmatrix}. \tag{5.10}$$

The propagation of light in such a material can be described by ordinary $\tilde{\varepsilon}_o$ and extraordinary $\tilde{\varepsilon}_e$ DF's for the light polarised perpendicular and parallel to the optical axis, respectively.

5.1.2 Jones matrix formalism

In ellipsometric experiments it is common to use the p- and s- directions as the two orthogonal basis vectors to express beam polarisation states. The p- direction is defined as lying in the plane of incidence (which is the plane containing the incidence and reflected beams and the vector normal to the sample surface). The s- direction lies perpendicular to the p- direction such that the p- direction, s- direction and direction of propagation define a right-handed cartesian coordinate system. In this case, the z- component of the electric field is always zero

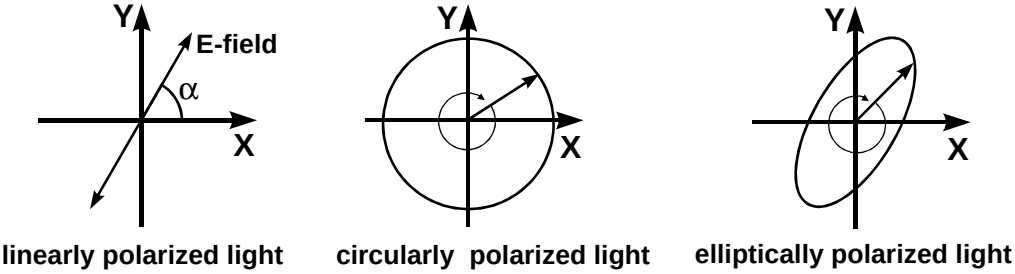

Figure 5.1: Linear, circular and elliptical polarisation of light.

because the electric field vector lies in the plane perpendicular to the direction of propagation. So one can express any polarised beam by specifying only the p- and s- components of the complex vector $\tilde{\mathbf{E}}^0$. These two components are complex numbers, which can be written as a two component vector ("Jones vector" [58])

$$\tilde{\mathbf{E}} = \begin{pmatrix} \tilde{E}_P \\ \tilde{E}_S \end{pmatrix}. \tag{5.11}$$

Fig. 5.1 shows the orientation of the electric field with respect to the coordinate system for linear, circular and elliptical polarisation. The Jones vector is $\begin{pmatrix} \cos\alpha \\ \sin\alpha \end{pmatrix}$ for linearly and $\begin{pmatrix} 1 \\ i \end{pmatrix}$ for circular polarised light. Any other Jones vector describes elliptically polarised light. For example, elliptical polarisation shown in Fig. 5.1 is described by Jones vector $\begin{pmatrix} 1 \\ 1+i \end{pmatrix}$.

The influence of any sample on the polarisation state can be described then by means of 2×2 complex matrix ("Jones matrix")

$$\begin{pmatrix} \tilde{E}_P^R \\ \tilde{E}_S^R \end{pmatrix} = \begin{pmatrix} \tilde{R}_{PP} & \tilde{R}_{PS} \\ \tilde{R}_{SP} & \tilde{R}_{SS} \end{pmatrix} \begin{pmatrix} \tilde{E}_P^I \\ \tilde{E}_S^I \end{pmatrix}, \tag{5.12}$$

where $\begin{pmatrix} \tilde{E}_P^I \\ \tilde{E}_S^I \end{pmatrix}$ and $\begin{pmatrix} \tilde{E}_P^R \\ \tilde{E}_S^R \end{pmatrix}$ are the Jones vectors describing the polarisation of incident and reflected beams, respectively, and $\begin{pmatrix} \tilde{R}_{PP} & \tilde{R}_{PS} \\ \tilde{R}_{SP} & \tilde{R}_{SS} \end{pmatrix}$ is the Jones matrix of the sample. The complex coefficients $\tilde{R}_{PP}$, $\tilde{R}_{PS}$, $\tilde{R}_{SP}$ and $\tilde{R}_{SS}$ describe the change of the amplitude and phase of the light beam upon reflection. If the sample is isotropic, the off-diagonal elements of the Jones matrix vanish ($\tilde{R}_{PS} = \tilde{R}_{SP} = 0$). That means, no conversion of p- polarised light into s-polarised and vice versa occurs. In case of anisotropic sample, the Jones matrix generally exhibits off-diagonal elements.

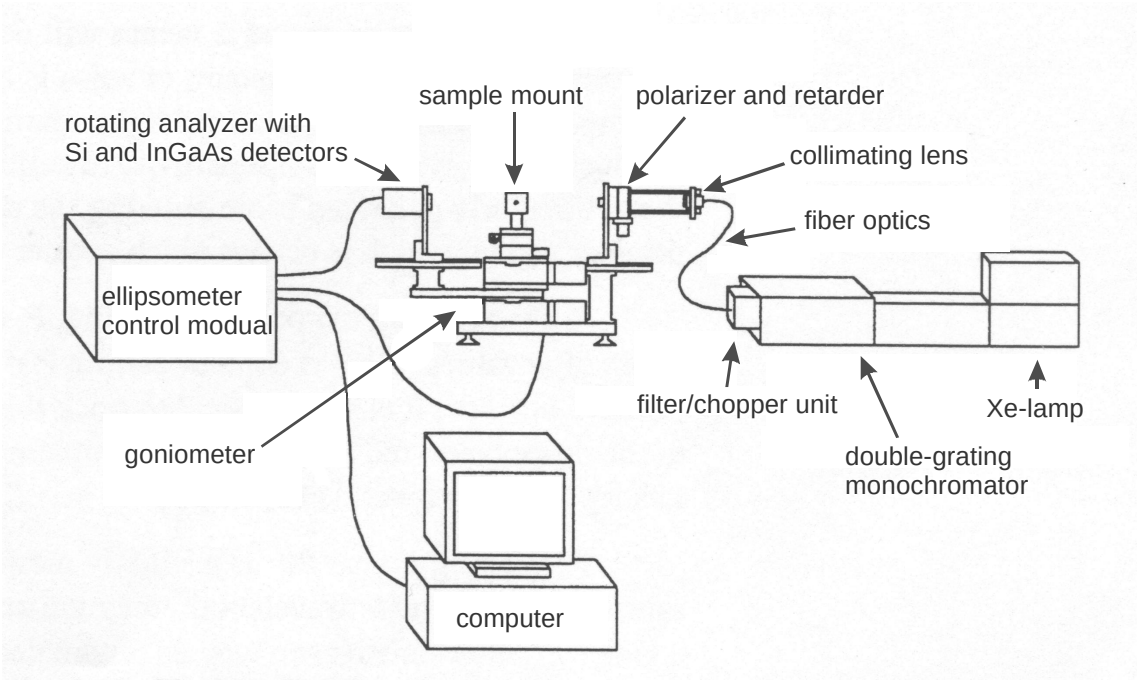

Figure 5.2: Configuration of the Woollam VASE rotating analyser ellipsometer.

5.1.3 Measurement of the ellipsometric angles with rotating analyser ellipsometer (RAE)

The ellipsometric parameter ρ is defined as the ratio of the complex diagonal elements of the Jones matrix 5.12

$$\tilde{\rho} \equiv \frac{\tilde{R}_{PP}}{\tilde{R}_{SS}}. \tag{5.13}$$

$\tilde{\rho}$ can be also presented in terms of two real ellipsometric parameters Ψ and Δ as follows:

$$\tilde{\rho} = \tan\Psi \exp(i\Delta). \tag{5.14}$$

The ellipsometric measurements were performed by Woollam VASE variable angle spectroscopic ellipsometer with rotating analyser. The VASE ellipsometer (Fig. 5.2) consists of the light source (xenon arc lamp, monocromator, chopper, filter wheel, fiber optics), input unit (collimating lens (quartz), polariser, retarder), sample mount, detector unit (rotating analyser, stacked Si/AlGaAs detector, pre-amplifier), control unit and computer [55].

A 75 watt xenon high-pressure arc lamp is used as light source. The radiation of the lamp is focused by an elliptical reflector on the entry slit of the monochromator. The beam chopper and the filter wheel are placed at the output of the monochromator.

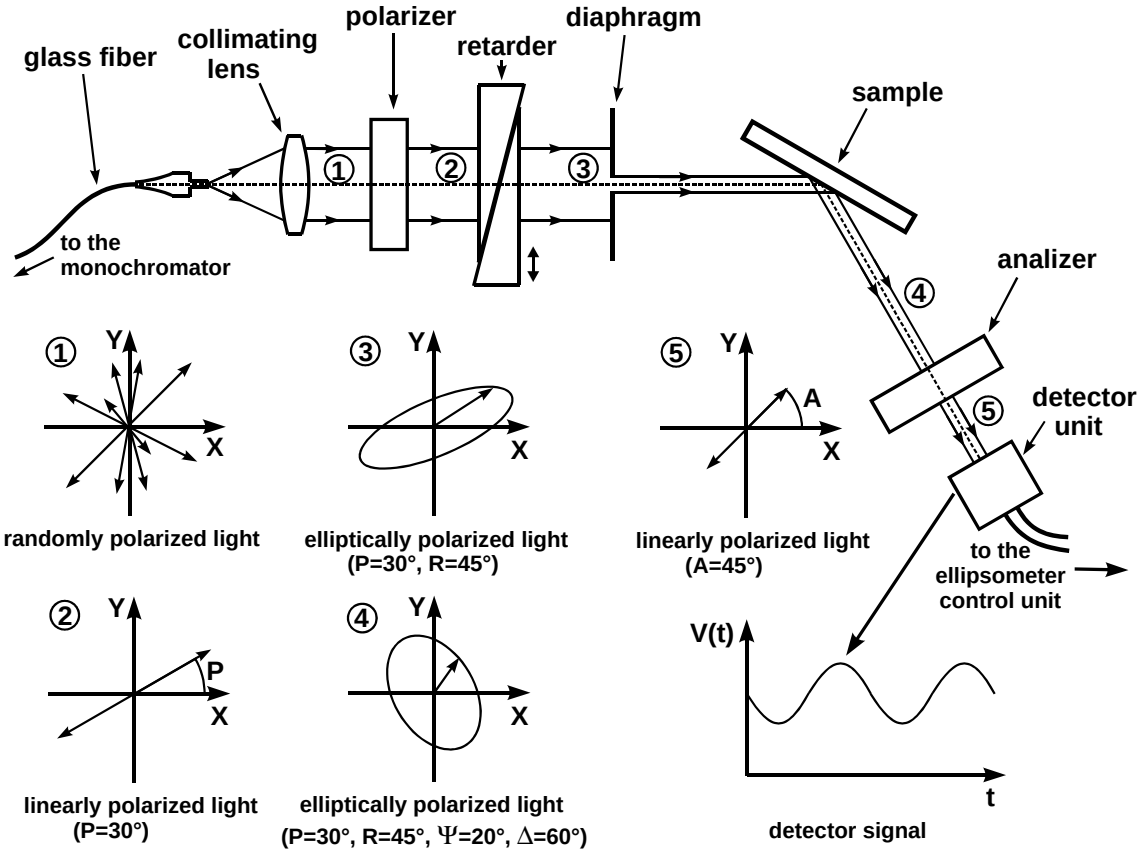

Figure 5.3: Optical scheme of the Woollam VASE ellipsometer and the polarisation states.

The unpolarised monochromatic light passed through the polariser becomes linearly polarised (see the onset 2 on 5.3). The retarder introduces the phase shift between p- and s- components. This results in an elliptically polarised light (onset 3, see also section 5.1.2). The incident beam is then reflected from the sample. The polarisation state changes upon the reflection (onset 4). The polarisation state of the reflected beam is then measured by combining the rotating polariser with a semiconductor detector (onset 5).

It can be shown [55], that for a general elliptical polarisation the detected signal is a sinusoid with constant offset:

$$V(t) = C + A\cos(2ft) + B\sin(2ft), \tag{5.15}$$

where f is the angular frequency of rotating analyser. The normalised Fourier coefficients $\alpha = A/C$ and $\beta = B/C$ can be represented in terms of the Ψ and Δ values of the sample, the polariser angle P and retardation R as follows:

$$\alpha = \frac{\tan^2\Psi - \tan^2 P}{\tan^2\Psi + \tan^2 P} \tag{5.16}$$

$$\beta = \frac{2\tan\Psi\cos(\Delta + R)\tan P}{\tan^2\Psi + \tan^2 P} \tag{5.17}$$

The solution for Ψ and Δ as functions of α and β gives:

$$\tan\Psi = \sqrt{\frac{1+\alpha}{1-\alpha}}|\tan P| \tag{5.18}$$

$$\cos(\Delta + R) = \frac{\beta}{\sqrt{1-\alpha^2}}\frac{\tan P}{|\tan P|} \tag{5.19}$$

Thus, in ellipsometric measurements the detector signal is measured as a function of time, the measured signal is Fourier analysed to obtain the Fourier coefficients α and β, and finally Ψ and Δ are calculated from α, β and known angles P and R.

Ellipsometric data were obtained by means of a Woollam variable angle spectroscopic ellipsometer (VASE) with rotating analyser (RAE) in spectral region from 1.2 to 5.0 eV in steps of 0.02 eV. The spectral resolution was 3 nm (0.01 eV at $\hbar\omega = 2.0$ eV). The measurements were performed at several angles of incidence in the range of 60-75° at room temperature in air. During the ellipsometric measurements the samples were illuminated with low-intensity monochromatic light and therefore the photooxidation rate should be low. This assumption was checked by repeating the ellipsometric measurements; no changes in the $(\Psi - \Delta)$ spectra were observed.

5.1.4 Reflection of light from planar layered system

Before the analysis of the measured experimental data, the ellipsometric angles Ψ_{model} and Δ_{model} must be calculated from the chosen optical model.

As a rule, the investigated samples consist of a thin film, deposited on a well-known substrate (like glass, Si, or GaAs) with known DF $\tilde{\varepsilon}_0$ as shown in Fig. 5.4. The investigated polymer films are uniaxially anisotropic with optical axis perpendicular to the film plane. The propagation of light in such a film can be described by two DF's $\tilde{\varepsilon}_{||}$ and $\tilde{\varepsilon}_{\perp}$ for the light polarised parallel and perpendicular to the substrate, respectively (cp. Eq. (5.10)). For an uniaxial film deposited on an isotropic substrate (which is the case for samples studied here) one obtains for the diagonal elements of the Jones matrix [58]

$$\tilde{R}_{PP} = \frac{\tilde{R}^{01}_{PP} + \tilde{R}^{12}_{PP}\exp(i2\beta_P)}{1 + \tilde{R}^{01}_{PP}\tilde{R}^{12}_{PP}\exp(i2\beta_P)}, \tag{5.20}$$

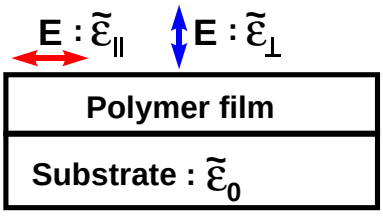

Figure 5.4: Configuration of the investigated samples for the SE measurement.

$$\tilde{R}_{SS} = \frac{\tilde{R}_{SS}^{01} + \tilde{R}_{SS}^{12} \exp(i2\beta_S)}{1 + \tilde{R}_{SS}^{01}\tilde{R}_{SS}^{12} \exp(i2\beta_S)}, \tag{5.21}$$

where β_P and β_S are the phase shifts, $\tilde{R}_{PP}^{01}$, $\tilde{R}_{PP}^{12}$, $\tilde{R}_{SS}^{01}$ and $\tilde{R}_{SS}^{12}$ are the Fresnel coefficients for the reflection of light at the air-film and film-substrate interfaces, which can be written as

$$\tilde{R}_{PP}^{01} = \frac{\sqrt{\tilde{\varepsilon}_\parallel \tilde{\varepsilon}_\perp}\cos\phi - \sqrt{\tilde{\varepsilon}_\perp - \sin^2\phi}}{\sqrt{\tilde{\varepsilon}_\parallel \tilde{\varepsilon}_\perp}\cos\phi + \sqrt{\tilde{\varepsilon}_\perp - \sin^2\phi}}, \tag{5.22}$$

$$\tilde{R}_{PP}^{12} = \frac{-\sqrt{\tilde{\varepsilon}_\parallel \tilde{\varepsilon}_\perp}\sqrt{\tilde{\varepsilon}_s - \sin^2\phi} + \tilde{\varepsilon}_s\sqrt{\tilde{\varepsilon}_\perp - \sin^2\phi}}{\sqrt{\tilde{\varepsilon}_\parallel \tilde{\varepsilon}_\perp}\sqrt{\tilde{\varepsilon}_s - \sin^2\phi} + \tilde{\varepsilon}_s\sqrt{\tilde{\varepsilon}_\perp - \sin^2\phi}}, \tag{5.23}$$

$$\tilde{R}_{SS}^{01} = \frac{\cos\phi - \sqrt{\tilde{\varepsilon}_\parallel - \sin^2\phi}}{\cos\phi + \sqrt{\tilde{\varepsilon}_\parallel - \sin^2\phi}}, \tag{5.24}$$

$$\tilde{R}_{SS}^{12} = \frac{-\sqrt{\tilde{\varepsilon}_s - \sin^2\phi} + \sqrt{\tilde{\varepsilon}_\parallel - \sin^2\phi}}{\sqrt{\tilde{\varepsilon}_s - \sin^2\phi} + \sqrt{\tilde{\varepsilon}_\parallel - \sin^2\phi}}, \tag{5.25}$$

where ϕ is the angle of incidence. The phase shifts β_P and β_S can be expressed by

$$\beta_P = \frac{2\pi D}{\lambda}\sqrt{\tilde{\varepsilon}_\parallel - \frac{\tilde{\varepsilon}_\parallel}{\tilde{\varepsilon}_\perp}\sin^2\phi}, \tag{5.26}$$

$$\beta_S = \frac{2\pi D}{\lambda}\sqrt{\tilde{\varepsilon}_\parallel - \sin^2\phi}, \tag{5.27}$$

where D is the film thickness.

Using the Eqs. (5.20-5.27), the quantities Ψ_{model} and Δ_{model} now can be calculated:

$$\tan\Psi_{model}\exp(i\Delta_{model}) = \frac{\tilde{R}_{PP}}{\tilde{R}_{SS}}. \tag{5.28}$$

5.1.5 Analysis of measured data

It should be pointed out, that ellipsometry can not determine directly DF, film thickness or any other parameter of the investigated sample, because the obtained quantities Ψ_{exp} and Δ_{exp} are not directly significant. However, these quantities are affected by physical parameters of the sample (for example by film thickness, optical constants of the film, surface roughness, etc.). In order to obtain the parameters of a sample, an optical model containing unknown parameters ("fit parameters") for the sample must be taken as a basis. Then, the model parameters should be varied to obtain the best fit between experimental data and those calculated by the model. Consequently, the obtained best-fit parameters depend on the chosen optical model. That is why the choice of the optical model is a very critical part of the ellipsometric analysis.

The quantity which represents the quality of the match between the data calculated from the model and the experimental data called "mean square error" is determined as following

$$MSE = \frac{1}{N-M}\sum_{i=1}^{N}[(\frac{\Psi^i_{model}-\Psi^i_{exp}}{\sigma^i_\Psi})^2+(\frac{\Delta^i_{model}-\Delta^i_{exp}}{\sigma^i_\Delta})^2], \tag{5.29}$$

where σ^i_Ψ and σ^i_Δ are the standard deviations of the measured quantities Ψ^i_{exp} and Δ^i, respectively, N is the number of experimental points and M is the number of the fit parameters. MSE is a function of M fit parameters. During the fit, the fit parameters are varied in order to find the set of values for the fit parameters which yields an absolute minimum of the MSE. This optimisation problem is solved by using the Levenberg-Marquardt method, which is the combination of gradient and inverse Hessian methods [55].

After the fit is completed, the best-fit parameter values should be examined. First, the MSE could be insensitive to one or more fit parameters. For example, in the case of a thick absorbing film (where the penetration depth of the light is much smaller than the film thickness), the data generated from the model (and consequently the MSE) obviously don't depend on the film thickness. Therefore, the obtained fit value for the film thickness is not realistic, and the film thickness should be excluded from the fit parameter set. Another case is a parameter correlation. If the fit parameter set is too large, some parameters could correlate. The correlation means, that there are many sets of values of fit parameters, which provide a good fit to the experimental data. A basic requirement for the absence

of the parameter correlation is that the number of the fit parameter must not exceed the number of measured quantities available for the sample:

$$N_{fit\ parameters} \leq N_{experimental\ points}. \tag{5.30}$$

If the number of fit parameters exceeds the number of measured quantities, the fit is always correlated.

A classic example is a fit for the DF (ε_1, ε_2) of a thin film with unknown film thickness D. Generally, such a fit is highly correlated. For instance, one obtains a perfect fit to the experimental data at some fixed film thicknesses, as it shown in Fig. 5.5. The reason for the correlation is that the number of fit parameters exceeds the number of experimental points available for the fit. In fact, if one tries to determine the film thickness and the DF at N different photon energies, the number of measured quantities equals $2N$ (Ψ and Δ at each photon energy), while the number of fit parameters equals $2N + 1$ (ε_1, ε_2 at each photon energy plus film thickness D). Therefore the film thickness and the DF could not be determined simultaneously using only the ellipsometric data.

There are some possibilities to prevent the parameter correlation:

• The fit parameter set must be reduced. In our case, one should fit the experimental data with a fixed film thickness (the film thickness must be determined from another experiment like AFM or profilometry prior to the fit). The fit is possible because the number of fit parameters is equal to the number of experimental points $2N$.

• Independent experimental data must be added to the fit. For example, if reflectance and transmittance data for the sample are included in the fit, the number of the experimental points becomes $4N$ (Ψ, Δ, R and T at each photon energy) and is higher than the number of the fit parameters $2N + 1$.

• In the special case of a semiconductor film, the film thickness can be determined by fitting the real part of the DF ε_1 and the film thickness D in the transparent region below the band gap $\hbar\omega < E_G$. The imaginary part of the DF is fixed at $\varepsilon_2 = 0$ and can be excluded from the fit. The number of fit parameters is then reduced to $n + 1$ (ε_1 at each photon energy and the film thickness; n is the number of photon energies below the band gap), whereas the number of measured quantities remains $2n$. After the film thickness was determined from the fit in the transparent region of the spectrum, the fit for ε_1 and ε_2 (with known film thickness) in the non-transparent region above the gap can also be performed.

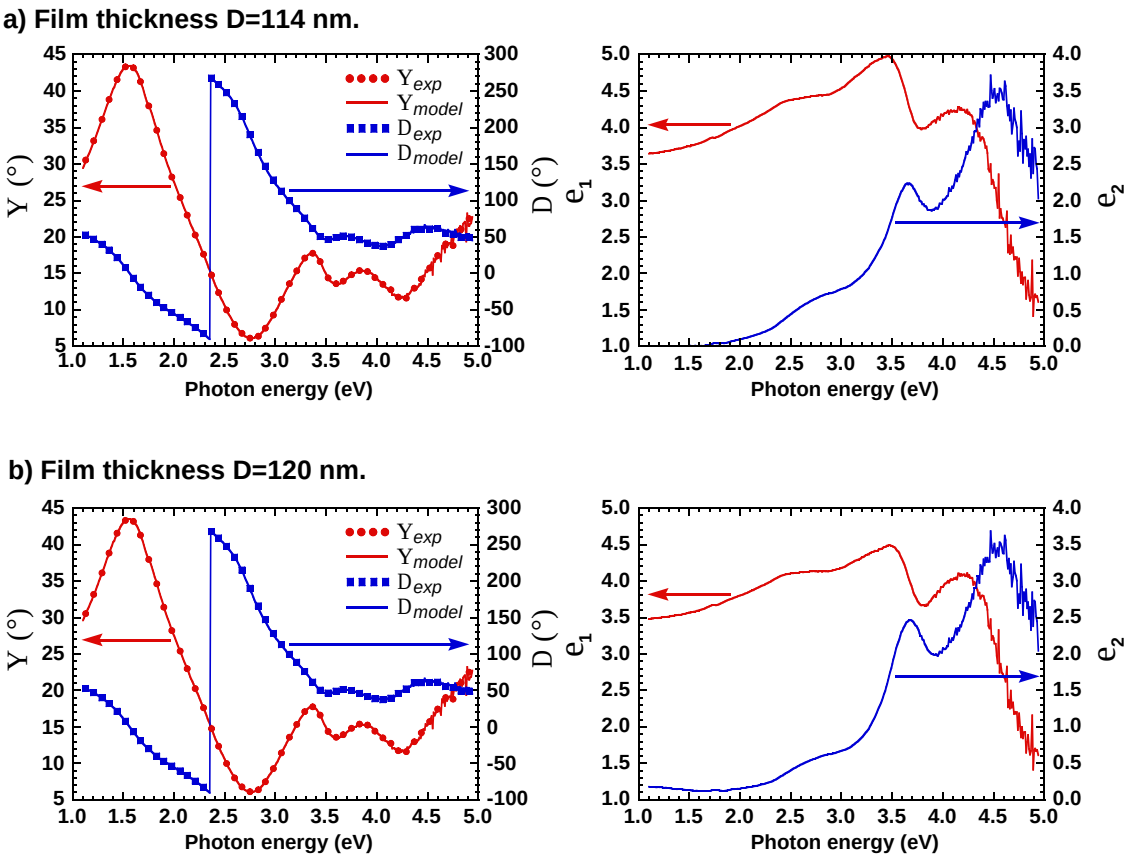

Figure 5.5: The fit of ellipsometric data with one-layer optical model (left) and the resulting DF's (right). During the fit, the film thickness was fixed at: a) 114 and b) 120nm.

In the case of an anisotropic uniaxial sample, both parallel $\tilde{\varepsilon}_{||} = \varepsilon_{1||} + i\varepsilon_{2||}$ and perpendicular $\tilde{\varepsilon}_{\perp} = \varepsilon_{1\perp} + i\varepsilon_{2\perp}$ components of the DF must be fitted. Because of a large $(4N+1)$ set of fit parameters ($\varepsilon_{1||}, \varepsilon_{2||}, \varepsilon_{1\perp}, \varepsilon_{2\perp}$ and film thickness D), the parameter correlation becomes the main problem. A simultaneous fit for all of these quantities is totally correlated. There are two approaches to solve this problem:

• **Using the multiple sample analysis (MSA)**. In multiple sample analysis, several films of the same material are simultaneously analysed assuming the same DF for all films, while the film thickness is allowed to be different for each sample. If K is the number of investigated samples, the number of measured quantities becomes $2KN$ (Ψ and Δ for each sample at each photon energy), while the number of the fit parameters $4N + K$ ($\varepsilon_{1||}, \varepsilon_{2||}, \varepsilon_{1\perp}, \varepsilon_{2\perp}$ and the film thicknesses $D_1 ... D_K$) increases only slightly with the increasing number of samples. Thus, the number of experimental points is effectively increased

without significant increase of the number of fit parameters. From (5.30) we get the condition for the absence of parameter correlation:

$$4N + K \leq 2NK. \tag{5.31}$$

Because of the large number of photon energies N Eq. (5.31) is true for $K \geq 3$. Thus, one can expect that the multiple sample analysis of 3 or more samples is uncorrelated.

In our work we analysed simultaneously three samples prepared from the same concentration of the solution, but using slightly different spin frequencies, which results in slightly different film thicknesses. The fitted anisotropic DF was then equalised to the DF of the sample with the mean spin frequency. It is supposed, that the obtained DF corresponds to the "mean" DF of the samples.

• **Including the reflectance/transmittance data to the fit (RTΨΔ-method)** (this method works only for films deposited on transparent substrates). The number of the measured quantities equals $4N$ (Ψ, Δ, R and T at each photon energy).

First, the film thickness is determined in the transparent region of the spectrum below the band gap. It is assumed, that there is no absorption below the gap ($\varepsilon_{2||} = 0, \varepsilon_{2\perp} = 0$), and only the real parts of the anisotropic DF $\varepsilon_{1||}, \varepsilon_{1\perp}$ and the film thickness D are fitted at this step. Because of the reduced number of fit parameters $2N + 1$, this fit is uncorrelated (see Eq. (5.30)).

Once the film thickness is determined from previous step, both real and imaginary parts of the anisotropic DF (i. e. $\varepsilon_{1||}, \varepsilon_{2||}, \varepsilon_{1\perp}, \varepsilon_{2\perp}$, altogether $4N$ parameters) are fitted with fixed film thickness D. The fit of the parallel and perpendicular components of the DF to the ellipsometric and reflectance/transmittance data was found to be uncorrelated in agreement with the condition (5.30).

In our work, both MSA and RTΨΔ-method were used. The results provided by these two methods were carefully proved by independent reflectance/transmittance measurements performed at the Johannes Kepler University Linz in Austria. The reflectance/transmittance measurements provide both the film thickness and the parallel component of the DF. The results of the reflectance/transmittance measurements were found to be in a good agreement with those of ellipsometric analysis. Additionally, the AFM data on scratched samples were taken to determine the film thickness. The good agreement of the film thickness provided by ellipsometry, AFM and reflectance/transmittance measurements indicates the reliability of the ellipsometric analysis.

A question arises whether the MSA analysis can be applied for characterisation of conjugated polymer films. The main assumption in MSA is that the optical properties of the films do not change with the film thickness. It will be shown in this work, that this is not correct for thin conjugated polymer films. However, if the film thicknesses do not vary too much, this is still a reasonable approximation.

There are two arguments that the MSA provides correct values for the optical anisotropy. First, the results of MSA analysis are in a very good agreement with the results provided by the RT$\Psi\Delta$-method. Secondly, the results of MSA analysis are self-consistent, i. e. there is no scattering of the anisotropy data obtained from many (>20) samples.

Measurement of optical anisotropy of organic materials is a very interesting and challenging topic from the experimental point of view. There are quite a few groups doing ellipsometry to extract film anisotropies. However, each group uses slightly different experiments in order to obtain more reliable results than conventional reflection ellipsometry. Currently there is an effort to compare these techniques by making a simple experiment where a few groups in several universities analyse with their own technique the anisotropy of a thin conjugated polymer film [59]. The idea is to prove whether all of them give similar results and what is the accuracy of measuring anisotropy.

5.2 X-ray diffraction

X-ray diffraction measurements were performed to characterise the structural properties of thin polymer and polymer/fullerene films. In particular, the mean size of the polymer domains and their orientation within the film were studied.

X-ray diffraction patterns were recorded with a Philips *X'Pert-Pro* diffractometer. A monochromatic CuK_α beam with the wavelength $\lambda = 0.154056$ nm was used. The powder diffraction measurements were performed in Bragg-Brentano geometry (see Fig. 5.6a). For these measurements, the powder material was pressed to 2 mm thick tablets. Thin conjugated polymer and conjugated polymer/fullerene films were studied in grazing-incidence diffraction geometry (GID) (Fig. 5.6b) in order to increase the effective XRD beam path in the film and therefore the signal-noise ratio. The angle α between the film surface and the incident beam was fixed at 0.3°. Scans in the plane defined by the incident beam and the surface normal were performed.

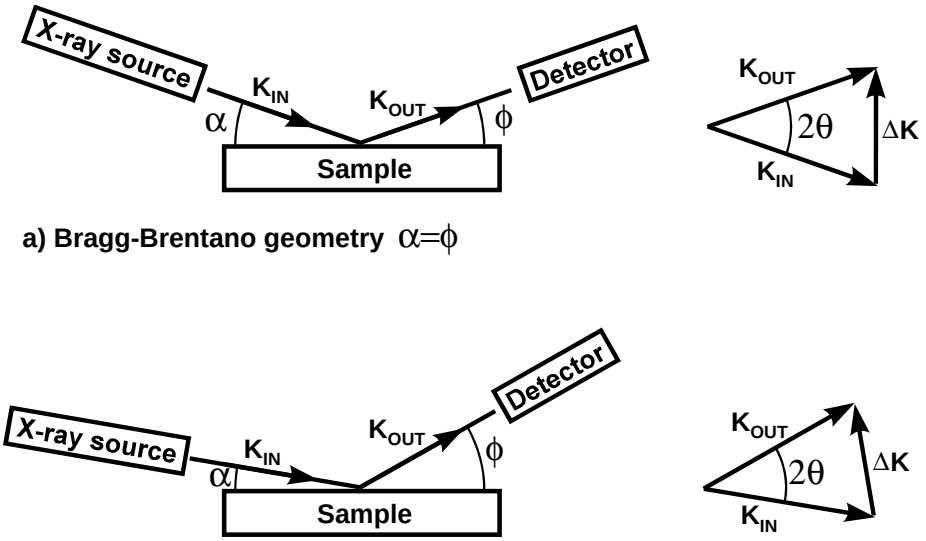

Figure 5.6: XRD measurements in Bragg-Brentano (a) and in grazing incidence diffraction (b) geometries.

The scattering vector $\Delta\mathbf{K}$, which is defined as the difference between the scattered $\mathbf{K}_{OUT}$ and the incident $\mathbf{K}_{IN}$ X-ray vectors, $\Delta\mathbf{K} = \mathbf{K}_{OUT} - \mathbf{K}_{IN}$, is exactly perpendicular to the surface in the Bragg-Brentano geometry. In GID, the scattering vector is slightly deviated from surface normal because of the asymmetry of the GID geometry. However, this deviation is very small [60] and can be neglected in qualitative analysis.

The Bragg condition for the maximum intensity of the scattered beam in a vector form can be written as:

$$\Delta\mathbf{K} = \mathbf{G}, \tag{5.32}$$

where $\mathbf{G}$ is the reciprocal lattice vector. Since the scattering vector $\Delta\mathbf{K}$ is always (nearly) perpendicular to the substrate, only crystallites with the reciprocal lattice vectors perpendicular to the surface are detected in both GID and Bragg-Brentano geometries.

The mean size of the polymer crystallites L can be obtained from Scherrer's formula [61]:

$$L \simeq \frac{0.9\lambda}{\Delta_{2\Theta}\cos\Theta}, \tag{5.33}$$

where $\Delta_{2\Theta}$ is the full width half maximum of the diffraction peak. From the peak intensity and the peak position the crystallinity and the orientation of the polymer crystallites within the film can be extracted, too [61].

5.3 Photoluminescence spectroscopy

Photoluminescence spectroscopy (PL) was used primarily to study the phenomenon of the ultra-fast photoinduced electron transfer in conjugated polymer/fullerene composites. The samples were excited with a 25 mW semiconductor GaN laser, which operates at a wavelength of 408 nm (3.04 eV). In order to prevent the overheating of the sample, the laser beam was usually attenuated by a grey laser filter, which passes 10% of incident light reducing the laser radiation power from 25 mW to 2.5 mW. The sample was placed in cryostat. The cryostat was evacuated before the measurement, thus preventing the photo-oxidation of the sample under influence of air oxygen and laser radiation. The photoluminescence of the sample was then collected by a photo-objective and analysed by a single-grating monochromator with an attached N_2 cooled CCD array.

The PL-setup is controlled by "ScanPL" software [62]. The raw data from the CCD array were corrected using the reference spectrum of the halogen lamp and then normalised to Counts/meV/s).

The PL spectra were taken in a spectral region 1.1 ... 3.0 eV at room temperature.

Chapter 6

Polythiophene films

6.1 Structure of thin polythiophene films

6.1.1 X-ray powder diffraction measurements

The polythiophene crystallite is shown in Fig. 6.1. Literature data on lattice constants a, b and c for P3OT and P3HT [43, 63, 64] are summarised in table 6.1.

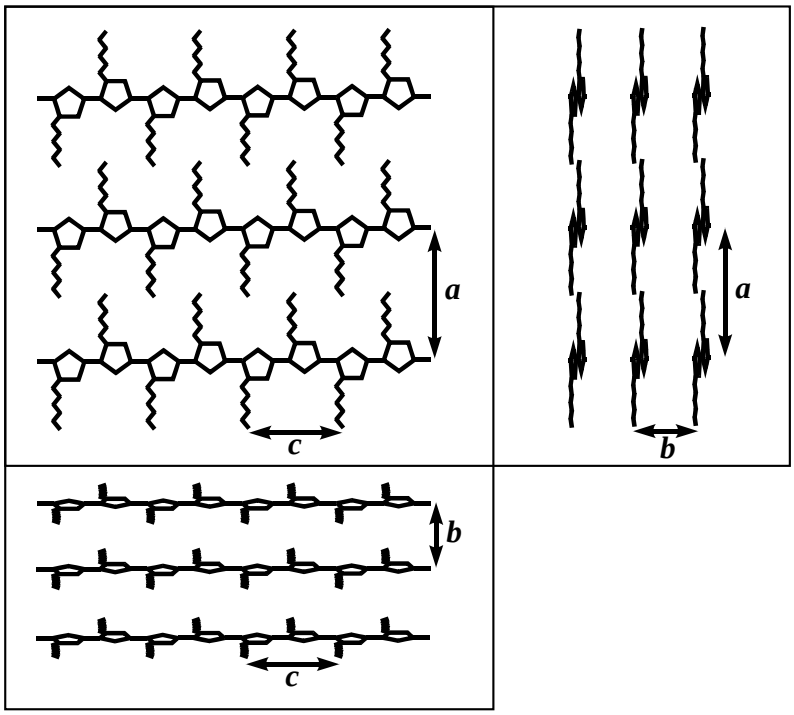

Figure 6.1: P3HT crystal in different projections.

The distance between the polymer chains in a-direction (along the sidechain)

Table 6.1: Lattice constants of P3OT and P3HT crystallites [43, 63, 64].

Conjugated polymer	a (nm)	b (nm)	c (nm)
P3OT	2.06	0.38	0.38
P3HT	1.68	0.38	0.38

is determined by the length of the sidechains. The lattice constant a is larger for P3OT than for P3HT, because the sidechains of P3OT are longer.

The distance between the polymer chains in "stacking" direction (b-direction) is determined by interaction between neighbour thiophene rings. The thiophene rings are identical for P3OT and P3HT. For this reason, the lattice parameter b is the same for these materials.

Finally, the parameter c is simply the length of the repeating unit. Since the chemical structure of the backbone is not changed, the parameter c is not altered, too.

Three principle orientations of polythiophene crystallite with respect to the substrate are shown in Fig. 6.2. In a-axis oriented crystallites (Fig. 6.2a) the polymer backbone is oriented parallel and the alkyl sidechains perpendicular to the substrate, respectively. In b-axis oriented crystallites (Fig. 6.2b) both polymer backbone and sidechains are parallel to the substrate, whereas in c-axis oriented crystallites (Fig. 6.2c) the backbone is perpendicular to the substrate.

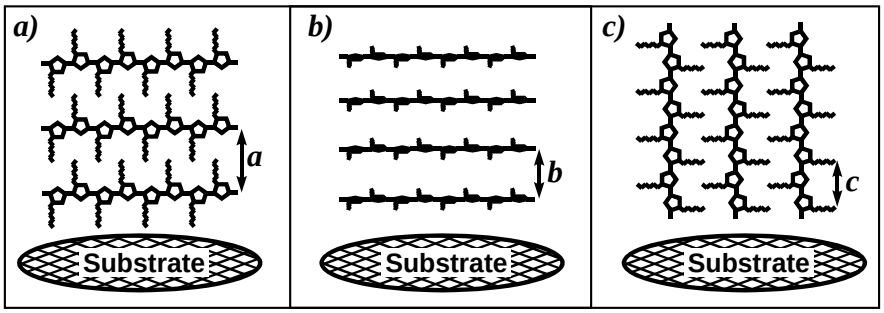

Figure 6.2: a-, b- and c-axis orientations of P3HT crystal with respect to the substrate.

Prior to measuring thin conjugated polymer films the XRD-measurements on bulk materials are needed as a reference. It was pointed above (section 5.2), that only polymer crystallites with reciprocal lattice vector perpendicular to the sample surface can be detected. There is no preferred orientation of the polymer crystallites in bulk material (Fig. 6.3); therefore, the diffraction peaks corresponding to all possible orientations of polymer crystallites should be observed.

On the contrary, the orientation of polymer crystallites within thin spin-coated films should be strongly affected by the substrate.

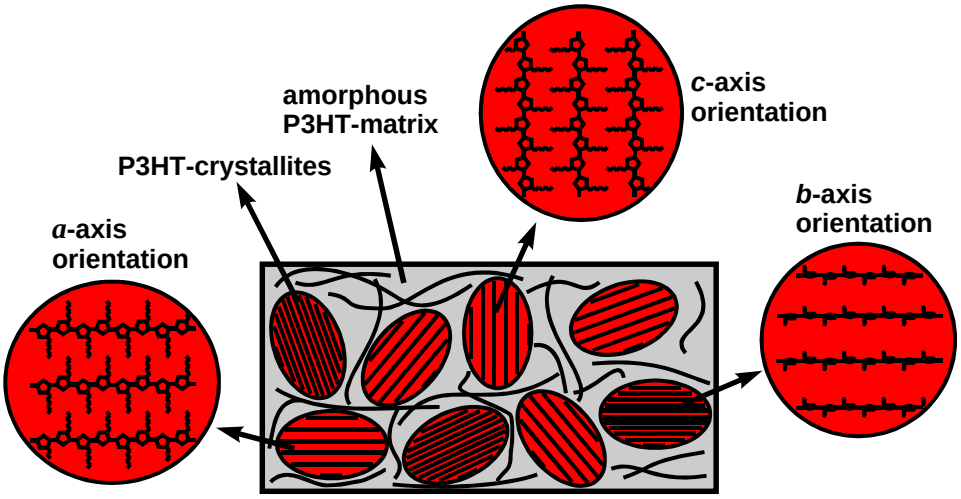

Figure 6.3: Structure of bulk P3HT sample and the orientations of the P3HT-crystallites with respect to the film plane.

In fact, the diffraction peaks corresponding to all three principal orientations of polythiophene crystallite are observed in X-ray measurements on volume P3OT and P3HT. The powder pattern of, for example, P3OT (Fig. 6.4), shows four diffraction peaks at $2\theta = 4.4$, 8.8, 13.2 and 23.6°.

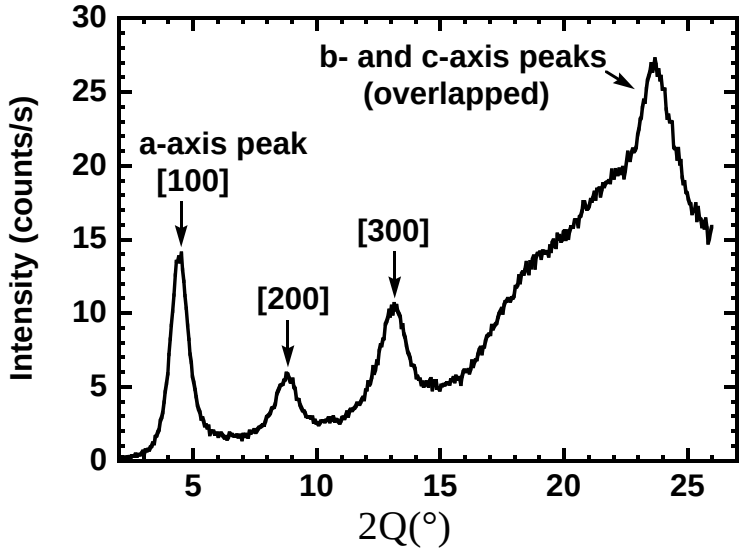

Figure 6.4: Diffractogram of bulk P3OT. The measurement was performed in Bragg-Brentano geometry.

The diffraction peak at 4.4° corresponds to the a-axis orientation of the crystallites. The peak at 8.8° is the second order and the peak at 13.2° the third

order of the 4.4° peak. The broad peak at 23.6° is a superposition of reflections caused by crystallites with *b*- and *c*-axis orientation [44, 63, 64].

6.1.2 XRD on thin polythiophene films

For thin spin-coated P3OT and P3HT films, only the *a*-axis peak appears in the diffractogram (see Fig. 6.5). This means, that only crystallites with *a*-axis perpendicular to the surface (Fig. 6.2a) are available in such films.

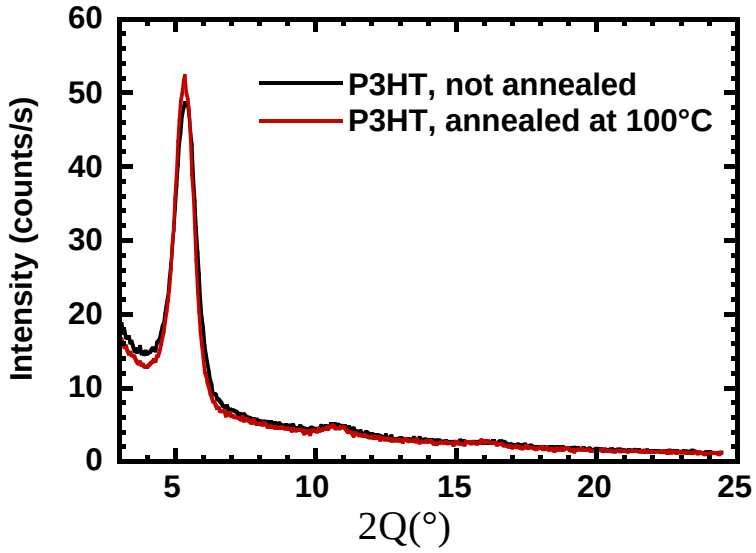

Figure 6.5: Diffractogram of thin spin-coated P3HT film.

The size of the P3HT crystallites can be estimated from Scherrer's equation (5.33) [43, 60, 64, 65]. In our case, the mean crystallite size of ∼10 nm was obtained. From this it can be concluded, that the films under study are partially crystalline. In such films, the P3HT crystallites are dispersed in the amorphous P3HT matrix. The structure of the spin-coated P3HT-films is schematically shown in Fig. 6.6.

The ordering of the P3HT molecules parallel to the film plane could be forced either by polymer-substrate or by polymer-air interfaces. We suppose that the crystallisation of the film after the spin coating begins at the polymer-substrate interface. This can explain differences in optical anisotropy between the films deposited on hydrophobic and hydrophilic substrates (see below).

The crystallinity of polythiophene thin films is only slightly (∼7%) increased upon annealing [66] (see Fig. 6.5). This is probably due to large number of the polythiophene crystallites available in the films already before annealing.

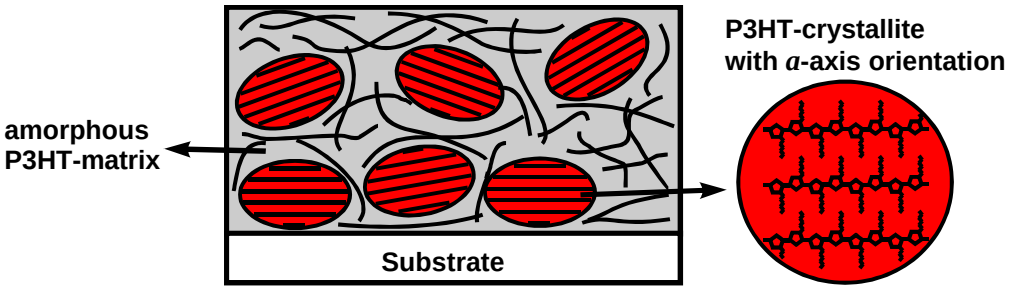

Figure 6.6: Structure of spin-coated P3HT sample. P3HT-crystallites are oriented with a-axis more or less perpendicular to the substrate.

6.2 Optical anisotropy

6.2.1 Anisotropic dielectric function of thin polythiophene films

The anisotropic DF of thin spin-coated P3OT film measured with spectroscopic ellipsometry is shown in Fig. 6.7.

The P3OT film demonstrates a strong optical anisotropy. The ratio of the absorption maxima of ε_2 for the parallel and perpendicular components of DF is nearly 3:1. The real part of the DF ε_1 is highly anisotropic, too.

The strong optical anisotropy is quite typical for thin conjugated polymer films. The DF of other materials like for example PPV/PPE-copolymers have a similar frequency dispersion and comparable optical anisotropy [67].

It has been shown [46, 52], that the imaginary part of the DF ε_2 (which is proportional to the absorption coefficient α, see Eq. (5.8)) indicates the degree of optical anisotropy of the investigated material and therefore characterises the degree of alignment of the polymer chains in the film. This is because the lowest energy optical transition (π-π^*) is excited due to an electric field that is parallel to the conjugated main chain (polymer backbone) [46, 50] and hence the absorption of the polymer is the strongest parallel to the polymer backbone (see Fig. 6.8). The absorption of light polarised perpendicular to the main chain direction occurs in ultraviolet region of the spectrum [68, 69] and is very weak in visible region. Therefore it has been neglected in our study. If now the absorption in the plane of the film becomes stronger, more polymer backbones are aligned parallel to it. The real part of the DF ε_1 will not be discussed in further considerations.

In this study the quotient of the maxima of the parallel and perpendicular components of the imaginary part of DF

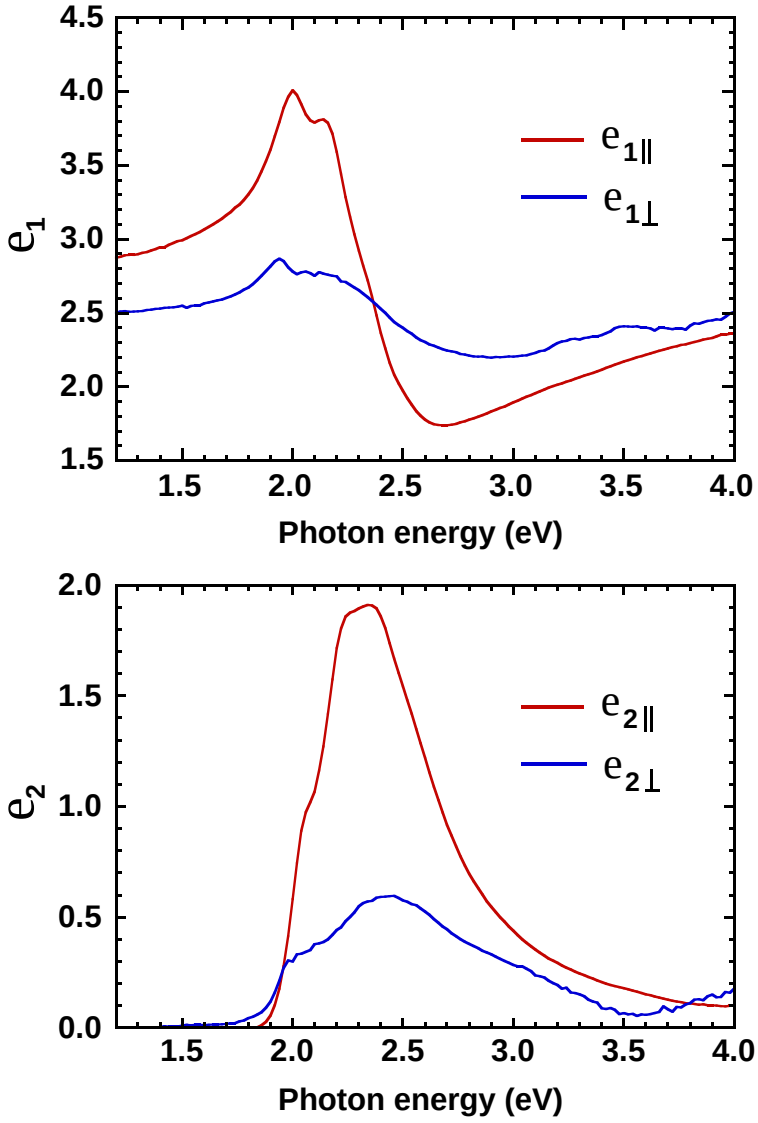

Figure 6.7: Real ε_1 (upper panel) and imaginary ε_2 (lower panel) parts of anisotropic DF of thin (88nm) spin-coated P3OT film.

$$A = \frac{\varepsilon_{2||}^{max}}{\varepsilon_{2\perp}^{max}} \tag{6.1}$$

was used for a qualitative analysis of the optical and structural anisotropy. The parameter A equals infinity if all of the chains are lying parallel to the substrate and it is unity for an isotropic film. We believe that this simple parameter is sufficient to describe the investigated phenomena because the shapes of the parallel and perpendicular components of the DF change only slightly between the films of the same material.

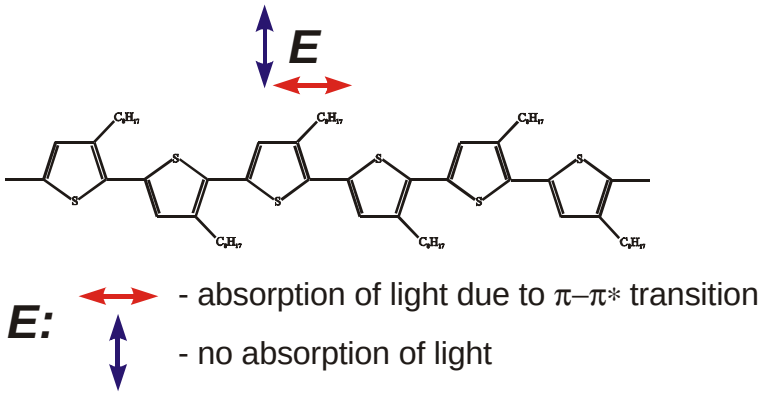

Figure 6.8: Light absorption by isolated polythiophene chain.

6.2.2 Interpretation of the anisotropy parameter A in terms of angular distribution of the polymer chains

In order to relate the anisotropy parameter A to the angular distribution of the polymer segments, a simple model of the polymer film is presented here. It is assumed, that the polymer film consists of molecular segments of equal length, but different orientations with respect to the substrate.

Generally, the imaginary part of the DF ε_2 can be written as [70]:

$$\varepsilon_2 = \frac{\pi e^2}{m_0^2\omega^2}\frac{2}{V}\sum_A\sum_B |\mathbf{e}\cdot\mathbf{p}_{BA}|^2\delta(E_B - E_A - \hbar\omega)(f_A - f_B), \tag{6.2}$$

where f_A (f_B) is the probability that the electronic state A (B) is occupied, $\mathbf{e}$ is a unit vector of electric field and p^i_{BA} is the optical matrix element. In our case, the double sum over all possible initial A and final B electronic states can be replaced by the sum over all polymer chains and the double sum over all π (initial) and π^* (final) states within a single chain. One obtains for ε_2:

$$\varepsilon_2 = C\sum_i\sum_\pi\sum_{\pi^*} |\mathbf{e}\cdot\mathbf{p}^i_{\pi-\pi^*}|^2\delta(E_\pi - E_{\pi^*} - \hbar\omega)(f_\pi - f_{\pi^*}), \tag{6.3}$$

where i is the chain number, $C = \frac{\pi e^2}{m_0^2\omega^2}\frac{2}{V}$. Assuming for simplicity only one initial π and one final π^* state, Eq. (6.3) can be written as:

$$\varepsilon_2 = C\sum_i |\mathbf{e}\cdot\mathbf{p}^i_{\pi-\pi^*}|^2\delta(E_\pi - E_{\pi^*} - \hbar\omega)(f_\pi - f_{\pi^*}), \tag{6.4}$$

or

$$\varepsilon_2 \propto \sum_i |\mathbf{e}\cdot\mathbf{p}^i_{\pi-\pi^*}|^2. \tag{6.5}$$

The orientation of the polymer segment within the film is given by two angles θ and ϕ as shown on Fig. 6.9. The three components of the imaginary part of the DF ε_2 can be written as:

$$\varepsilon_{2X} \propto \mathbf{p}^2_{\pi-\pi^*} \sum_i \sin^2\theta_i \cos^2\phi_i, \tag{6.6}$$

$$\varepsilon_{2Y} \propto \mathbf{p}^2_{\pi-\pi^*} \sum_i \sin^2\theta_i \sin^2\phi_i, \tag{6.7}$$

$$\varepsilon_{2Z} \propto \mathbf{p}^2_{\pi-\pi^*} \sum_i \cos^2\theta_i. \tag{6.8}$$

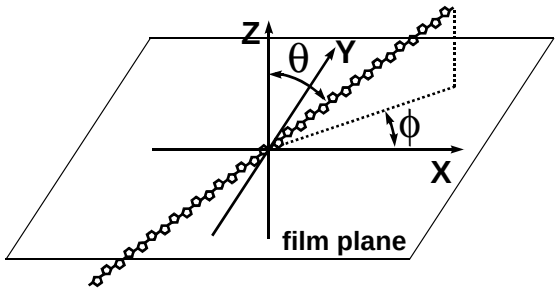

Figure 6.9: Orientation of the polymer chain within the film.

Using known angular distribution of the polymer segments $\Phi(\theta, \phi)$, one obtains:

$$\varepsilon_{2X} \propto \int_{\theta=0}^{\pi} \int_{\phi=0}^{2\pi} \Phi(\theta,\phi) \sin^2\theta \cos^2\phi d\theta d\phi, \tag{6.9}$$

$$\varepsilon_{2Y} \propto \int_{\theta=0}^{\pi} \int_{\phi=0}^{2\pi} \Phi(\theta,\phi) \sin^2\theta \sin^2\phi d\theta d\phi, \tag{6.10}$$

$$\varepsilon_{2Z} \propto \int_{\theta=0}^{\pi} \int_{\phi=0}^{2\pi} \Phi(\theta,\phi) \cos^2\theta d\theta d\phi. \tag{6.11}$$

Since the properties of the investigated polymer films were symmetric in respect to the rotation axis perpendicular to the surface, the distribution function Φ should be only function of polar angle θ, $\Phi = \Phi(\theta)$. After the integrating of (6.9) over ϕ one obtains:

$$\varepsilon_{2X} = \varepsilon_{2Y} \propto \pi \int_{\theta=0}^{\pi} \Phi(\theta) \sin^2\theta d\theta, \tag{6.12}$$

$$\varepsilon_{2Z} \propto 2\pi \int_{\theta=0}^{\pi} \Phi(\theta) \cos^2\theta d\theta. \tag{6.13}$$

For case of isotropic sample the angular distribution function $\Phi(\theta)$ has the following form:

$$\Phi^{isotropic}(\theta) = \sin\theta. \tag{6.14}$$

Applying $\Phi^{isotropic}(\theta)$ to (6.12), one obtains $\varepsilon_{2X} = \varepsilon_{2Y} = \varepsilon_{2Z}$, i. e. the DF of isotropic material. In order to introduce the optical anisotropy, the distribution function $\Phi(\theta)$ should be modified. The optical anisotropy follows for example from the assumption, that the tilt angle of all the polymer chains does not exceed a maximum tilt angle θ_{MAX}. This assumption is in agreement with X-ray studies on polythiophene films (see section 6.1.2). These measurements show, that the polymer crystallites are oriented preferably with polymer backbone parallel to the substrate, and there are no crystallites with c-axis orientation (polymer backbone perpendicular to the substrate). For this reason, the following distribution function for anisotropic conjugated polymer films was taken:

$$\Phi(\theta) = \begin{cases} \sin\theta & 90° - \theta_{MAX} < \theta < 90° + \theta_{MAX} \\ 0 & \text{otherwise} \end{cases} . \tag{6.15}$$

This function $\Phi(\theta)$ is shown in Fig. 6.10 for $\theta_{MAX} = 50°$.

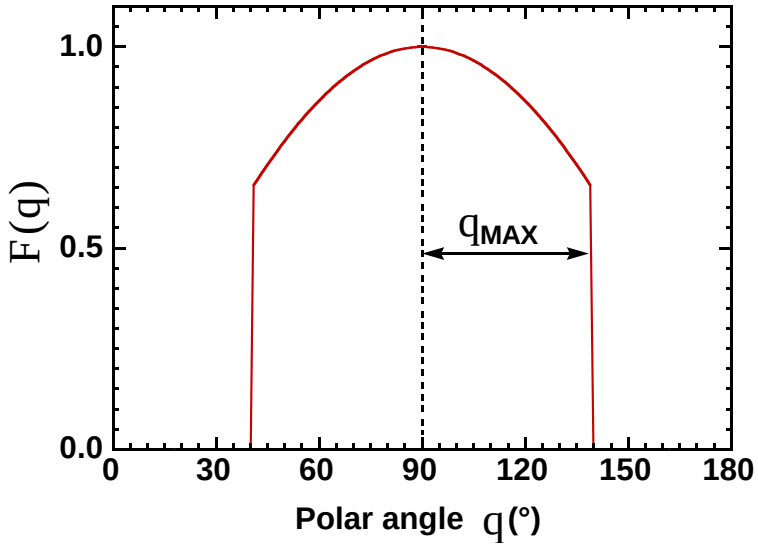

Figure 6.10: Anisotropic angular distribution of polymer chains $\Phi(\theta)$.

Now, the anisotropy parameter A can be calculated from (6.12) using the distribution function $\Phi(\theta)$ from (6.15) and taking into account that $\varepsilon_{2X} = \varepsilon_{2Y} =$

$\varepsilon_{2||}$ and $\varepsilon_{2X} = \varepsilon_{2\perp}$:

$$A = \frac{\varepsilon_{2||}}{\varepsilon_{2\perp}} = \frac{1}{2}\frac{\int_{\pi/2-\theta_{MAX}}^{\pi/2+\theta_{MAX}} \sin^3\theta d\theta}{\int_{\pi/2-\theta_{MAX}}^{\pi/2+\theta_{MAX}} \sin\theta\cos^2\theta d\theta} = \frac{3\sin\theta_{MAX} - \sin^3\theta_{MAX}}{2\sin^3\theta_{MAX}}. \quad (6.16)$$

The anisotropy parameter A in dependence on the maximum tilt angle θ_{MAX} is shown in Fig. 6.11. The anisotropy parameter A changes from unity for $\theta_{MAX} = 90°$ (isotropic film) to very high values for small θ_{MAX} (highly anisotropic film). For typical values of the anisotropy parameter A of $2.5 - 4.0$ (see below, section 6.2.3), the maximum tilt angle θ_{MAX} is in a range of $34° - 44°$.

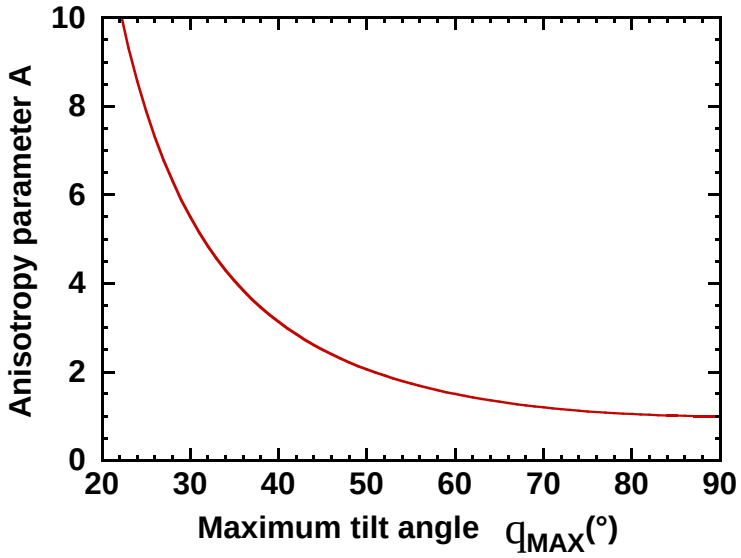

Figure 6.11: Calculated anisotropy parameter A in dependence on the maximum tilt angle of the polymer chains θ_{MAX}.

Thus, the Eq. (6.16) gives us the possibility to relate the measured anisotropy parameter A to the orientation of the polymer segments via maximum tilt angle θ_{MAX}.

6.2.3 Anisotropy of thin polythiophene films in dependence on preparation parameters

In order to investigate the influence of the preparation conditions on the optical properties of the spin-coated films, we have studied the P3OT-films at Si and

Table 6.2: P3OT samples for systematical study of the optical anisotropy.

Sample #	Preparation method	Polymer concentration (wt.%) / Solvent	Substrate/ treatment	Spin frequencies (rpm)
1	Spin coating	1.1 / CB	Si / -	750, 1000, 1500, 2000, 3000, 4000
2	Spin coating	0.7 / CB	Si / -	1500
3	Spin coating	1.5 / CB	Si / -	1500
4	Spin coating	2.0 / CB	Si / -	1500
5	Spin coating	1.1 / Tol	Si / -	1500
6	Spin coating	1.5 / CB	Glass / -	2000, 3000, 4000
7	Spin coating	1.1 / CB	Si / -	650
8	Spin coating	1.1 / CB	Si / HF[1]	650
9	Drop casting	0.7 / CB	Si / -	-
10	Drop casting	1.5 / CB	Si / -	-
11	Drop casting	1.1 / Tol	Si / -	-
12	Drop casting	0.7 / CB	Glass / -	-
13	Drop casting	1.5 / CB	Glass / -	-

glass substrates, prepared by different spin frequencies and polymer concentrations in the solution. The solvents used were chlorobenzene and toluene. The spin frequency was varied from 500 to 6000 rounds per minute (rpm), and the polymer concentration from 0.7% to 2.0%.

The imaginary ε_2 part of DF of the films on Si substrates prepared by different spin frequencies (750-4000 rpm, serie #1, see Table 6.2) and fixed polymer concentration (1.1%) is shown in Fig. 6.12. With increased spin frequency, the parallel component of the DF increases and the perpendicular one decreases; the anisotropy parameter A grows from 2.85 (spin frequency 750 rpm) to 4.08 (spin frequency 4000 rpm). This means that on average the films become more aligned with increased spin frequency.

The same behaviour can be observed for films prepared by fixed spin frequency (1500 rpm) but various polymer concentrations (0.7%, 1,1%, 1,5%, 2.0%, samples #2-4; see Fig. 6.13). The anisotropy parameter A grows from 2.37 (polymer concentration 2.0%) to 4.05 (polymer concentration 0.7%).

To investigate the influence of the substrate on the optical properties of the spin-coated films, the P3OT films were spin-coated onto both glass and Si substrates (samples #6 and #7, respectively). In addition, some Si-substrates were

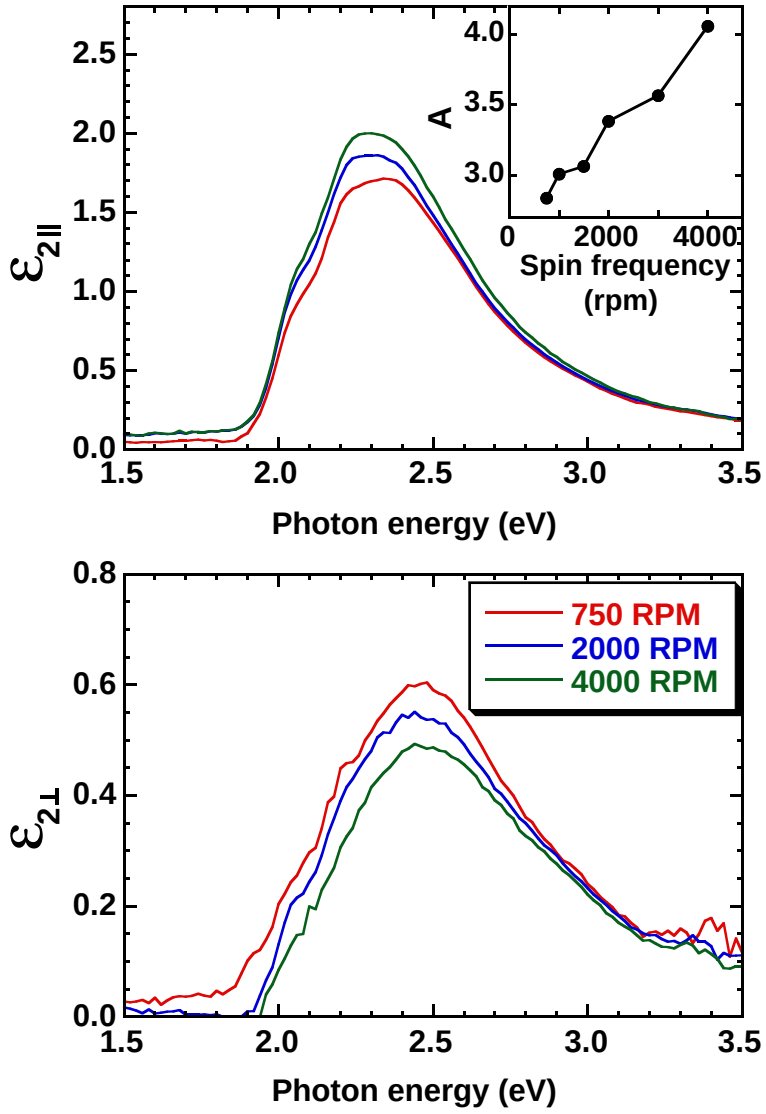

Figure 6.12: Imaginary ε_2 part of the parallel (upper panel) and perpendicular (lower panel) components of the anisotropic DF of spin-coated P3OT films prepared by different spin frequencies and fixed polymer concentration of 1.1% in chlorobenzene.

treated with HF-acid prior to spin-coating of the polymer films (#8). It is known, that such a treatment changes the surface properties of the Si to be hydrophobic, whereas the untreated Si is hydrophilic. The anisotropy A of the film deposited on hydrophilic Si is comparable to the spin-coated films on glass. However, the films deposited on hydrophobic substrates are much more anisotropic than these deposited on hydrophilic ones (the anisotropy parameter A changes from 2.30 to 2.97 [71]). The origin of this phenomenon is discussed below.

For comparison, we have plotted the anisotropy parameter A for all spin-

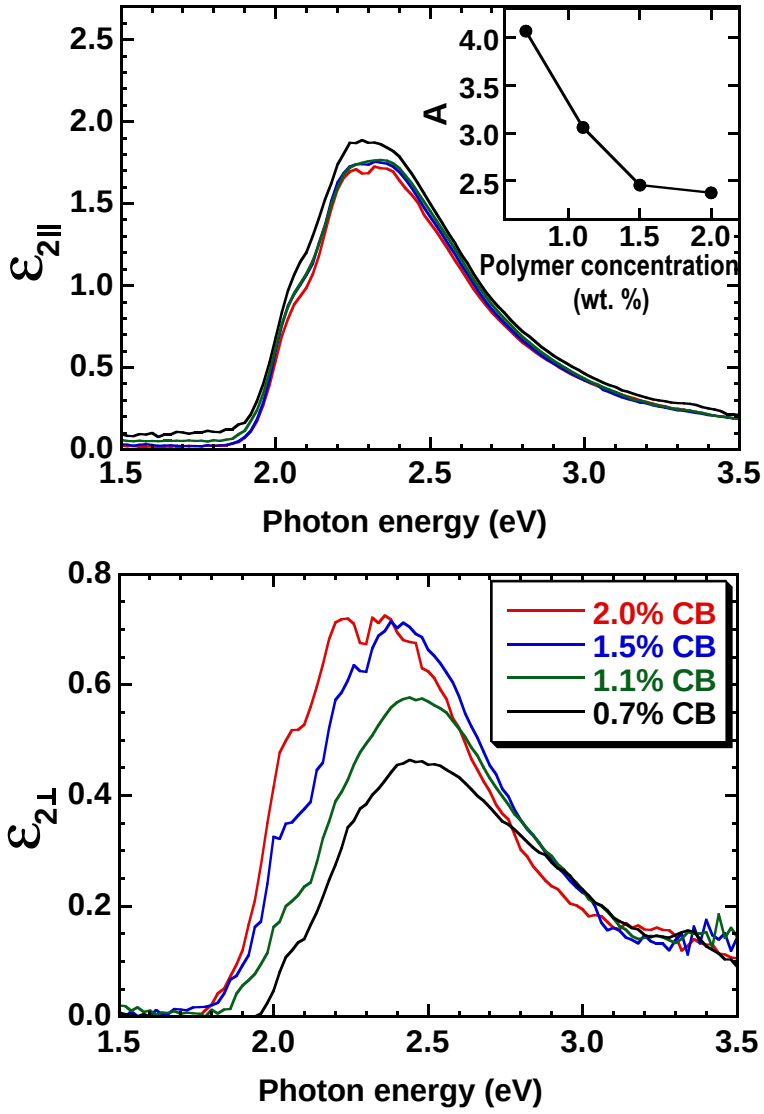

Figure 6.13: Imaginary ε_2 part of the parallel (upper panel) and perpendicular (lower panel) components of the anisotropic DF of spin-coated P3OT films prepared from chlorobenzene solutions of different polymer concentrations and fixed spin frequency 1500rpm.

coated samples in dependence on the film thickness, which was also obtained from spectroscopic ellipsometry (see Fig. 6.14). The anisotropy of the spin-coated films increases with decreased film thickness, and depends not strongly on the spin frequency and polymer concentration. At a given film thickness, the variation of spin frequency and polymer concentration induces a change in anisotropy of maximum 15% (see Fig. 6.14). There is also no strong dependence on the solvent type. There are no significant differences between samples deposited on Si and glass substrates with exception of the film deposited on HF-

treated (hydrophobic) Si substrates, as it was mentioned above. It can be concluded, that the film thickness is the decisive parameter for the optical anisotropy of spin-coated films, as all the data points fall unto some kind of "master curve".

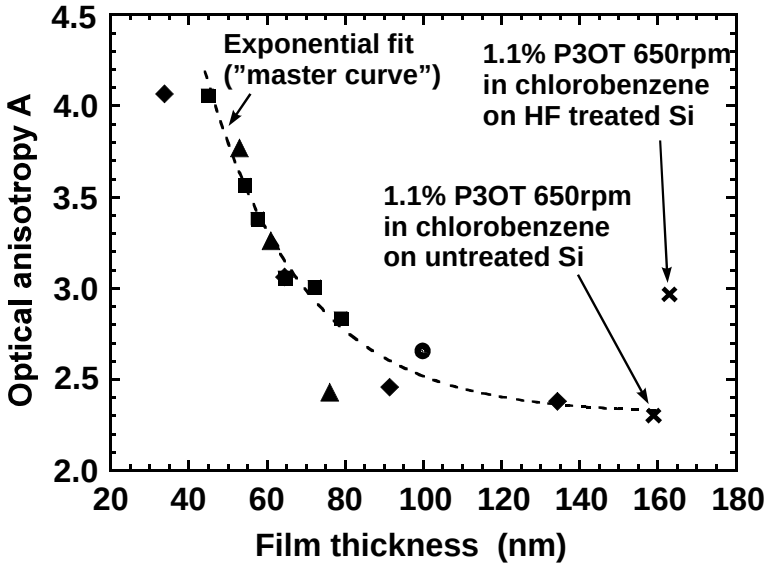

Figure 6.14: Anisotropy parameter A of spin-coated P3OT-films prepared by: various spin frequencies (750, 1000, 1500, 2000, 3000, 4000 rpm) on untreated Si substrates from 1.1% chlorobenzene solution (squares); various polymer concentrations (0.7, 1.1, 1.5, 2.0%) on untreated Si substrates from chlorobenzene solution by 1500 rpm (diamonds); various spin frequencies (2000, 3000, 4000 rpm) on glass substrates from 1.5% chlorobenzene solution (triangles); 1500 rpm on Si substrate from 1.1% toluene solution (circle). The experimental points fall closely on a single "master curve", an exponential decay.

In addition, we have measured drop-cast films deposited on untreated Si and glass substrates (samples #9-13). The results are shown in Fig. 6.15. A decrease of the anisotropy with a film thickness is also observed. On the same figure, the "master curve" for spin coated films taken from Fig. 6.14 is also shown for comparison. All measured drop-cast films are more anisotropic than spin-coated ones of comparable film thickness.

We conclude, that the optical anisotropy in pristine conjugated polymer films depend mainly on:

- Preparation method: drop-cast films are more oriented than spin-coated ones;
- Film thickness: with increased film thickness the films become less oriented,

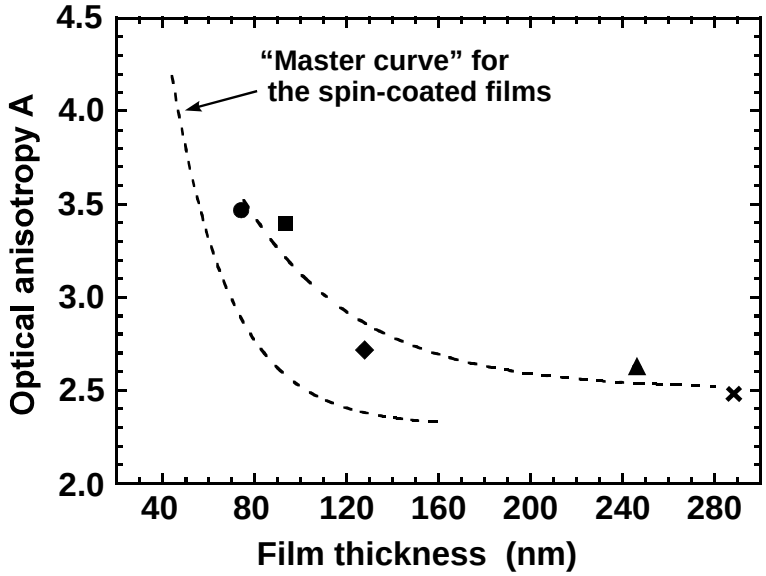

Figure 6.15: Anisotropy parameter A of drop-cast P3OT-films prepared from: 0.7% chlorobenzene solution on glas (circle); 0.7% chlorobenzene solution on untreated Si (square); 1.1% toluene solution on untreated Si (diamond); 1.5% chlorobenzene solution on glas (triangle); 1.5% chlorobenzene solution on untreated Si (cross).

and

- Substrate properties: the degree of orientation is higher for films deposited on hydrophobic substrates.

Our results can be understood by the assumption [71, 43], that the film begins to solidify at the substrate and that the polymers form to some extend little crystallites by parallel alignment of the polymer main chains [43, 44] (see Fig. 6.16a) . For the first layers of the polymer film the interaction between the polymer and the substrate is significant. Depending on the interaction the alignment of the main chain will be more or less parallel to the substrate. This can explain the observed differences in the anisotropy between the films deposited on the HF-treated silicon and the non-treated silicon substrates (Fig. 6.16b). The interaction of the polymer chain with the hydrophobic surface is enhanced as compared to the hydrophilic one.

Further on, the deposition time (i.e. the time of evaporation of the solvent) is the other important parameter that determines the properties of the films. For drop-cast films, the deposition time is significantly larger ($\sim$30 s and more), and the polymer molecules have more time to settle and align. Therefore the obtained order of the polymer within these films is better than in the spin-coated

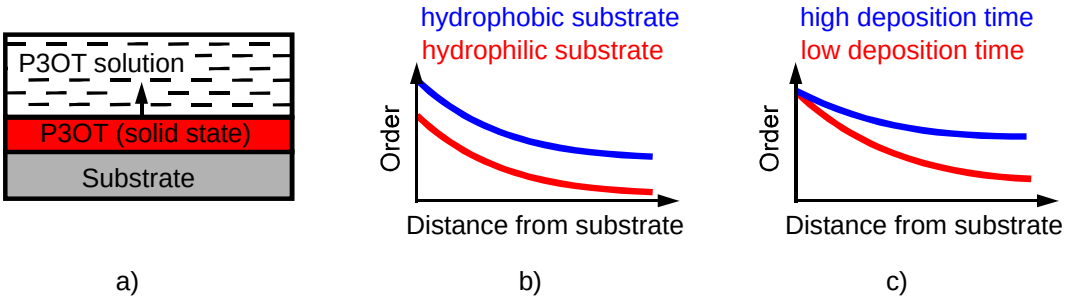

Figure 6.16: Formation of polythiophene film.

ones (Fig. 6.16c). For the spin-coated films, the deposition time is (with just a few seconds) lower. In summary the deposition time and the interaction strength between substrate and polymer determine the order and the optical anisotropy within the polymer films.

The differences in the deposition time and the interaction on the glass and silicon substrates seem not to differ very much for the spin cast films. This can be an explanation for that the relation between the anisotropy and the film thickness falls on one curve for the different preparation conditions used to produce these films. The shape of the curve suggests an exponential drop off of the anisotropy with film thickness (see fit on Fig. 6.14, 6.15). The characteristic length for the decay is on the order of a few tens of nanometers. Within the first layers of the film the ordering of the polymer molecules is driven by the short-range interaction between substrate and polymer. After this initially strongly ordered layer the order of the polymer drops off exponentially with a characteristic length, which can be understood as a correlation length for the main chain direction, similar to the behavior of nematic liquid crystals in the isotropic phase* [72].

*We have tried to apply a more complicated optical model including an anisotropy gradient within the conjugated polymer film. However, the multiple sample analysis failed in this case because of very large number of fit parameters and strong parameter correlation.

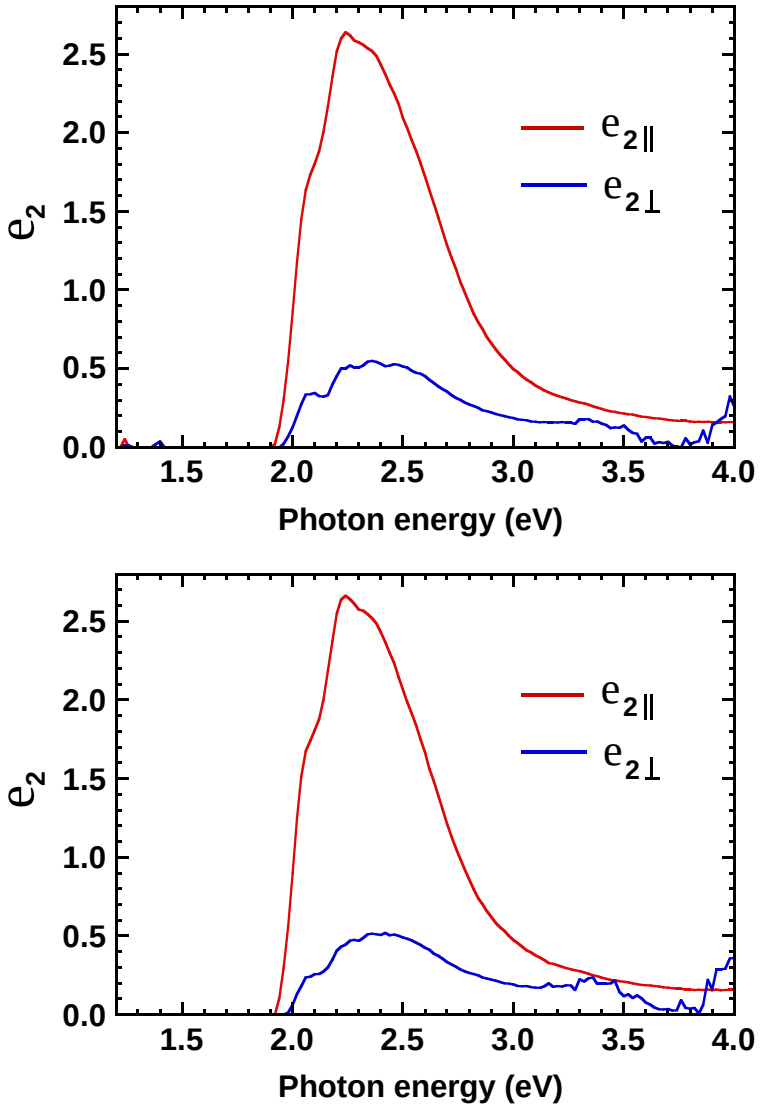

Figure 6.17: Imaginary part of the anisotropic DF of untreated (upper panel) and annealed at 85° (lower panel) pristine P3HT films.

6.2.4 Influence of annealing on the optical anisotropy

The anisotropic DF of untreated and annealed at 85°C for 10 min pristine P3HT films is shown in Fig. 6.17. The films were prepared by spin coating on untreated Si substrates from 0.3 wt.% chloroform solution.

Although the differences between untreated and annealed films are not very strong, the parallel component of the DF of annealed film is larger than that of untreated one ($\varepsilon_{2||}^{max} = 2.66$ for annealed and $\varepsilon_{2||}^{max} = 2.63$ for untreated film). At the same time, the perpendicular component of the DF of annealed film is smaller than that of untreated film ($\varepsilon_{2\perp}^{max} = 0.51$ for annealed and $\varepsilon_{2\perp}^{max} = 0.55$

for untreated film). The shapes of the parallel and perpendicular components of the DF does not significantly change between the untreated and the annealed films. The anisotropy parameter A increases by 9% from $A = 4.78$ for untreated film to $A = 5.22$ for annealed one. Thus, polythiophene crystallites become more aligned parallel to the substrate upon annealing. This is in a good agreement with the observed increase of the film crystallinity upon annealing (see Fig. 6.5).

6.3 Anisotropic mobility in polythiophene films

The mobility of charge carriers in polythiophene films depends strongly on both transport direction (parallel/perpendicular to the main chain) and on the films structure (crystalline/amorphous). In experiments on field-effect transistors prepared by drawing method, the highest mobility $\mu = 7.4 * 10^{-4}$ cm^2/(Vs) was observed in the main chain (c-axis) direction [18]. The mobility perpendicular to the main chain direction was with $\mu = 0.9 * 10^{-4}$ cm^2/(Vs) one order of magnitude lower. This is because the mobility perpendicular to the chain direction (a- or b-direction) is limited by hopping from one polythiophene chain to another, whereas the band transport along the main chain is much more effective. The mobility along the a-axis μ_a is obviously lower than this along the b-axis μ_b because of higher distance between the neigbour polythiophene molecules in the a-axis direction (a=1.68 nm for P3HT) compared to this in the b-axis direction (b=0.38 nm).

From our structural and optical studies it follows, that for thin spin coated and drop cast polythiophene films the polythiophene crystallites are oriented with a-axis perpendicular to the substrate. At the same time, there is no preferred orientation of the c- (or b-) axis. Thus, the charge transport perpendicular to the substrate occurs due to hopping along a-axis with charge mobility μ_a. On the contrary, the in-plane mobility is determined by band transport along the c-axis and by hopping along the b-axis with characteristic mobilities μ_c and μ_b, respectively. Since both μ_c and μ_b are much higher than μ_a, the in-plane mobility should be much higher than out-of-plane one.

In fact, the measured out-of-plane mobilities are several orders of magnitude lower than the in-plane ones. This can be clearly seen from a comparison between field-effect transistor (FET) and space charge limited current (SCLC) or time-of-flight (ToF) mobilities. In FET-configuration, the in-plane mobility is measured, whereas SCLC and ToF mobilities are those out-of-plane. In most cases the best

in-plane (FET) mobilities ($\mu_{FET} \sim 10^{-2} - 10^{-1}$ cm^2/(Vs)) [25, 20, 21, 22, 16] exceed the out-of-plane (SCLC, ToF) ones ($\mu_{SCLC,ToF} \sim 10^{-10} - 10^{-4}$ cm^2/(Vs)) [73, 74, 75, 19, 76] by several orders of magnitude.

Let us discuss the influence of the film structure and the optical anisotropy on in-plane and out-of-plane mobilities separately.

6.3.1 In-plane mobility

It is commonly assumed, that the in-plane mobility in polythiophene films is limited by disordered regions [77]. One possibility to reduce a disorder is to align the polymer molecules (and crystallites) parallel to the substrate. From this point of view, a comparison between the films deposited on hydrophilic or hydrophobic substrates is of interest. We have found in section 6.2.3, that the films deposited on hydrophilic substrates are more anisotropic than this deposited on hydrophobic ones. Consequently, the molecule ordering is better for the films on hydrophobic substrates. One can expect, that the in-plane mobility is increased, too.

A strong dependence of FET mobilities on the water contact angle was observed in [78, 79]. The mobility is increased with increasing water contact angle Θ from $1.4 * 10^{-3}$ cm^2/(V s) for $\Theta = 62°$ to $3.5 * 10^{-2}$ cm^2/(V s) for $\Theta = 110°$. Thus, the mobility is higher for films deposited on hydrophobic substrates, which is in a good agreement with the observed increase of optical anisotropy. We conclude, that there is a distinct correlation between the optical anisotropy and the in-plane mobility.

Further on, a moderate increase of the in-plane mobility was observed upon annealing of polythiophene films. Despite of the increase of the film crystallinity (section 6.5) and anisotropy (section 6.17) after annealing, the in-plane mobility increases only slightly. For the films deposited on Si substrate treated with self-assembled octadecyltrichlorosilan (OTS) monolayer, the in-plane mobility was increased from $3.5 * 10^{-2}$ to $4.2 * 10^{-2}$ cm^2/(V s) [79]. This seems to be in a contradiction with the observed huge increase of the in-plane mobility with increased water contact angle.

To understand this difference, one should take into account, that the charge transport in field-effect transistors takes place only in the thin (several nm) accumulation region on the polymer-isolator interface. For this reason, FET performance and FET mobility depend mainly on the structure of the interface layer.

We suppose, that the structure of the interface layer is forced by the substrate, whereas the annealing supports the formation of the polythiophene crystallites in the bulk material. Therefore the in-plane mobility is not significantly increased after annealing.

6.3.2 Out-of-plane mobility

The out-of-plane mobility can be measured in sandwiched devices like for example metal-isolator-semiconductor (MIS) diodes or metal-semiconductor-metal structures (for SCLC or ToF measurements). In [79, 80], the out-of-plane mobility was determined from the capacitance-frequency and capacitance-voltage measurements on polythiophene-based MIS diodes. Typical out-of-plane mobilities of 10^{-8}-10^{-7} $cm^2/(V\ s)$ for not annealed polythiophene films were reported. The mobility is increased to 10^{-6}-10^{-5} $cm^2/(V\ s)$ upon annealing. We attribute this increase to the increased crystallinity of the annealed polythiophene films. This leads to enhanced overlap of the wavefunctions of neigbour polythiophene molecules and therefore to the increased out-of-plane mobility.

Chapter 7

Polythiophene/fullerene films

7.1 Structure of polythiophene/fullerene films

7.1.1 Polythiophene phase

In composite polythiophene/fullerene films, the polythiophene crystallites are generally *a*-axis oriented, too [64, 66]. However, the crystallinity of the composite films is significantly lower than that of pristine polymer films.

On the contrary to pristine polythiophene films, the crystallinity of the composite polythiophene/fullerene films is drastically increased upon annealing [66, 81]. Fig. 7.1 shows the diffractograms of untreated (black) and annealed at 150°C for 2 min. (red) P3HT/PCBM films with 66 wt.% of PCBM. The films were prepared by spin coating on untreated Si substrates from 1.2 wt.% chlorobenzene solution. The untreated sample exhibits neither polymer crystallites with *a*- nor with *b*- or *c*-axis orientations (the corresponding peaks fail in the spectrum, cp. Figs. 6.4 and 6.5). This is probably because the PCBM-molecules, placed between the P3HT-chains, disturb the formation of the P3HT-crystallites.

The peak at 2θ=5.4° in the spectrum of the annealed sample indicates, however, that the annealed sample contains significant number of polymer crystallites with *a*-axis orientation. This observation is in a good agreement with the results of Yang et. al. [8], who have observed the increased diffusion of PCBM-molecules at high temperatures, resulting in an accelerated phase segregation and in the formation of large PCBM clusters in the films. Since the PCBM cluster become larger upon annealing, the concentration of PCBM-molecules between the P3HT-chains becomes lower, resulting in the improved formation of P3HT-crystallites.

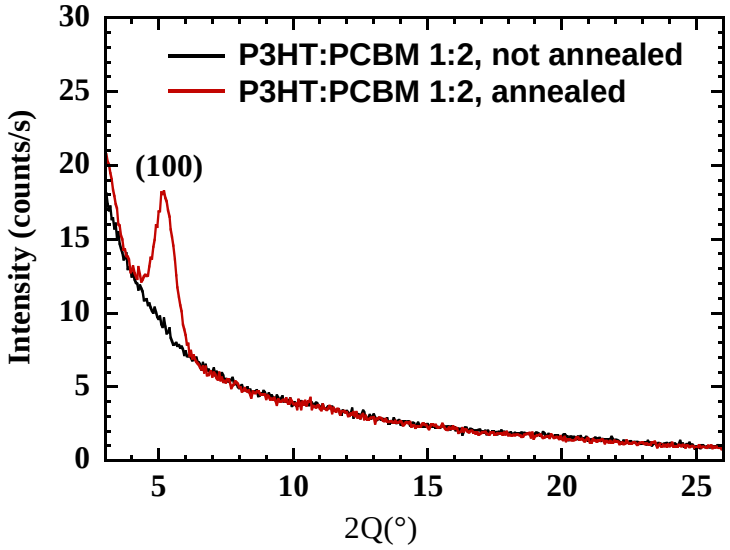

Figure 7.1: Diffractogram of thin untreated and annealed at 150°C P3HT/PCBM composite films.

Photoluminescence (PL) measurements on the same samples (Fig. 7.2) provide another evidence of the formation of polymer crystallites. The photoluminescence of annealed sample is several times higher than that of the not annealed one. That means that photoinduced electron transfer becomes less effective upon annealing. The efficiency of electron transfer depends obviously from the mean distance between conjugated polymer and fullerene molecules. If the distance between polymer and fullerene becomes comparable with exciton diffusion length ($\sim 10-20$ nm [82]), some excitons can not reach the neighbour fullerene molecules and recombine radiatively, giving rise to the PL signal (see also section 2.2). Since the concentration of the PCBM in the film does not change upon annealing, we conclude, that the change of the PL intensity originates from changes in morphology of the active layer. We assume, that the fullerene molecules tends to leave the polymer crystallites upon annealing. This results in the increased PL intensity, because the average distance between polymer and neighbour fullerene is increased.

The efficiency of electron transfer η_{PET} can be calculated from Eq. (2.9). For the not annealed P3HT/PCBM composite, PL quenching $Q(\hbar\omega)$ is 94 at $\hbar\omega$=1.71 eV and the calculated from Eqs. (2.8,A.6) correction factor K equals 0.75. Using (2.9) one obtains for the not annealed sample η_{PET}=98.5%. In the case of the not annealed sample, the photoluminescence quenching is significantly lower ($Q(\hbar\omega)$=16 at $\hbar\omega$=1.71 eV), resulting in lower efficiency of electron trans-

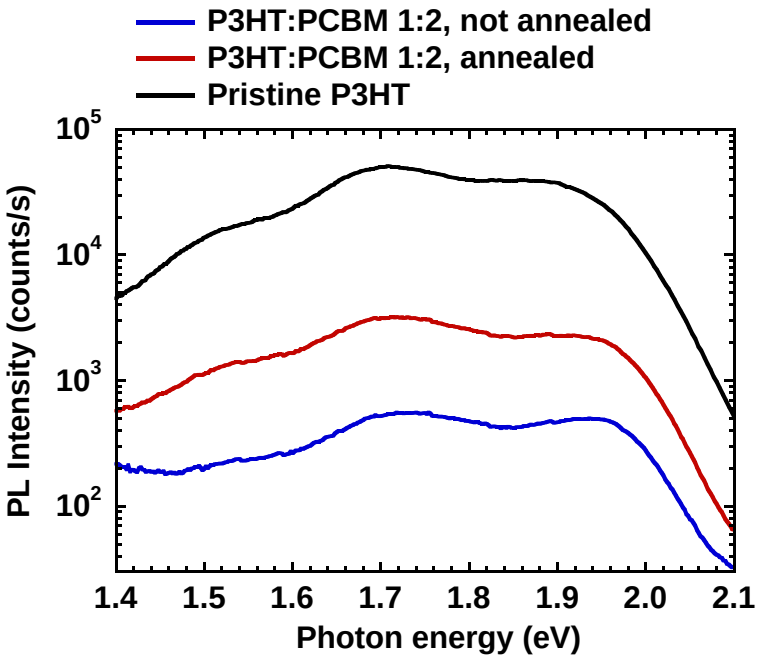

Figure 7.2: PL spectra of thin untreated and annealed at 150°C P3HT/PCBM composite films. PL of pristine P3HT is also shown for comparison.

fer η_{PET}=93% (correction factor K=0.90 was used). Although the efficiency of electron transfer η_{PET} becomes lower due to annealing of P3HT/PCBM composite, it is still high enough for operation of plastic solar cell, because only 7% of photogenerated charge carriers recombine radiatively and thus can not contribute to the photocurrent produced by plastic solar cell.

7.1.2 PCBM phase

Figures 7.3a,b display representative tapping mode AFM results obtained on the untreated and the annealed P3HT/PCBM films. A moderate surface roughness (2.5 nm peak-to-peak value) is observed already for the not annealed sample. This is caused by fullerene clusters [3, 10]. In the case of the annealed sample (Fig. 7.3b), the surface is getting somewhat rougher (3.6 nm). This can be understood in terms of an ongoing phase separation inside the composite. The diffusion of the fullerene leads to growth of fullerene clusters.

It should be pointed out, that in our measurements diffraction peaks caused by PCBM crystallites were not detected. This is in contradiction to [8] who observed the formation of PCBM single crystals in MDMO-PPV/PCBM films by transmission electron microscopy (TEM). The size of the PCBM crystals is

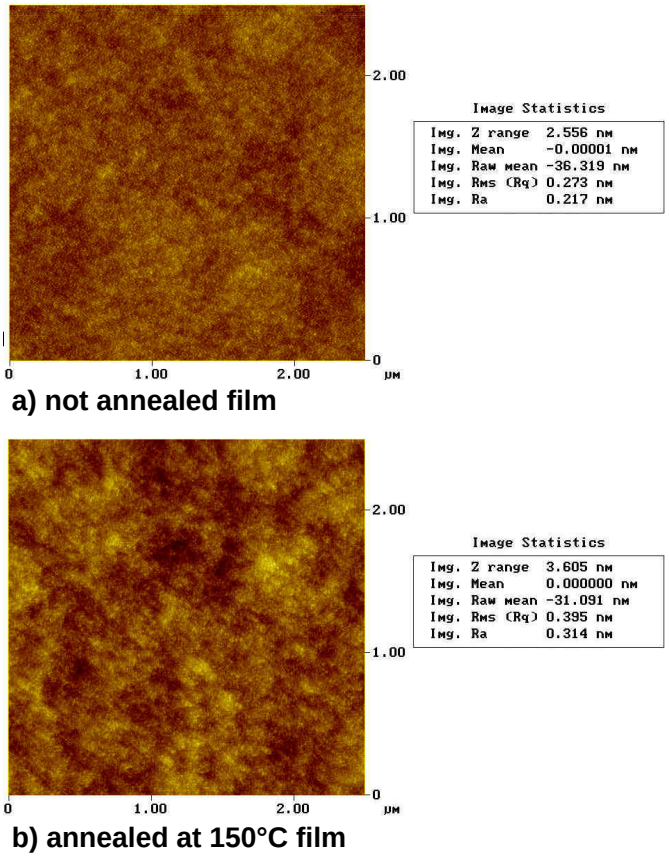

Figure 7.3: Tapping mode AFM topography images of the not annealed (a) and the annealed at 150°C (b) P3HT/PCBM films. The annealing causes some roughening of the film due to stronger phase separation inside the mixture. The z-scales are 2.5 nm in (a) and 3.6 nm in (b). (From H. Hoppe (LIOS Linz)).

increased upon annealing. The same group has found single PCBM crystals in thin pure PCBM films with TEM measurements [83].

To investigate this difference, we studied pure PCBM powder by XRD first. A distinct diffraction pattern with characteristic narrow peaks was measured (Fig. 7.4). These peaks, however, are absent in the diffractogram of both not annealed and annealed P3HT/PCBM thin films. Consequently, the PCBM is not crystalline in our P3HT/PCBM films within the limit of our sensitivity.

We suppose that the reason lies in the special molecular structure of the P3HT molecule in combination with the aggregation of P3HT in crystalline nanodomains. One possible explanation is that the side chains of P3HT and the nanodomains disturb the formation of PCBM crystallites in our thin P3HT/PCBM films.

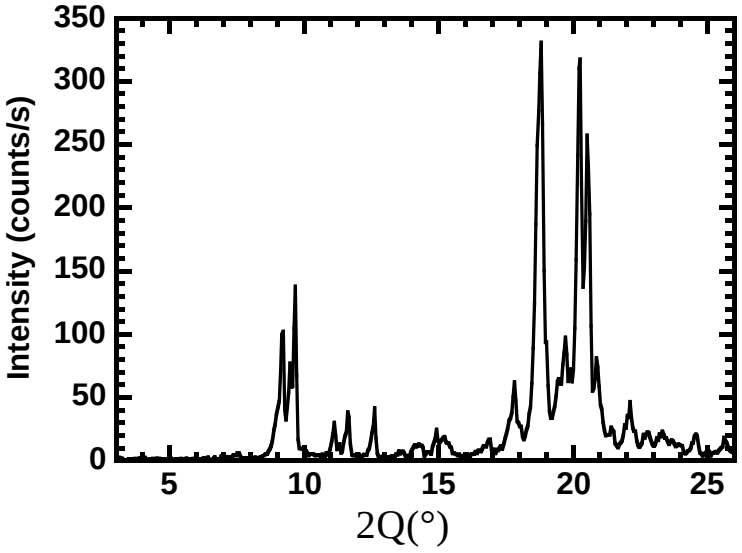

Figure 7.4: Diffractogram of PCBM powder.

Thus, the annealing of P3HT/PCBM composite films leads to better phase separation in conjugated polymer/fullerene blend, resulting in the formation of the polymer crystallites and in the growth of the fullerene clusters, as it is shown in Fig. 7.5a,b.

7.2 Effect of annealing on optical properties

The growth of the polymer crystallites leads also to drastic changes of optical properties of the composite P3HT/PCBM films. In the case of P3HT/PCBM composites, the changes in DF upon annealing are much stronger and more complicated compared to pristine P3HT films (Fig. 7.6).

In the UV spectral region $\hbar\omega > 3.2$ eV, the absorption coefficents are mainly determined by the optical transition of the PCBM at 3.67 eV. There are only minor changes in the magnitude of this PCBM peak between the untreated and the annealed samples.

There are three important differences between the DF of the annealed and the untreated film in energy region $\hbar\omega < 3.2$ eV:

- The local maximum of the imaginary part of the DF ε_2 around 2.5 eV is shifted to the lower photon energies. This is true for both parallel and perpendicular components of ε_2.

- The optical anisotropy is increased upon annealing.

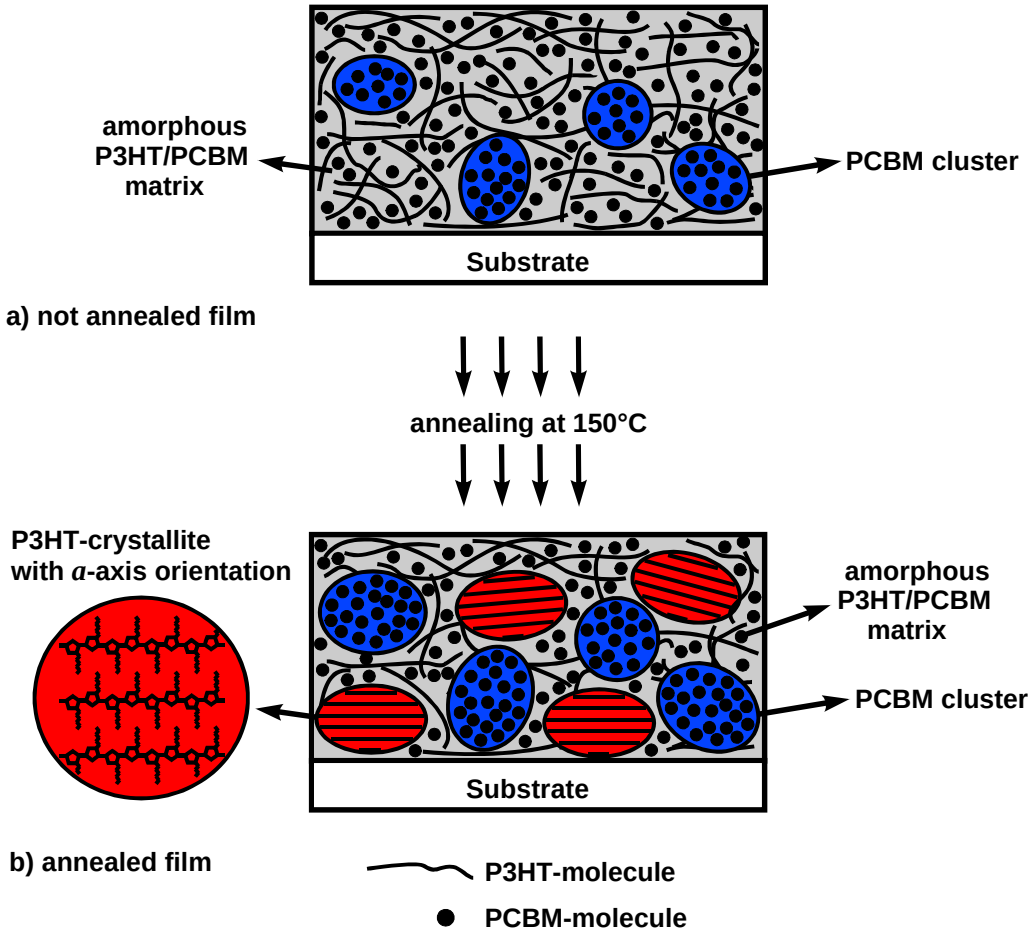

Figure 7.5: Model for structural changes of the composite P3HT/PCBM-film upon annealing.

- Both parallel and perpendicular components of ε_2 are increased upon annealing.

It has been shown [84, 85], that both absorption and emission maxima of conjugated polymers are shifted towards lower photon energies with increasing conjugation length. Therefore, the first phenomenon is obviously caused by increasing of the mean conjugation length upon annealing. The increase of the mean conjugation length is in a good agreement with XRD-measurements performed on the same films (see Fig. 7.1). From XRD-measurements, the formation of polymer crystallites was concluded. The conjugation length in crystallites is larger, because the polymer molecules within such crystallites are perfectly oriented and there are no defects like chain kinks, which limit the conjugation length. Thus, the mean conjugation length for annealed samples should be larger, resulting in the observed shift of the absorption maxima to the lower photon energies.

The increase of the optical anisotropy could be also explained by formation of

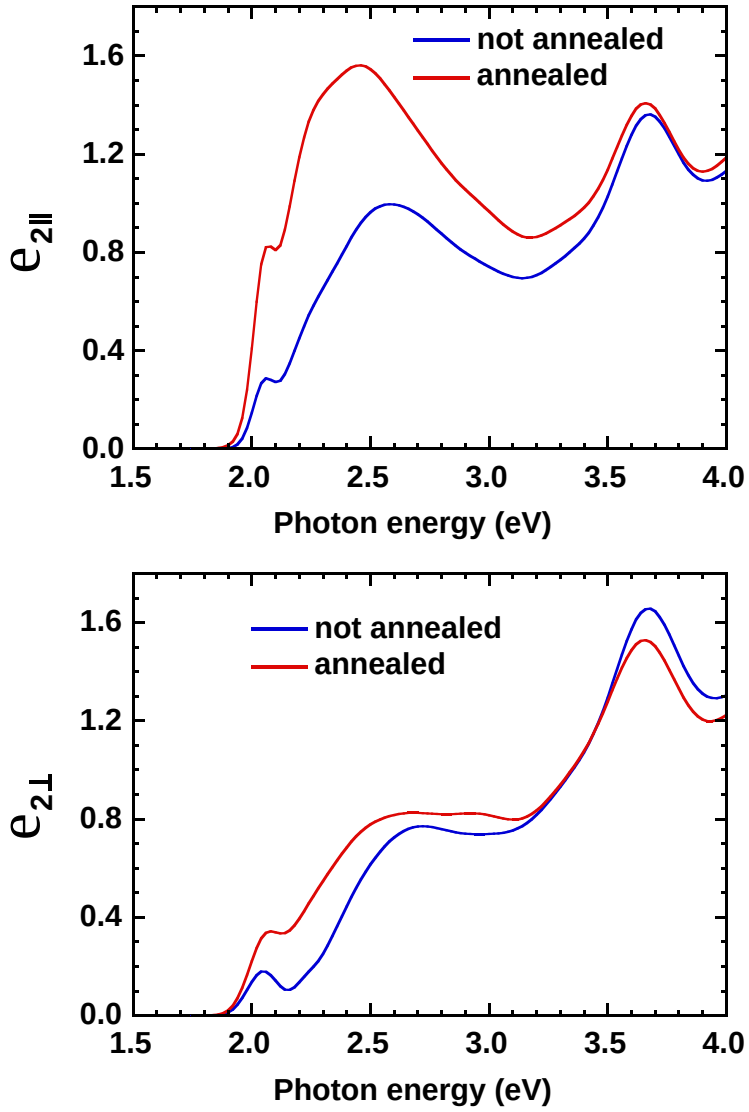

Figure 7.6: Imaginary part of the anisotropic DF of untreated and annealed at 150° P3HT:PCBM films.

the polymer crystallites. Such crystallites have a pronounced a-axis orientation (polymer backbone parallel to the substrate, Fig. 7.5). This results in higher optical anisotropy.

The third phenomenon, increase of both parallel and perpendicular components of ε_2 upon annealing, does not correlate with our measurements on pristine P3OT- (section 6.2.3) and P3HT-films (Fig. 6.17). In case of pristine polythiophene films, the increase of for example parallel component of ε_2 is followed by decrease of the perpendicular component and vice versa. The physical origin of these is the reorientation of the polymer molecules. If the polymer molecules becomes for example more aligned parallel to the substrate, the parallel component

should increase and the perpendicular component should decrease. The simultaneous increase of both parallel and perpendicular components of ε_2 can not be explained by reorientation of the polymer molecules only. We attribute the increase of the optical absorption to the change of the state of the aggregation of the P3HT from amorphous (in the case of the untreated film) to nanocrystalline (in the annealed film). Due to crystallisation of P3HT, the interaction between the P3HT molecules becomes stronger. We suppose that this is the origin of increased optical absorption in low photon energy region.

A question arises, whether the crystallisation of P3HT begins in the bulk or at the substrate. Before the annealing the P3HT/PCBM film is nearly isotropic, i. e. there is no preferable orientation of P3HT chains. If the crystallisation begins in the bulk, there is no reason why the P3HT molecules should change their orientation. Therefore, after annealing the P3HT crystallites should be randomly oriented, too. Such arrangement will lead to isotropic optical properties, which is in contradiction to observed strong optical anisotropy of the P3HT/PCBM films after annealing. We conclude, that the P3HT crystallisation begins at the substrate and propagates subsequently into the bulk. The first P3HT crystallites are a-axis oriented due to interaction with the substrate. This first layer determines the orientation of the P3HT crystallites in the bulk in an analogous manner as for pristine polythiophene films (section 6.2.3).

To obtain the maximum tilt angle of the polythiophene crystallites in the composite films θ_{MAX} as described in section 6.2.2, absorption of P3HT must be extracted from the anisotropic DF of the P3HT/PCBM composite. In the first approximation the imaginary part of the DF of the P3HT/PCBM composite $\varepsilon_{2||,\perp}^{BLEND}(\hbar\omega)$ can be written as a superposition of the imaginary parts of the DF's of the constituents:

$$\varepsilon_{2||,\perp}^{BLEND}(\hbar\omega) = f * \varepsilon_2^{PCBM}(\hbar\omega) + (1-f) * \varepsilon_{2||,\perp}^{P3HT}(\hbar\omega), \tag{7.1}$$

where $\varepsilon_2^{PCBM}(\hbar\omega)$ and $\varepsilon_{2||,\perp}^{P3HT}(\hbar\omega)$ are the DF's of PCBM and P3HT, respectively, and f=0.594 is the volume fraction of fullerene (P3HT and PCBM densities of 1.1 g/cm^3 and 1.5 g/cm^3, respectively, were taken). From (7.1), one obtains for the P3HT absorption:

$$(1-f) * \varepsilon_{2||,\perp}^{P3HT}(\hbar\omega) = \varepsilon_{2||,\perp}^{BLEND}(\hbar\omega) - f * \varepsilon_2^{PCBM}(\hbar\omega). \tag{7.2}$$

The calculated from (7.2) P3HT absorption for the annealed film is shown in Fig. 7.7. From this, the anisotropy parameter A and the maximum tilt angle

of the polythiophene crystallites θ_{MAX} can be calculated. We obtain from (6.1) A=1.34/0.514=2.6 and from Fig. 6.11 θ_{MAX}=44°. Thus, the P3HT crystallites are strongly oriented even in composites with PCBM.

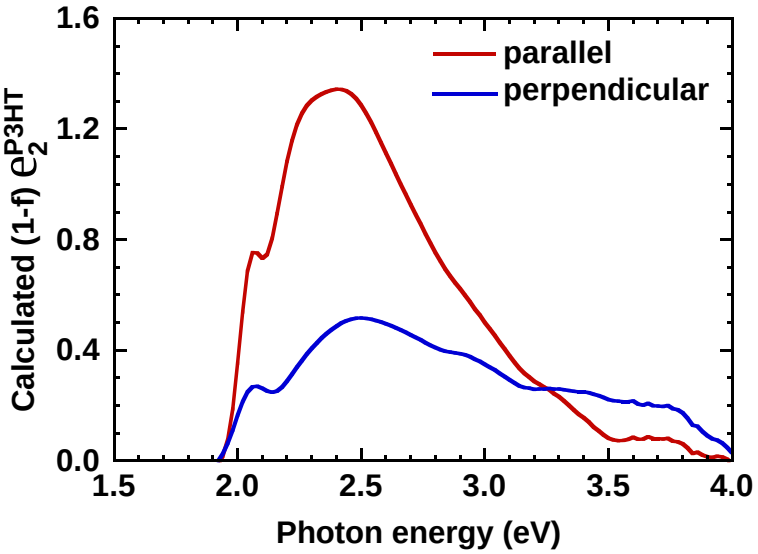

Figure 7.7: Calculated P3HT absorption in composite with PCBM.

7.3 Optical absorption as a function of P3HT crystallinity

It was shown in the last section, that the absorption of annealed P3HT/PCBM composite films is drastically increased due to crystallisation of P3HT. To study this phenomenon in detail, we investigated the crystallinity and the optical absorption of P3HT/PCBM films annealed at different temperatures.

The diffractogramms of not annealed and annealed at 100, 125 und 150°C P3HT/PCBM films are shown in Fig. 7.8a. The concentration of PCBM was 67 wt.%. The films were prepared by spin coating from chloroform solution. The films were annealed under nitrogen atmosphere for 5 min. The film thickness was 57±2 nm for all the samples.

The diffraction peak at 2θ=5.4° corresponding to P3HT crystallites with a-axis orientation is observed for all annealed samples. A weak diffraction peak at 2θ=10.8° is the second order of the 5.4° peak. To get structural information about the samples, the 5.4° peak was fitted with one gaussian. The determined peak height and peak width for the investigated four samples are shown in Table 7.1.

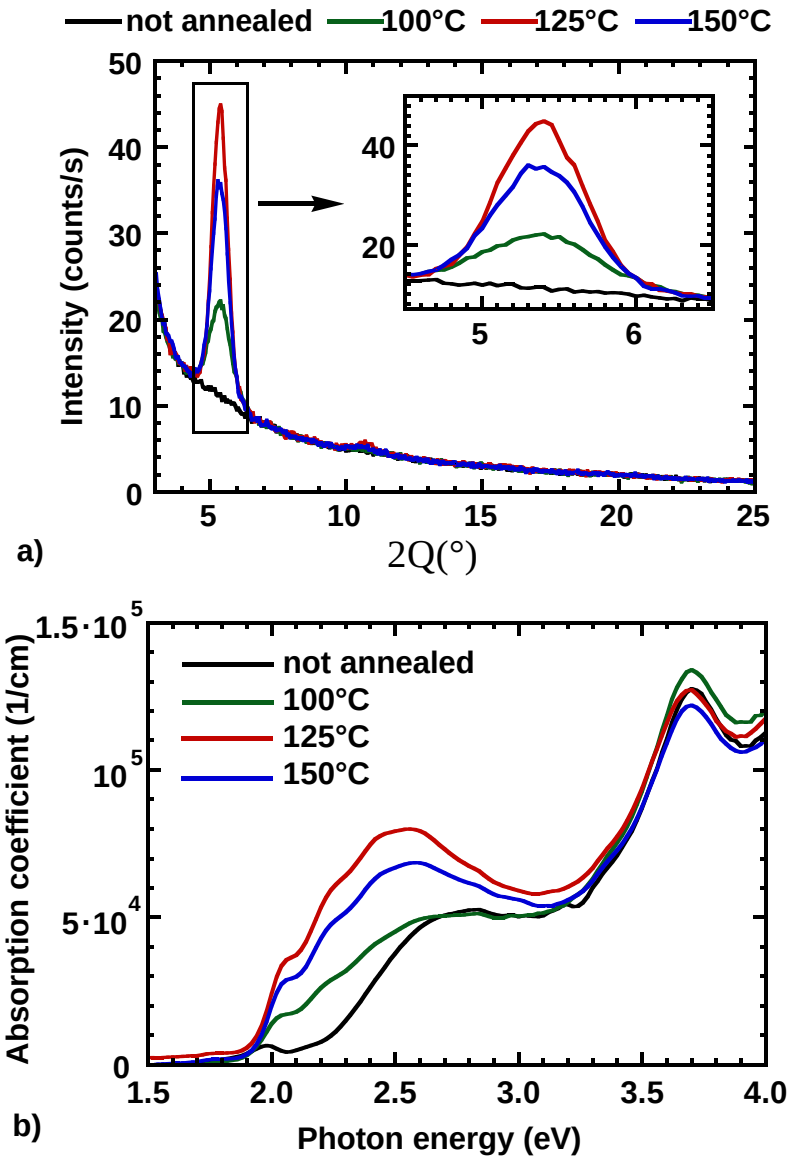

Figure 7.8: Diffractogramms (a) and absorption coefficients (b) of P3HT/PCBM 1/2 films in dependence on annealing temperature.

The peak position remains constant at $2\theta = (5.39 \pm 0.01)^\circ$. The mean crystallite size was calculated from Scherrer's relation (5.33). The P3HT crystallinity is defined as a product of the peak height and the peak width.

The lowest crystallinity was observed for the not annealed film. Upon annealing, the P3HT crystallinity is drastically increased. This is due to the increased thermal diffusion of PCBM molecules at elevated temperatures into larger PCBM aggregates and P3HT crystallisation in PCBM free regions (see the discussion in section 7.1). It is remarkable, that both the P3HT crystallinity and the P3HT crystallite size have a maximum for the annealing temperature of 125°C. Further

Table 7.1: Crystallinity of P3HT/PCBM films in dependence on annealing temperature.

Annealing temperature (°C)	Peak height (a. u.)	Peak width (°)	P3HT crystallite size (nm)	P3HT crystallinity (a. u.)
not annealed	∼0.7	∼1.5	∼5.3	∼1.1
100	11.3	0.91	8.8	10.3
125	33.5	0.65	12.2	21.7
150	25.2	0.71	11.2	17.9

increase of the annealing temperature leads to decrease of the P3HT crystallinity. We presume that the P3HT crystallites become unstable due to enhanced thermal motion of the P3HT molecules at high temperatures, which results in reduced P3HT crystallinity.

The absorption coefficients of the samples are shown in Fig. 7.8b. The magnitude of the absorption coefficient in the low photon energy region changes strongly. The lowest absorption coefficient is observed for the not annealed sample. In the case of the annealed samples, the magnitude of the absorption coefficient increases and the absorption maximum shifts to the lower photon energies in comparison to the not annealed sample. The origin of these effects was already discussed in section 7.2. The annealed at 125°C film have the highest absorption coefficient. Thus, there is a direct correlation between the crystallinity of the films and their optical absorption in the visible region of the spectrum.

To demonstrate the relation between the optical absorption and the film crystallinity more clearly, the absorption coefficients of the films at photon energies of 2.06 and 2.26 eV were plotted as a function of the P3HT crystallinity (Fig. 7.9). The absorption increases linearly (at 2.06 eV) or even superlinearly (at 2.26 eV) with increasing crystallinity. The intersection of the curves with ordinate gives the absorption of P3HT in amorphous state (crystallinity=0). From Fig. 7.9 it follows, that the contribution of amorphous P3HT to the absorption in low photon energy region can be neglected. Thus, the optical absorption in low photon energy region is determined by P3HT crystallinity.

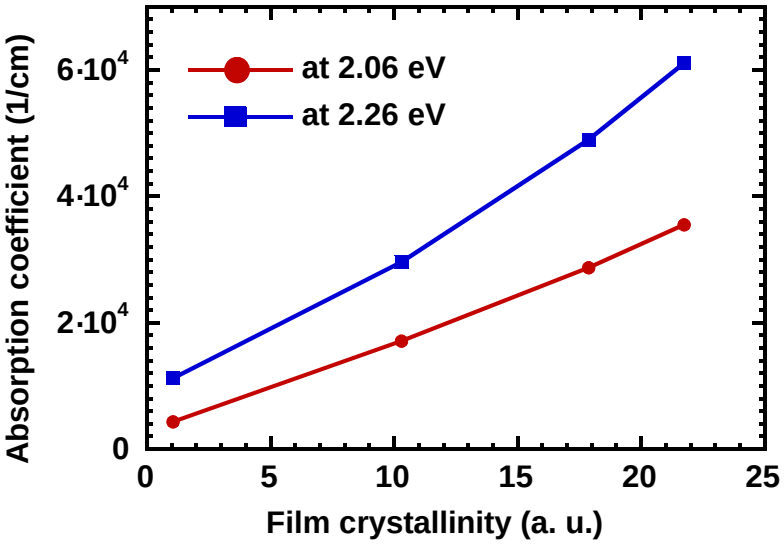

Figure 7.9: Absorption coefficient of P3HT/PCBM 1/2 films at 2.06 eV and 2.26 eV as a function of film crystallinity.

7.4 Effect of annealing on transport properties

Fig. 7.10 shows the current-voltage characteristic of solar cells made of the not annealed and annealed sample under 50 mW/cm^2 AM1.5 simulated illumination [65]. The open circuit voltage V_{OC} remains nearly unchanged for both cells. In terms of relative efficiency enhancement, an increase from 1.0% for the not annealed sample to 3.6% for the annealed sample is observed. The increase in the short circuit current density (J_{SC}) is more than a factor 2. The enhanced near IR absorption certainly contributes to the higher J_{SC} current densities, but the observed improvement can not be explained solely by the enhanced spectral contributions. Other mechanisms must be considered. Investigations of the light intensity dependence I_{ill} of J_{SC} showed that recombination is more relevant in the not annealed films. The scaling factor α ($J_{SC} \sim I_{ill}^{\alpha}$) is reduced to less than 0.9 for not annealed devices compared to 1.0 for annealed films, corresponding to a reduction of J_{SC} by at least 30-40% at 50 mW/cm^2 [65]. The reduction of recombination losses together with an enhanced spectral sensitivity can explain the increase in J_{SC}.

The reduction of recombination losses could in principle occur due to improvement of charge carrier mobilities and/or lifetimes. Since the polythiophene molecules are better ordered in the case of annealed polythiophene/fullerene films, it is reasonable to assume, that the hole mobility is higher for the annealed sample. This assumption is strongly supported by the measurements on pris-

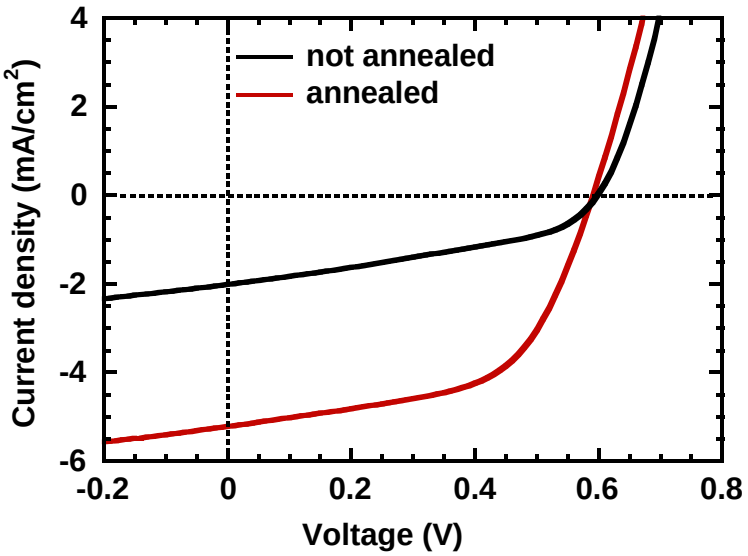

Figure 7.10: Current-voltage characteristics of the not annealed and the annealed P3HT/PCBM solar cells [65].

tine polythiophene films, where the significant increase of the out-of-plain hole mobility after annealing was observed (see section 6.3).

On the other hand, the density of the recombination centers is obviously lower for annealed film due to reduced interface area between polythiophene and fullerene (see Fig. 7.5). Most likely, this results in higher charge carrier lifetimes for annealed sample.

We conclude that morphology modifications upon annealing lead to improved transport properties and therefore to reduction of recombination losses.

Chapter 8

Conclusions and outlook

In this work, correlation between structural, optical and transport properties of polythiophene and polythiophene/fullerene films was studied. Thin pristine polythiophene films were found to be partially crystalline. Only the a-axis orientation of polythiophene crystallites (polymer main chain parallel and side chain perpendicular to the substrate) was observed. Our study shows, that the polythiophene films consist of a highly ordered interface layer on the polythiophene-substrate interface. The degree of the orientation of the polythiophene molecules within this interface layer depends on the strength of the short-range interaction between the polythiophene molecules and the substrate. After this well ordered layer, the order drops-off with a characteristic length of several tens of nanometers. The characteristic length (and therefore the degree of orientation of the polythiophene molecules in the bulk) depends on the time of the evaporation of the solvent (longer evaporation time results in improved order and vice versa). Annealing improves the overall crystallinity and anisotropy of the polythiophene films. From comparison with mobility data it was concluded, that the annealing support the formation of the polythiophene crystallites in the bulk and do not significantly change the ordering of the interface layer.

In the case of composite polythiophene/fullerene films, the polythiophene crystallites are a-axis oriented, too. On the contrary to the pristine polythiophene films, the crystallinity of not annealed polythiophene/fullerene samples is very low. The reason for this is that the fullerene molecules disturb the formation of the polythiophene crystallites. At elevated temperatures, the fullerene molecules become mobile and diffuse to the fullerene clusters. Due to the thermal diffusion of fullerene, regions with low fullerene concentration occurs. In this fullerene-free regions, the polythiophene can crystallise. As a result, polythiophene crystallites

and fullerene clusters are formed upon annealing of the films (see Fig. 8.1). Due to the crystallisation of polythiophene, the optical absorption and the hole mobility perpendicular to the film plane increases. The improved absorption of the annealed films together with improved transport properties result in an increase of the polythiophene/fullerene solar cell efficiency from 1.0% to 3.6%.

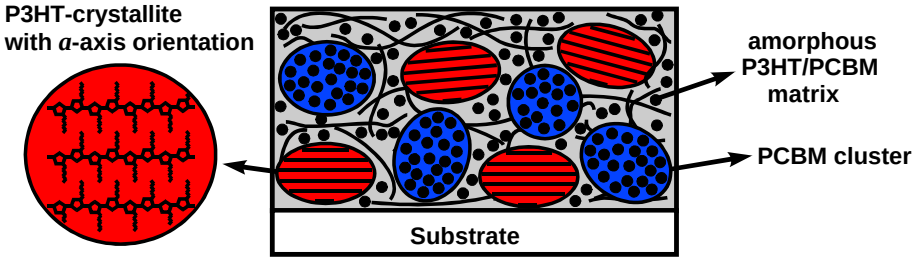

Figure 8.1: Structure of annealed P3HT/PCBM film.

This work contributes to better understanding of the correlation between the structure, the optical and the transport properties of the pristine polythiophene and composite polythiophene/fullerene films. In particular, a direct correlation between the optical absorption and the crystallinity of the films was demonstrated, which is useful for further optimisation of the polythiophene/fullerene solar cells. In the case of pristine polythiophene films, the correlation between the in-plane mobility and the optical anisotropy provides the possibility to study the ordering of the interface layer and to increase the performance of FET devices. Thus, the gained knowledge about film structure is of great importance from both fundamental and engineering points of view.

The most important results of this work are:

- first systematic study of the optical anisotropy of thin polythiophene films and
- first study of the correlation between crystallinity and optical properties of P3HT/PCBM thin films.

There are still some remaining questions which should be clarified in the future. One of the most important problems to our opinion is the determination of absolute fraction of the polythiophene crystallites in the polythiophene/fullerene blend. In this work, only relative polythiophene crystallinity could be estimated. The knowledge about the absolute volume fractions of crystalline and amorphous regions within the blend could help to understand much more better the physical processes in plastic solar cells.

Another challenge is to find out the parameters which affect the polythiophene crystallinity and the crystallite size. This study is already under work [86]. Some preliminary results were presented in [87].

On the basis of increased polythiophene/fullerene solar cell performance after annealing we concluded (section 7.4), that annealing leads to improvement of charge transport properties of polythiophene/fullerene blends. However, this conclusion should be supported by direct measurements of charge carrier mobilities (for example by time-of-flight technique) and lifetimes for untreated and annealed samples. Currently there is an effort to measure the charge carrier lifetimes in polythiophene/fullerene blends by photoinduced absorption spectroscopy [88, 89].

Abbreviations

AFM	atomic force microscopy
AM1.5	air mass 1.5 spectrum (see appendix C)
CB	conduction band
DF	dielectric function
EMA	effective medium approximation
FF	fill factor (see appendix C)
GID	grazing-incidence diffraction
HOMO	highest occupied molecular orbital
ITO	indium tin oxide
LUMO	lowest unoccupied molecular orbital
MDMO-PPV	poly[2-methoxy-5-(3,7-dimethyloctyloxy)-1,4-phenylenevinylene]
MEH-PPV	poly[2-methoxy-5-(2-ethyl-hexoxy)-1,4-phenylenevinylene]
MIS	metal-isolator-semiconductor
MSA	multiple sample analysis
MSE	mean square error
OFET	organic field effect transistor
OLED	organic light emitting diode
P3DDT, P3HT,	poly(3-dodecylthiophene), poly(3-hexylthiophene),
P3OT	poly(3-octylthiophene) (Fig. 4.1)
PCBM	[6,6]-phenyl-C61-butyric acid methyl ester (Fig. 4.2)
PET	polyethylenetherephtalate
PEDOT	poly(ethylene-dioxythiophene)
PIA	photoinduced absorption
PL	photoluminescence
PSS	poly-(styrene-sulphonic acid)
RAE	rotating analyser ellipsometer
SCLC	space charge limited current
SE	spectroscopic ellipsometry

SEM	scanning electron microscopy
TEM	transmission electron microscopy
ToF	time-of-flight
VASE	variable angle spectroscopic ellipsometer
VB	valence band
XRD	X-ray diffraction

Appendix A

3-phase model

In 3-phase model, the sample which consists of a thin isotropic film with film thickness D on a substrate placed in ambient with dielectric function $\tilde{\varepsilon}_0$ is considered (Fig. A.1). The dielectric functions of the film and the substrate are $\tilde{\varepsilon}$ and $\tilde{\varepsilon}_S$, respectively. The part of $p-$ or $s-$ polarized light absorbed by polymer (or by polymer/fullerene) film A can be expressed as:

$$A_{P,S} = 1 - R_{P,S} - T_{P,S}, \tag{A.1}$$

where R and T are the reflected and transmitted parts of light, respectively. They can be calculated as:

$$R_{P,S} = \left| \frac{\tilde{R}^{01}_{P,S} + \tilde{R}^{12}_{P,S} \exp(i2\beta)}{1 + \tilde{R}^{01}_{P,S}\tilde{R}^{12}_{P,S} \exp(i2\beta)} \right|^2, \tag{A.2}$$

$$T_{P,S} = Re\left[\frac{\sqrt{\tilde{\varepsilon}_0}\cos\tilde{\phi}_0}{\sqrt{\tilde{\varepsilon}_S}\cos\tilde{\phi}_2} \right] \left| \frac{\tilde{T}^{01}_{P,S}\tilde{T}^{12}_{P,S} \exp(i\beta)}{1 + \tilde{R}^{01}_{P,S}\tilde{R}^{12}_{P,S} \exp(i2\beta)} \right|^2, \tag{A.3}$$

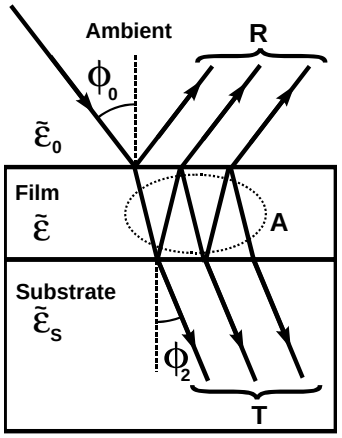

Figure A.1: 3-phase model.

where the $\tilde{R}^{01}_{P,S}, \tilde{T}^{01}_{P,S}$ and $\tilde{R}^{12}_{P,S}, \tilde{T}^{12}_{P,S}$ are the Fresnel reflection and transmission coefficients for ambient-film and film-substrate interfaces and β is a phase shift [58]. The phase shift β depend on the film thickness D, the dielectric function of the film $\tilde{\varepsilon}$ and on the angle of incidence.

In order to calculate the correction factor for photoluminescence quenching (see section 2.2, Eq. 2.8), the samples were measured with spectroscopic ellipsometry. From spectroscopic ellipsometry, the film thicknesses and the dielectric functions of polymer and polymer/fullerene films were determined. Applying these quantities to Eq. A.1, the absorption of the polymer and polymer/fullerene films for $p-$ and $s-$ polarization was calculated. Then, the average values were taken:

$$A_{polymer} = \frac{A_{polymer,P} + A_{polymer,S}}{2}, \tag{A.4}$$

$$A_{blend} = \frac{A_{blend,P} + A_{blend,S}}{2}. \tag{A.5}$$

After this, the correction factor K was calculated by eqn. 2.8:

$$K = \frac{A_{blend,P} + A_{blend,S}}{A_{polymer,P} + A_{polymer,S}}. \tag{A.6}$$

Appendix B

Conditions for efficient charge transport in plastic solar cell

Highly efficient **charge transport** of the separated charges is achieved if the extraction times for electrons and holes τ_e^{extr} and τ_h^{extr} are smaller than their recombination lifetimes τ_e and τ_h:

$$\tau_e^{extr} \ll \tau_e, \qquad \tau_h^{extr} \ll \tau_h. \tag{B.1}$$

The extraction time for electrons can be estimated by:

$$\tau_e^{extr} = D/v_e, \tag{B.2}$$

where D is the thickness of active layer and v_e is a velocity of the electron in applied electric field E, which is proportional to the electron mobility μ_e, i. e. $v_e = \mu_e E$. The maximum value for electric field E is $E = V_{OC}/D$. One obtains for Eq. (B.3):

$$\mu_e \tau_e \gg D^2/V_{OC}, \qquad \mu_h \tau_h \gg D^2/V_{OC}. \tag{B.3}$$

This is a **condition of efficient charge carrier transport in solar cell**. For example, assuming $D = 100nm$ and $V_{OC} = 0.5V$, one obtains for $\mu\tau$ product:

$$\mu_e \tau_e \gg 2 * 10^{-10} cm^2/V, \qquad \mu_h \tau_h \gg 2 * 10^{-10} cm^2/V. \tag{B.4}$$

Appendix C

Efficiency of an ideal plastic solar cell

C.1 Power conversion efficiency of solar cells: definition

The efficiency of a solar cell depends strongly on ambient conditions such as cell temperature, incident light intensity and incident light spectral content. The standard conditions are specified as [11]:

light intensity	1000 W/m^2,
light spectrum	AM 1.5,
sample temperature	25°.

The AM1.5 spectrum $I_{AM1.5}(\hbar\omega)$ (Fig. C.1) is the sun spectrum, modified by scattering and absorption in the atmosphere. This is a standard spectrum for which solar cell efficiencies are rated. The total energy current density obtained by integrating of the AM1.5 spectrum over the photon energy is 1000 W/m^2. For calculation of the solar cell efficiency, the number of incident photons per unit square per time $J_{AM1.5}(\hbar\omega)$ called the photon current density is more relevant. $J_{AM1.5}(\hbar\omega)$ is derived from $I_{AM1.5}(\hbar\omega)$ by dividing by the photon energy $\hbar\omega$:

$$J_{AM1.5}(\hbar\omega) = I_{AM1.5}(\hbar\omega)/\hbar\omega. \tag{C.1}$$

The resulting spectrum is shown in Fig. C.2.

The power conversion efficiency of a solar cell is defined as:

$$\eta = \frac{V_{OC} I_{SC} FF}{I_{LIGHT}}, \tag{C.2}$$

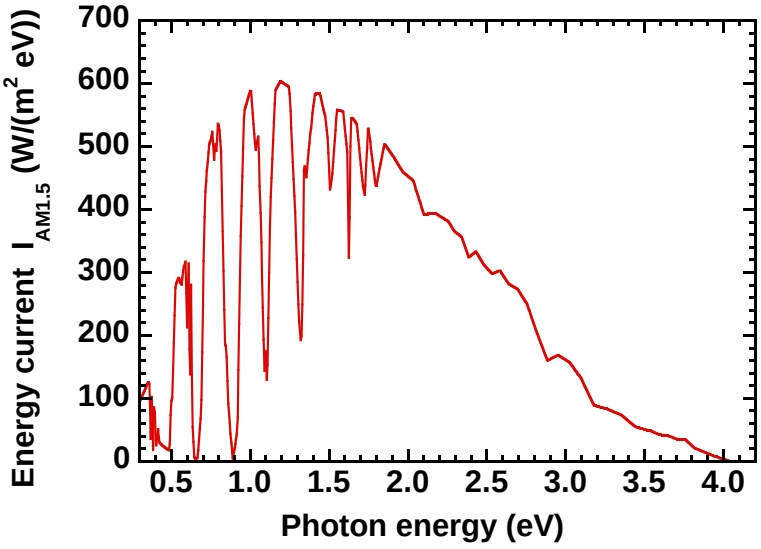

Figure C.1: Energy current density per photon energy of AM1.5 radiation.

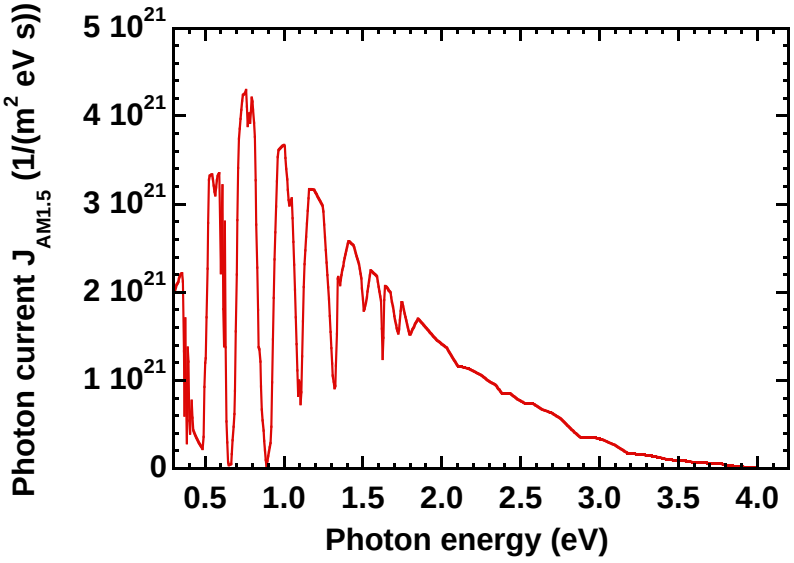

Figure C.2: Photon current density per photon energy of AM1.5 radiation.

where V_{OC} is the open circuit voltage in V, I_{SC} is the short circuit current density in A/m^2, FF is the fill factor, and I_{LIGHT} is the intensity of incident light in W/m^2, which equals 1000 W/m^2 in case of AM1.5 radiation. Thus, the efficiency of s solar cell is determined by three quantities: V_{OC}, I_{SC} and FF. In next sections, these quantities are considered separately.

C.2 Open circuit voltage

From the simple band diagram shown in Fig. 2.9, the open circuit voltage is equal to the difference between work functions of ITO and Aluminium, i. e.

$$V_{OC} = \frac{1}{e}(W_{ITO} - W_{ME}). \tag{C.3}$$

However, this simple model can not explain open circuit voltages observed in experiment. For ITO/(conjugated polymer/fullerene)/Aluminium devices the open circuit voltages of 800 mV [3, 90, 35] and higher were observed, in comparison to the 400 mV expected from the Eq. (C.3). In references [90] and [35], the influence of the work function W_{ME} of Me-electrode and the LUMO-level of the used fullerene derivatives $E_{LUMO}^{fullerene}$ on the open circuit voltage V_{OC} was systematically investigated. It was found out that the open circuit voltage V_{OC}:

- depends only slightly on the work function of Me electrode W_{ME};
- correlates with the LUMO-level of the used fullerene derivative.

Both findings are not consistent with MIM model, and could be explained by mechanism of Fermi-level pinning. The Fermi-level pinning means that the work function of Me electrode is pinned to the work function of the semiconductor. In our case, the work function of the metal is related to the LUMO of the fullerene. As an origin of this phenomenon, the strong charge transfer on the Me/fullerene interface is assumed [90, 35].

The open circuit voltage is determined by the difference between quasi Fermi levels for electron $E_{F,C}$ and holes $E_{F,V}$, i. e.

$$V_{OC} = \frac{1}{e}\left(E_{F,C} - E_{F,V}\right). \tag{C.4}$$

For a conventional $p-n$ junction solar cell with gap energy E_G, the V_{OC} can be written as [75, 11]

$$V_{OC} = \frac{E_G}{e} - \frac{kT}{e}\ln\left[\frac{1}{I_{SC}} e N_V N_C \left(\frac{L_n}{n\tau_n} + \frac{L_p}{p\tau_p}\right)\right], \tag{C.5}$$

where N_V and N_C are the effective densities of states in the valence and conduction band, L_n, L_p, n, p, τ_n and τ_p are the diffusion lengths, densities and lifetimes of electrons and holes, respectively. Thus, the open circuit voltage increases linearly with decreasing temperature and increases logarithmic with increasing short circuit current in an ideal $p-n$ junction solar cell.

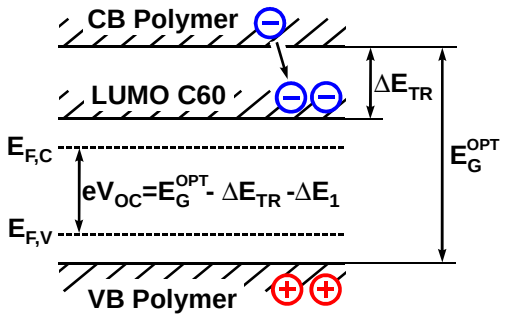

Figure C.3: Quasi-fermi levels in bulk heterojunction solar cell under illumination.

In case of a plastic bulk heterojunction solar cell, the energy loss ΔE_{TR} occurs due to ultra-fast electron transfer from polymer to fullerene (see Fig. C.3). For this reason, the "effective" band gap, which is the difference between the LUMO of fullerene and the valence band edge of the polymer $E_{LUMO}^{fullerene} - E_{VB}^{polymer}$ should be used instead of E_G^{OPT}. The Eq. (C.5) can be then written as:

$$V_{OC} = \frac{1}{e}\left(E_{LUMO}^{fullerene} - E_{VB}^{polymer}\right) - \frac{kT}{e}\ln\left(\frac{C}{I_{SC}}\right), \tag{C.6}$$

where

$$C = eN_V N_C\left(\frac{L_n}{n\tau_n} + \frac{L_p}{p\tau_p}\right). \tag{C.7}$$

In fact, similar behavior (i. e. decrease of the open circuit voltage with increasing temperature) was observed for P3HT/PCBM [75] and MDMO-PPV/PCBM [11] solar cells. For MDMO-PPV/PCBM solar cell, the open circuit voltage of nearly 1.33-1.40 V by T=0K was obtained by extrapolating the measured $V_{OC}(T)$ dependence to the T=0K. This value is in a good agreement with the theoretical value of $(E_{LUMO}^{PCBM} - E_{VB}^{MDMO-PPV}) = 1.45$ eV.

In further consideration, the energy loss due to the quasi-fermi level splitting

$$\Delta E_{QF} = kT\ln\left(\frac{C}{I_{SC}}\right) \tag{C.8}$$

is used. Taking into account that $E_{LUMO}^{fullerene} - E_{VB}^{polymer} = E_G^{OPT} - \Delta E_{TR}$, the open circuit voltage of conjugated polymer/fullerene solar cell can be written as:

$$V_{OC} = \frac{1}{e}\left(E_G^{OPT} - \Delta E_{TR} - \Delta E_{QF}\right). \tag{C.9}$$

Thus, the open circuit voltage of bulk heterojunction solar cell is determined by optical gap of the used conjugated polymer E_G^{OPT}, energy loss due to photoinduced electron transfer ΔE_{TR} and energy loss due to the quasi-fermi levels splitting ΔE_{QF}.

Since both the conjugated polymer and the fullerene in bulk heterojunction are undoped in the dark, the constant C and the energy loss due to the quasi-fermi levels splitting ΔE_{QF} can not be directly calculated from the Eqs. (C.7) and (C.8), respectively. The ΔE_{QF} equals 0.55 eV for MDMO-PPV/PCBM and nearly 0.85 eV for P3HT/PCBM solar cells at room temperature and high light intensities. The origin of these values is still not well understood.

For further consideration we introduce the total energy loss ΔE in plastic solar cell, which is the sum of the energy losses due to the photoinduced electron transfer ΔE_{TR} and the energy loss due to quasi-fermi level splitting ΔE_{QF}:

$$\Delta E = \Delta E_{TR} + \Delta E_{QF}. \tag{C.10}$$

Using (C.10), (C.11) can be written as

$$V_{OC} = \frac{1}{e}\left(E_G^{OPT} - \Delta E\right). \tag{C.11}$$

Thus, the total energy loss describes the difference between the optical gap and the open circuit voltage.

ΔE is nearly 0.4 eV in Si ($E_G^{OPT} = 1.12$ eV, $V_{OC} = 0.71$ V) and GaAs ($E_G^{OPT} = 1.42$ eV, $V_{OC} = 1.02$ V) solar cells. In plastic solar cells the ΔE with nearly 1.35 eV (P3HT/PCBM cells: $E_G^{OPT} = 1.95$ eV, $V_{OC} = 0.6$ V; MDMO-PPV/PCBM cells: $E_G^{OPT} = 2.15$ eV, $V_{OC} = 0.85$ V) is much higher. As it will be shown below, the very high value of ΔE is the main reason for low efficiencies of the plastic solar cells.

C.3 Fill factor

The fill factor is defined as:

$$FF = \frac{V_{MP} I_{MP}}{V_{OC} I_{SC}}, \tag{C.12}$$

where V_{MP} and I_{MP} are the voltage and the current at the maximum power point of the I/V characteristic. The fill factor for an ideal solar cell can be easily calculated from ideal current/voltage diode characteristic:

$$I(V) = I_0 \left[\exp\left(\frac{eV}{kT}\right) - 1\right] - I_{SC}, \tag{C.13}$$

where V is applied voltage, I_{SC} is a short circuit current and I_0 is the reverse saturation current. Open circuit voltage V_{OC} is determined by I_0. The ideal

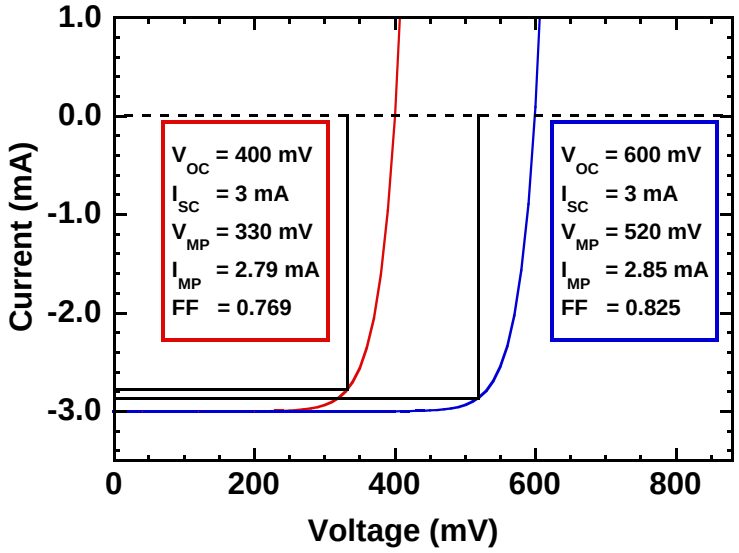

Figure C.4: IV-characteristics of ideal solar cells.

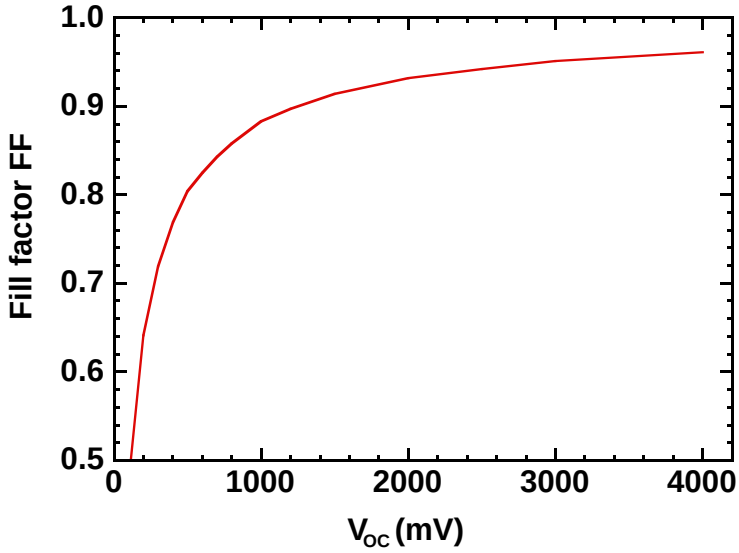

Figure C.5: Fill factor FF of ideal solar cell in dependence on the open circuit voltage V_{OC}.

solar cell I/V characteristics for $V_{OC} = 0.4$ V and $V_{OC} = 0.6$ V are shown in Fig. C.4. From the ideal I/V characteristics, the fill factor FF in dependence on the open circuit voltage could be easily calculated numerically from (C.12). The result is shown in Fig. C.5.

In order to describe the I/V characteristics of the practical solar cell, a series and a parallel resistance ([11], p. 214) are introduced. The series resistance originates from the finite conductivity of ITO layer, and from limited conductivity of the polymer (or fullerene) of the active layer. The parallel resistance occurs

due to impurities of the active layer and due to local short circuits between ITO and Me electrodes ("pin defects"). Both series and parallel resistances shift the maximum power point towards the lower output power and reduce therefore the fill factor. Thus, the fill factor obtained from ideal I/V characteristic is the highest possible value for the practical solar cell.

The fill factors of the best anorganic solar cells are very close to their theoretical limits. For example, the fill factor for Si (V_{OC} = 0.706 V) and GaAs (V_{OC} = 1.02 V) solar cells reach the values of 82.8% and 87.1%, respectively. The theoretical limits for these cells obtained from Fig. C.5 are 84.2% and 88.3%, respectively. The obtained fill factors of plastic solar cells (typical open circuit voltages of 0.5-0.9 V) with 50-60% are very low in comparison to the highest possible values of 80-87%. This is because of high contact resistance and low charge carrier mobilities. Thus, using better contacts and organic materials with higher charge carrier mobilities, the fill factor can be in principle increased by up to 50%.

C.4 Short circuit current

The short circuit current of a plastic solar cell is limited by following four processes:

- **absorption of light** and generation of excitons;
- **exciton dissociation** due to ultrafast electron transfer;
- **transport** of the separated charge carriers to the electrodes;
- **optical losses** within the device.

The absorption of light, i. e. the number of absorbed photons per square per time N, can be calculated for the case of relatively thick ($D \gg 1/\alpha_{blend}^{max}$, see Eq. (D.2)) active layer, consisting of the conjugated polymer with optical band gap E_G^{OPT} and the fullerene. In this case, each photon with energy $\hbar\omega > E_G^{OPT}$ is absorbed by polymer, whereas the photons with energy $\hbar\omega < E_G^{OPT}$ are not absorbed. The absorption of the fullerene can be neglected in this consideration, because 1) the absorption of the fullerene is very weak in the spectral region up to 3 eV, and 2) the photons absorbed by fullerene do not significantly contribute to the photocurrent [91]. The number of the absorbed photons N can be found

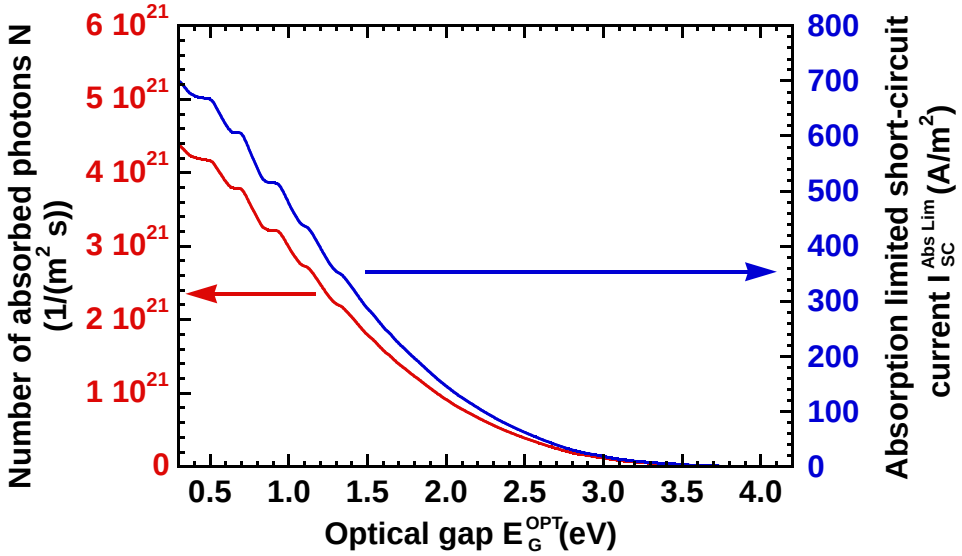

Figure C.6: Number of absorbed photons and absorption limited short circuit current in dependence on the optical gap E_G^{OPT} for AM1.5 radiation.

by integrating of photon current density $J_{AM1.5}(\hbar\omega)$ over the spectral range from E_G^{OPT} to ∞:

$$N = \int_{E_G^{OPT}}^{\infty} J_{AM1.5}(\hbar\omega) d(\hbar\omega). \tag{C.14}$$

The result of numerical integration in dependence on the optical gap E_G^{OPT} is presented in Fig. C.6.

As it was already mentioned in section 2.2, the efficiency of exciton dissociation η_{PET} is rather high ($\eta_{PET} > 95\%$) for all of the investigated conjugated polymer/fullerene composites. Therefore, the losses by exciton dissociation are neglected in further consideration.

Optical losses in plastic solar cells occur due to reflection of light from the substrate and due to undesired absorption of light within the substrate (in UV region), the ITO- and the PEDOT-layers [92, 93].

Highly efficient charge transport of the separated charges is achieved if the extraction times for electrons and holes are smaller than their recombination lifetimes τ_e and τ_h (B.3).

Assuming, that the optical losses are negligible and that all absorbed photons are converted to free charge carriers and are transported to the corresponding electrodes without recombination, i. e. no losses occurs during the exciton dissociation and during the transport of the charge carriers to the electrodes, the

absorption limited short circuit current I_{SC}^{AbsLim} can be obtained by multiplying (C.14) with elemental charge e:

$$I_{SC}^{AbsLim} = e \int_{E_G^{OPT}}^{\infty} J_{AM1.5}(\hbar\omega) d(\hbar\omega). \tag{C.15}$$

I_{SC}^{AbsLim} is also shown in Fig. C.6. The absorption limited short circuit current I_{SC}^{AbsLim} determines thus the highest possible short circuit current.

Again, the short circuit current of real Si and GaAs solar cells with $I_{SC} = 422$ A/m^2 and $I_{SC} = 282$ A/m^2, respectively, are very close to the values calculated from (C.15). For the optical gaps of 1.12 eV (Si) and 1.42 eV (GaAs) one obtains $I_{SC} = 434$ A/m^2 and $I_{SC} = 317$ A/m^2, respectively. In P3HT/PCBM and in MDMO-PPV/PCBM plastic solar cells (optical gaps of 1.95 eV and 2.15 eV, respectively) these values are $I_{SC} = 157$ A/m^2 and $I_{SC} = 116$ A/m^2, respectively. In praxis, however, much lower short circuit currents of 85 A/m^2 for P3HT/PCBM [4] and 53 A/m^2 for MDMO-PPV/PCBM [3] solar cells at light intensity of 800 W/m^2 were obtained. Assuming for simplicity that the external quantum efficiency of these cells does not decrease by increasing the intensity of incident light, one obtains the short circuit currents of 106 A/m^2 and 66 A/m^2 for P3HT/PCBM and MDMO-PPV/PCBM solar cells by illumination with 1000 W/m^2 light, respectively. These values are still too low in comparison to the calculated ones ($I_{SC} = 157$ A/m^2 and $I_{SC} = 116$ A/m^2) and therefore should be further improved by using higher film thickness according to Eq. D.2 and materials with improved charge carrier mobilities and lifetimes according to Eq. (B.3). In ideal case the short circuit current could be increased by 50-75%.

C.5 Power conversion efficiency of an ideal plastic solar cell

From the calculated open circuit voltage V_{OC} (Eq. (C.11)), fill factor FF (Fig. C.5) and short circuit current I_{SC} (Fig. C.15), the power conversion efficiency of an ideal plastic solar cell η_{max} can be calculated from Eq. (C.2). The calculated efficiency η_{max} is shown on Fig. C.7 as a function of the optical gap E_G^{OPT} and total energy loss ΔE, which is the sum of the energy losses due to the photoinduced electron transfer ΔE_{TR} and the quasi-fermi level splitting ΔE_{FS}: $\Delta E = \Delta E_{TR} + \Delta E_{FS}$.

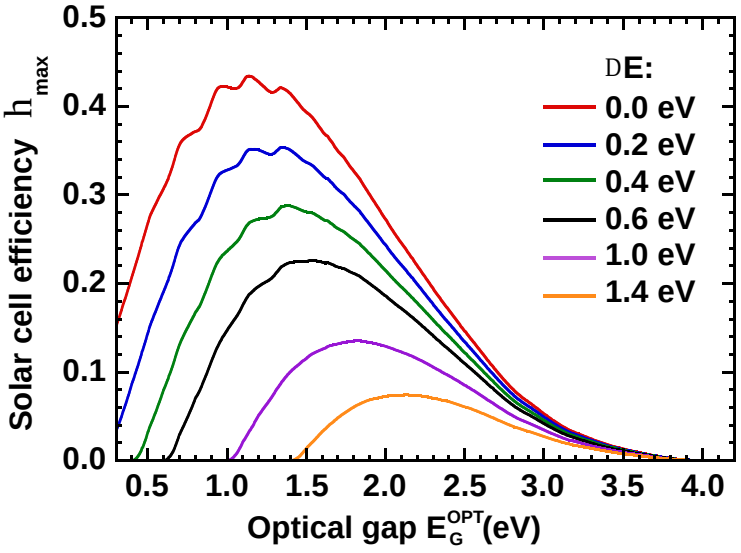

Figure C.7: Maximum efficiency of ideal plastic solar cell in dependence on the optical gap E_G^{OPT} and on total energy loss ΔE, calculated for AM1.5 radiation.

From Fig. C.7, the optical band gap E_G^{OPT} is a decisive parameter for theoretically achievable solar cell efficiency η_{max}. In particular, the optical band gap between 1.0 and 2.0 eV is necessary to achieve high solar cell efficiencies. The optimal value for optical gap, dependent on the total energy loss ΔE, lies at nearly 1.5eV.

The efficiency depends strongly not only on the optical band gap E_G^{OPT}, but also on the total energy loss ΔE. For instance, assuming the total energy loss $\Delta E = 1.4$ eV, what is state of the art for MDMO-PPV/PCBM and P3HT/PCBM solar cells, the maximum solar cell efficiency of only $\eta_{max} = 7.5\%$ can be achieved in principle (see the curve corresponding to $\Delta E = 1.4$ eV in Fig. C.7) using material with optical gap of $E_G^{OPT} \simeq 2.1$ eV. It is remarkable, that the band gaps of both P3HT with $E_G^{OPT}(P3HT) = 1.95$ eV and MDMO-PPV with $E_G^{OPT}(MDMO - PPV) = 2.15$ eV are lying very close to the optimal value of 2.1 eV. It is often claimed, that the efficiency of plastic solar cell can be improved by using the low-band gap ($E_G^{OPT} < 2.0$ eV) materials. Our calculations show, however, that without significant reduce of total energy loss ΔE opposite effect (i. e. decrease of the efficiency, see Fig. C.7, $\Delta E = 1.4$ eV curve) is expected. On the other hand, the reduction of ΔE to 1.0 eV allows the efficiencies up to 11-13% even with P3HT or MDMO-PPV.

Thus, the significant increase of the solar cell efficiency can be achieved only

due to the reduce of total energy loss ΔE. This can be done by reducing the ΔE_{TR} and/or the ΔE_{FS}. The ΔE_{TR} can be minimised by adjusting the conduction band edge of the polymer to the LUMO level of the fullerene or vice versa. It was shown [37], that the energy difference of only 0.15 eV is already sufficient for efficient electron transfer.

Currently there is no theory which correctly describes the ΔE_{FS} observed in plastic solar cells. The semiconductor theory of $p-n$ junction can not be applied in this case. In order to reduce the ΔE_{FS}, the fundamental knowledge of this phenomenon is needed.

Appendix D

Required thickness of the active layer

Generally, a sophisticated optical modelling of organic photovoltaic devices is required to calculate the energy absorbed in the active layer [93, 92]. Neglecting the reflection of incident light from the substrate, interference effects and assuming the 100% reflection from the metal electrode, one obtains a very rough estimation of the part of absorbed light $A(\hbar\omega)$:

$$A(\hbar\omega) = 1 - \exp\left(-2\,\alpha_{blend}(\hbar\omega)\,D\right), \tag{D.1}$$

where D is the thickness of the active layer (the factor 2 in the exponent indicate that light passes the active layer two times). In order to achieve high conversion efficiency, the part of absorbed light $A(\hbar\omega)$ should be as high as possible. Changing the film thickness D as

$$D > 1/\alpha_{blend}^{max} \tag{D.2}$$

leads to the absorption of more than 86% of incident light ($A > 1 - \exp(-2) = 0.86$) at photon energy corresponding to the maximum of the absorption coefficient α_{blend}^{max}. Further increase of the film thickness improves the absorption of light only slightly. Thus, the condition (D.2) determines the film thickness needed for effective absorption of the light. For example, for MDMO-PPV/PCBM composite with fullerene fraction of 75% and $\alpha_{blend}^{max} = 6.0 * 10^4\,\mathrm{cm}^{-1}$ one obtains for the film thickness $D > 166$ nm.

List of Figures

Bibliography

[1] C. J. Brabec, *Technological achievements and perspectives of plastic solar cells,* Lecture, Symposium for final review of Christian Doppler laboratory for plastic solar cells, 8. October 2004, Linz (Austria)

[2] M. A. Green, K. Emery, D. L. King, S. Igari, W. Warta, Prog. Photovolt. **12**, 365 (2004)

[3] S. E. Shaheen, C. J. Brabec, N. S. Sariciftci, F. Padinger, T. Fromherz, J. C. Hummelen, Appl. Phys. Lett. **78**, 841 (2001)

[4] F. Padinger, R. S. Rittberger, N. S. Sariciftci, Adv. Func. Mat. **13**, 85 (2003)

[5] From "Introduction Lecture of Prof. Sariciftci" (LIOS Linz)

[6] M. Al-Ibrahim, H.-K. Roth, S. Sensfuss, Appl. Phys. Lett. **85**, 1481 (2004)

[7] J. M. Kroon, M. M. Wienk, W. J. H. Verhees, J. C. Hummelen, Thin Solid Films **403**, 223 (2002)

[8] X. Yang, J. K. J. van Duren, R. A. J. Janssen, M. A. J. Michels, J. Loos, Macromolecules **37**, 2151 (2004)

[9] J. K. J. van Duren, X. Yang, J. Loos, C. W. T. Bulle-Lieuwma, A. B. Sieval, J. C. Hummelen, R. A. J. Janssen, Adv. Func. Mat. **14**, 425 (2004)

[10] H. Hoppe, M. Niggemann, C. Winder, J. Kraut, R. Hiesgen, A. Hinsch, D. Meissner, N. S. Sariciftci, Adv. Func. Mat. **14**, 1005 (2004)

[11] C. J. Brabec, V. Dyakonov, J. Parisi, N. S. Sariciftci, *Organic Photovoltaics: Concepts and Realization* (Springer, Berlin, 2003)

[12] A. J. Heeger, S. Kivelson, J. R. Schrieffer, W. P. Su, Rev. Mod. Phys. **60**, 781 (1988)

[13] M. C. Scharber, C. Winder, H. Neugebauer, N. S. Sariciftci, Synth. Met. **141**, 109 (2004)

[14] Y. A. Udum, K. Pekmez, A. Yildiz, Synth. Met. **142**, 7 (2004)

[15] H. Sirringhaus, P. J. Brown, R. H. Friend, M. M. Nielsen, K. Bechgaard, B. M. W. Langeveld-Voss, A. J. H. Spiering, R. A. J. Janssen, E. W. Meijer, Synth. Met. **111**, 129 (2000)

[16] K. E. Paul, W. S. Wong, S. E. Ready, R. A. Street, Appl. Phys. Lett. **83**, 2070 (2003)

[17] S. Hoshino, Yoshida, S. Uemura, T. Kodzasa, T. Kamata, J. Photopolymer Sci. Tech. **17**, 327 (2004)

[18] S. Nagamatsu, W. Takashima, K. Kaneto, Y. Yoshida, N. Tanigaki, K. Yase, Appl. Phys. Lett. **84**, 4608 (2004)

[19] S. A. Choulis, J. Nelson, Y. Kim, D. Poplavskyy, T. Kreouzis, J. R. Durrant, D. D. C. Bradley, Appl. Phys. Lett. **83**, 3812 (2003)

[20] M. Halik, H. Klauk, U. Zschieschang, G. Schmid, W. Radlik, S. Ponomarenko, S. Kirchmeyer, W. Weber, J. Appl. Phys. **93**, 2977 (2003)

[21] Y. Kato, S. Iba, R. Teramoto, T. Sekitani, T. Someya, H. Kawaguchi, T. Sakurai, Appl. Phys. Lett. **84**, 3789 (2004)

[22] T. Minari, T. Nemoto, S. Isoda, J. Appl. Phys. **96**, 769 (2004)

[23] C. Jacoboni, C. Canali, G. Ottaviani, A. A. Quaranta, Solid State Electron. **20**, 77 (1977)

[24] R. K. Willardson, A. C. Beer, *Semiconductors and Semimetals*, Band 10 (Academic Press, New York, 1975)

[25] V. X. Butko, X. Chi, D. V. Lang, A. P. Ramirez, Appl. Phys. Lett. **83**, 4773 (2003)

[26] K. Sakurai, H. Tachibana, N. Shiga, C. Terakura, M. Matsumoto, Y. Tokura, Phys. Rev. B **56**, 9552 (1997)

[27] U. Zhokhavets, R. Goldhahn, G. Gobsch, W. Schliefke, Synth. Met. **138**, 491 (2003)

[28] J.-W. van der Horst, P. A. Bobbert, P. H. L. de Jing, M. A. J. Michels, G. Brocks, P. J. Kelly, Phys. Rev. B **61**, 15817 (2000)

[29] M. Liess, S. Jeglinski, Z. V. Vardeny, M. Ozaki, K. Yoshino, Y. Ding, T. Barton, Phys. Rev. B **56**, 15712 (1997)

[30] R. Rinaldi, R. Cingolani, K. M. Jones, A. A. Baski, H. Morkoc, A. Di Carlo, J. Widany, F. Della Sala, P. Lugli, Phys. Rev. B **63**, 075311 (2001)

[31] S. F. Alvarado, P. F. Seidler, D. G. Lidzey, D. D. C. Bradley, Phys. Rev. Lett. **81**, 1082 (1998)

[32] P. Y. Yu, M. Cardona, *Fundamentals of Semiconductors* (Springer, Berlin, 1999)

[33] T. G. Pedersen, Phys. Rev. B **62**, 15424 (2000)

[34] G. Yu, K. Pakbaz, A. J. Heeger, Appl. Phys. Lett. **64**, 3422 (1994)

[35] C. J. Brabec, A. Cravino, D. Meissner, N. S. Sariciftci, M. T. Rispens, L. Sanchez, J. C. Hummelen, T. Fromherz, Thin Solid Films **403**, 368 (2002)

[36] N. S. Sariciftci, L. Smilowitz, A. J. Heeger, F. Wudl, Science **258**, 1474 (1992)

[37] M. Al-Ibrahim, A. Konkin, H.-K. Roth, D.A.M. Egbe, E. Klemm, U. Zhokhavets, G. Gobsch, S. Sensfuss, Thin Solid Films **474**, 201 (2005)

[38] M. Al-Ibrahim, H.-K. Roth, U. Zhokhavets, G. Gobsch, S. Sensfuss, Solar Energy Materials and Solar Cells **85**, 13 (2005)

[39] C. J. Brabec, Solar Energy Materials and Solar Cells **83**, 273 (2004)

[40] J. Nelson, Phys. Rev. B **67**, 155209 (2003)

[41] H. Hoppe, N. S. Sariciftci, J. Mat. Res. **19**, 1924 (2004)

[42] D. Chirvase, J. Parisi, J. C. Hummelen, V. Dyakonov, Nanotechnology **15**, 1317 (2004)

[43] K. E. Aasmundtveit, E. J. Samuelsen, M. Guldstein, C. Steinsland, O. Flornes, C. Fagermo, T. M. Seeberg, L. A. A. Pettersson, O. Inganas, R. Feidenhans'l, S. Ferrer, Macromolecules **33**, 3120 (2000)

[44] H. J. Fell, E. J. Samuelsen, J. Als-Nielsen, G. Grubel, J. Mardalen, Solid State Comm. **94**, 843 (1995)

[45] D. Comoretto, G. Dellepiane, F. Marabelli, J. Cornil, D. A. Santos, J. L. Bredas, D. Moses, Phys. Rev. B **62**, 10173 (2000)

[46] D. McBranch, I. H. Campbell, D. L. Smith, J. P. Ferraris, Appl. Phys. Lett. **66**, 1175 (1995)

[47] L. A. A. Pettersson, F. Carlsson, O. Inganas, H. Arwin, Thin Solid Films **313-314**, 356 (1998)

[48] R. W. Gymer, R. H. Friend, H. Ahmed, P. L. Burn, A. M. Kraft, A. B. Holmes, Synth. Met. **55-57**, 3683 (1993)

[49] J. Sturm, S. Tasch, A. Niko, G. Leising, E. Toussaere, J. Zyss, T. C. Kowalczyk, K. D. Singer, U. Scherf, J. Huber, Thin Solid Films **298**, 138 (1997)

[50] M. Tammer, P. Monkman, Adv. Mat. **14**, 210 (2002)

[51] C. M. Ramsdale, N. C. Greenham, Adv. Mat. **14**, 212 (2002)

[52] H. Sirringhaus, R. J. Wilson, R. H. Friend, M. Inbasekaran, W. Wu, E. P. Woo, M. Grell, D. D. C. Bradley, Appl. Phys. Lett. **77**, 406 (2000)

[53] P. Gattinger, H. Rengel, D. Neher, M. Gurka, M. Buck, A. M. van de Craats, J. M. Warman, J. Phys. Chem. B **103**, 3179 (1999)

[54] E. Punkka, M. F. Rubner, Synth. Met. **41-43**, 1509 (1991)

[55] *Guide to using WVASE32* (J. A. Woollam co., Inc., 1995)

[56] M. Born, E. Wolf, *Principles of Optics* (Cambridge University Press, Berlin, 1999)

[57] D. Meschede, *Gerthsen Physik* (Springer, Berlin, 2002)

[58] R. M. A. Azzam, N. M. Bashara, *Ellipsometry and polarized light* (North-Holland, Amsterdam, 1979)

[59] M. Campoy-Quiles, U. Zhokhavets, *Determination of out-of-plane optical anisotropies of conjugated polymer films,* private communication

[60] T. Erb, *Untersuchung der optischen und strukturellen Eigenschaften von Poly(3-Alkylthiophen)/Fulleren-Mischfilmen für organische Solarzellen* (2004)

[61] B. D. Cullity, *Elements of X-Ray Diffraction* (Addison-Wesley Publishing Company, Inc., 1956)

[62] Programmed by Norbert Stein (TU Ilmenau)

[63] T. J. Prosa, M. J. Winokur, Macromolecules **25**, 4364 (1992)

[64] T. Erb, S. Raleva, U. Zhokhavets, G. Gobsch, B. Stühn, M. Spode, O. Ambacher, Thin Solid Films **450**, 97 (2004)

[65] T. Erb, U. Zhokhavets, G. Gobsch, S. Raleva, B. Stühn, P. Schilinsky, C. Waldauf, C. Brabec, Adv. Func. Mat. (2005 (accepted))

[66] T. Erb, U. Zhokhavets, G. Gobsch, M. Al-Ibrahim, P. Schilinsky, C. Waldauf, C. Brabec, *X-ray diffraction study of morphology of active layers for organic solar cells,* Poster, Technologies for Polymer Electronics 04, 28.-30 September 2004, Rudolstadt (Germany)

[67] U. Zhokhavets, R. Goldhahn, G. Gobsch, M. Al-Ibrahim, H.-K. Roth, S. Sensfuß, E. Klemm, D. A. M. Egbe, Thin Solid Films **444**, 215 (2003)

[68] E. K. Miller, G. S. Maskel, C. Y. Yang, A. J. Heeger, Phys. Rev. B **60**, 8028 (1999)

[69] F. C. Krebs, S. V. Hoffmann, M. Jorgensen, Synth. Met. **9563**, 1 (2002)

[70] S. L. Chuang, *Physics of Optoelectronic Devices* (Wiley-Interscience publication, New York, 1995)

[71] U. Zhokhavets, G. Gobsch, H. Hoppe, N. S. Sariciftci, Synth. Met. **143**, 113 (2004)

[72] Iam-Choon Khoo, *Liquid Crystals*, chapter 2.1 (Wiley-Interscience, New York, 1995)

[73] S. C. Jain, W. Geens, A. Mehra, V. Kumar, T. Aernouts, J. Poormans, R. Mertens, M. Willander, J. Appl. Phys. **89**, 3804 (2001)

[74] P. W. M. Blom, M. J. M. de Jong, M. G. van Muster, Phys. Rev. B **55**, 656 (1997)

[75] D. Chirvase, Z. Chiguvare, A. Knipper, J. Parisi, V. Dyakonov, J. C. Hummelen, Synth. Met. **138**, 299 (2003)

[76] S. A. Choulis, Y. Kim, J. Nelson, D. D. C. Bradley, M. Giles, M. Shkunov, I. McCulloch, Appl. Phys. Lett. **85**, 3890 (2004)

[77] H. Sirringhaus, P. J. Brown, R. H. Friend, M. M. Nielsen, K. Bechgaard, B. M. W. Langeveld-Voss, A. J. H. Spiering, R. A. J. Janssen, E. W. Meijer, P. Herwig, D. M. de Leeuw, Nature **401**, 685 (1999)

[78] J. Veres, S. Ogier, G. Lloyd, D. de Leeuw, Chem. Mater. **16**, 4543 (2004)

[79] S. Grecu, M. Bronner, A. Opitz, W. Brutting, Synth. Met. **146**, 359 (2004)

[80] A. Opitz, *Study of organic materials in field-effect devices,* Lecture, 5. April 2005, Ilmenau

[81] U. Zhokhavets, T. Erb, G. Gobsch, M. Al-Ibrahim, O. Ambacher, P. Schilinsky, C. Waldauf, C. Brabec, H. Hoppe, N. S. Sariciftci, *Effect of annealing on structural and optical properties of polythiophene/fullerene composite films for plastic solar cells,* Lecture, 17th Workshop on Quantum Solar Energy Conversion, 14.-18. March 2005, Rauris (Austria)

[82] A. Haugeneder, M. Neges, C. Kallinger, W. Spirkl W, U. Lemmer, J. Feldmann, U. Scherf, E. Harth, A. Gugel, K. Mullen, Phys. Rev. B **59**, 15346 (1999)

[83] X. Yang, J. K. J. van Duren, M. T. Rispens, J. C. Hummelen, R. A. J. Janssen, M. A. J. Michels, J. Loos, Adv. Mat. **16**, 802 (2004)

[84] Y. Kanemitsu, K. Suzuki, Y. Masumoto, Y. Tomiuchi, Y. Shiraishi, M. Kuroda, Phys. Rev. B **50**, 2301 (1994)

[85] G. Padmanaban, S. Ramakrishan, J. Am. Chem. Soc **122**, 2244 (2000)

[86] Tobias Erb, *Structure of polythiophene/fullerene composite films,* private communication

[87] T. Erb, U. Zhokhavets, G. Gobsch, M. Al-Ibrahim, O. Ambacher, *Influence of solvent and unnealing temperature on structural and optical properties of polythiophene/fullerene composite films,* Poster, EMRS Spring Meeting, 31. May - 3 June 2005, Strasbourg (France)

[88] C. Arndt, U. Zhokhavets, M. Mohr, G. Gobsch, M. Al-Ibrahim, S. Sensfuss, Synth. Met. **147**, 257 (2004)

[89] Stefan Voigt, *Investigation of charge carrier dynamics in polythiophene/fullerene films for plastic solar cells,* private communication

[90] C. J. Brabec, A. Cravino, D. Meissner, N. S. Sariciftci, T. Fromherz, M. T. Rispens, L. Sanchez, J. C. Hummelen, Adv. Func. Mat. **11**, 374 (2001)

[91] P. Schilinsky, C. Waldauf, C. J. Brabec, *EQE of P3HT/PCBM plastic solar cell,* private communication

[92] H. Hoppe, N. Arnold, D. Meissner, N. S. Sariciftci, Thin Solid Films **451**, 589 (2004)

[93] N. K. Persson, M. Schubert, O. Inganas, Solar Energy Materials and Solar Cells **403**, 368 (2002)

Acknowledgement

I would like to thank the following people who helped me to prepare this work:

- My supervisor Gerhard Gobsch for his constant support during this research;

- Tobias Erb for XRD measurements;

- Other members of "polymer" group Christian Arndt, Martina Mohr, Nicole Killat and Stefan Voigt for excellent team work;

- Norbert Stein for his technical assistance in the lab;

- Members of our work group at Ilmenau Technical University, Helmut Barth, Carsten Buchheim, Jens Eberhardt, Wolf Gnehr, Rüdiger Goldhahn, Marko Hofmann, Barbara Krause, Henrick Lösch, Pascal Schley, Dirk Schulze, Petra Sieck, Heidi Sülzner, Sviatoslav Shokhovets and Andreas Winzer for their friendly support;

- Harald Hoppe, Niyazi Serdar Sariciftci (LIOS Linz), Pavel Schilinsky, Christoph Waldauf, Christoph Brabec (Siemens, now Konarka Technologies Gmbh Erlangen), Sofiya Raleva, Bernd Stühn (TU Darmstadt), Maher Al-Ibrahim (ZMN/TITK), Steffi Sensfuss and Hans-Klaus Roth (TITK) for very nice and fruitful collaborations;

- My parents and my brother for their help.

Erklärung

Ich versichere, dass ich die vorliegende Arbeit ohne unzulässige Hilfe Dritter und ohne Benutzung anderer als der angegebenen Hilfsmittel angefertigt habe. Die aus anderen Quellen direkt oder indirekt übernommenen Daten und Konzepte sind unter Angabe der Quelle gekennzeichnet. Bei der Auswahl und Auswertung folgenden Materials haben mir die nachstehend aufgeführten Personen in der jeweils beschriebenen Weise entgeltlich/unentgeltlich geholfen:

... keine ....

Weitere Personen waren an der inhaltlich-materiellen Erstellung der vorliegenden Arbeit nicht beteiligt. Insbesondere habe ich hierfür nicht die entgeltliche Hilfe von Vermittlungs- bzw. Beratungsdiensten (Promotionsberater oder anderer Personen) in Anspruch genommen. Niemand hat von mir unmittelbar oder mittelbar geldwerte Leistungen für Arbeiten erhalten, die im Zusammenhang mit dem Inhalte der vorgelegten Dissertation stehen.

Die Arbeit wurde bisher weder im In- noch im Ausland in gleicher oder ähnlicher Form einer Prüfungsbehörde vorgelegt.

Ich bin darauf hingewiesen worden, dass die Unrichtigkeit der vorstehenden Erklärung als Täuschungsversuch angesehen wird und den erfolglosen Abbruch des Promotionsverfahrens zu Folge hat.

Ilmenau, den Uladzimir Zhokhavets